Chaudhry Amjad Ali Ghumman

Mestrado em Física

Time-of-Flight Secondary Ion Mass Spectrometry: New application for urinary stones analysis

Dissertação para obtenção do Grau de Doutor em
Engenharia Física

Orientador: Orlando Manuel Neves Duarte Teodoro
Professor Associado
Departamento de Física
Faculdade de Ciências e Tecnologia
Universidade Nova de Lisboa

Júri:

Presidente: Prof. Doutora Maria Adelaide de Almeida Pedro de Jesus
Arguentes: Prof. Doutor Reinhard Horst Schwarz
Doutor Paulo Jorge Amorim Madeira

Vogais: Prof. Doutora Maria Adelaide de Almeida Pedro de Jesus
Prof. Doutor Orlando Manuel Neves Duarte Teodoro
Prof. Doutor João Erse de Goyri O´Neill
Doutor Alexander Tolstoguzov

FACULDADE DE CIÊNCIAS E TECNOLOGIA
UNIVERSIDADE NOVA DE LISBOA

January 2013

Time-of-Flight Secondary Ion Mass Spectrometry: New application for urinary stones analysis

Acknowledgements

I would like to thank my supervisor, Prof. Dr. Orlando M.N.D. Teodoro, who kindly provided me the opportunity to work on this interesting, novel and valuable project. His abundant experience in instrumentation helped me to sort out many difficulties, which I am very grateful. He also introduced me to other groups and the departmental workshops, so that the co-operation with them could be done in a smooth way. Furthermore, the thesis will not have been achieved to this level without his direction.

I would also like to thank Prof. Dr. A.M.C. Moutinho, who provided me the scientific support during whole this project, especially in the scientific discussions. His friendly companion and suggestions in aspects other than research gave me many joys.

I would also like to thank Mrs. Olga M. T. Carreira (Serviço de Patologia Clínica do Hospital Garcia de Orta, Almada) and Mrs. Clara Barrento (Grupo Joaquim Chaves, SGPS, S.A.) for providing valueable urinary stone samples for this scientific research.

I would like to acknowledge my group members Dr. Alexander Tolstogouzov and Dr. Nenad Bundaleski for providing me many useful suggestions to finalize the discussion of this thesis.

I would also like to acknowledge Mr. A. Santos and all the coworkers from CEFITEC for their companionship.

I owe very much to my wife Mrs. Lubna who supported and encouraged me continuously.

Finally, I would like to acknowledge Foundation for science and Technology (Grant No. SFRH/BD/44558/2008) for financial support of this research.

Abstract

Time-of-flight secondary ion mass spectrometry was used to study the real urinary stones and the results were compared with those from commercially available urinary calculi organic compounds and minerals. Organic urinary stone components like uric acid and cystine were clearly identified by their respective protonated molecules $[M+H]^+$ and deprotonated molecules $[M-H]^-$. With TOF-SIMS analysis we clearly distinguished between uric acid and its sodium/potassium urates. The mass spectra of cystine stones were compared with those measured for the standard compounds, cystine and its monomer cysteine. Similar spectra were obtained for the stones and cystine. The most important identification was based on the existence of the protonated molecules $[M+H]^+$ and deprotonated molecules $[M-H]^-$.

The calcium oxalate (COX) stones were recognized by the presence Ca^{+2}, Ca^+, CaO^+, $CaOH^+$, Ca_2^+, Ca_2O^+, $Ca_2O_2^+$, and $Ca_2O_2H^+$ ions. The calcium phosphate stones were recognized with the presence of aforementioned ion peaks for calcium oxalate along with additional phosphate containing ions. Moreover, the phase identification of calcium phosphates was achieved in the positive SIMS mode on basis of the PO^+/POH^+ and $CaPO_2^+/Ca_2O^+$ peak ratios. We also quantified the calcium phosphate (up to < 3%) in the human calculi containing calcium oxalate as major or minor component, which is of a great interest for medical community, and the reliable phase identification of calcium phosphates also has potential application in bio-implant technology.

Struvite ($NH_4MgPO_4.6H_2O$) stones, also known as infection stones due to their association with urea-splitting bacteria were confidently identified by the presence of its major characteristic peaks of $NH4^+$, Mg^+, PO_2^-, PO_3^-. We also observed uric acid, sodium/potassium urates, apatite $[Ca_{10}(PO_4)_6(OH,CO_3)]$ and tri-calcium phosphate $[Ca_3(PO_4)_2]$ in struvite stones.

In our studies we also identified unusual components namely calcium formate $Ca(HCO_2)_2$, metabolite of vitamin B6 (4-deoxypyridoxine 5-phosphate) and iodine in three human stones.

Last but not least, the VG Ionex TOF-SIMS instrument used for this new application was upgraded which enables us to perform extensive experimental work for this study and for plentiful collaborated work published and being prepared for publications.

Keywords: TOF-SIMS; human calculi; calcium phosphate; phase identification; calcium oxalate; cystine; arginine; uric acid; struvite; urate; glycerol; C-SIMS.

Table of Contents

List of Figures

List of Tables

List of abbreviations

CaP	Calcium phosphate
CDHP	Calcium di-hydrogen phosphate monohydrate
COX	Calcium oxalate
C-SIMS	Constructive SIMS
DB	Dehydrated brushite (monetite)
DLL	Dynamic link library
ESA	Electrostatic analyzer
G-SIMS	Gentle SIMS
HAP	Hydroxyapatite
LMIS	Liquid metal ion source
S-SIMS	Static secondary ion mass spectrometry
TCP	Tri-calcium phosphate
TDC	Time to digital convertor
TOF-SIMS	Time-of-flight secondary ion mass spectrometry
UHV	ultra-high vacuum
VI	Virtual instrument

Publications

Published work included in Thesis

1. **C.A.A. Ghumman**, A.M.C. Moutinho, A. Santos, A. Tolstogouzov, O.M.N.D. Teodoro; TOF-SIMS VG Ionex IX23LS: upgrade and application for the urinary stones analysis. *Surf. Interface Anal.*, **2013**, 45, 532.
2. **C.A.A. Ghumman**, A.M.C. Moutinho, A. Santos, O.M.N.D. Teodoro, A. Tolstogouzov. An upgraded TOF-SIMS VG Ionex IX23LS: study on the negative secondary ion emission of III-V compound semiconductors with prior neutral cesium deposition. *Applied Surface Science* **2012**, 258, 2490.
3. **C.A.A. Ghumman**, A.M.C. Moutinho, A. Santos, A. Tolstogouzov, O.M.N.D. Teodoro; TOF-SIMS study of cystine and cholesterol stones. *J. Mass. Spectrom*. ***2012***, 47, 547.
4. **C.A.A. Ghumman**, A.M.C. Moutinho, A. Tolstogouzov, O.M.N.D. Teodoro. Time-of-flight secondary ion mass spectrometric identification of calciumformate $Ca(HCO_2)_2$ andmetabolite of vitamin B6 in human stones. *Rapid Commun. Mass Spectrom.* **2011**, 25, 997.
5. **C.A.A. Ghumman**, O.M. T. Carreira, A.M. C.Moutinho, A. Tolstogouzov, V. Vassilenko, O.M.N.D. Teodoro. Identification of human calculi with time-of-flight secondary ion mass spectrometry. *Rapid Commun. Mass Spectrom*. **2010**, 24, 185.

Other relevant published work

6. M.B. Gawande, P.S. Branco, I.D. Nogueira, **C.A.A. Ghumman**, N. Bundaleski, A. Santos, O.M.N.D. Teodoro, R. Luque. Catalytic applications of a versatile magnetically separable FeMo nanocatalyst. *Green Chem*. **2013**, DOI: 10.1039/C3GC36844K
7. M.B. Gawande, A.K. Rathi, P.S. Branco, A. Tolstogouzov, **C.A.A. Ghumman**, O.M.N.D. Teodoro, A. Velhinho. Nano-MgO-ZrO_2 Mixed Metal oxides: Characterization by SIMS and application in the reduction of carbonyl compounds and in multicomponent reactions. *RSC Advances* **2013**. DOI: 10.1039/C2RA22511E
8. M.A. Neto, E.L. Silva, **C.A. Ghumman**, O.M. Teodoro, A.J.S. Fernandes, F.J. Oliveira, R.F. Silva. Composition profiles and adhesion evaluation of conductive diamond coatings on dielectric ceramics. *Thin Solid Films* **2012**, 520, 5260.
9. M.B. Gawande, A. Velhinho, I.D. Nogueira, **C.A.A. Ghumman**, O.M.N.D.Teodoro, P.S. Branco. facile synthesis of cysteine-ferrite magnetic nanoparticles for application in multicomponent reactions - A sustainable protocol. *Royal Society of Chemistry*, **2012**, 2, 6144
10. M.B. Gawande, A. Rathi, I.D. Nogueira, **C.A.A. Ghumman**, N. Bundaleski, O.M.N.D. Teodoro, P. S. Branco. A Reusable and Recyclable Ferrite-Co Magnetic Nanocatalyst for Oxidation of Alcohols to Carbonyl Compounds. *ChemPlusChem* **2012**, 77, 865

11. M.B. Gawande, A.K. Rathi, P.S. Branco,I. D. Nogueira, A. Velhinho, J.J. Shrikhande, U.U. Indulkar, R.V. Jayaram. **C.A.A. Ghumman**, N. Bundaleski, O.M.N.D. Teodoro; Regio- and Chemoselective Reduction of Nitroarenes and Carbonyl Compounds over Recyclable Magnetic Ferrite_Nickel Nanoparticles (Fe_3O_4-Ni) by Using Glycerol as a Hydrogen Source, *Chem. Eur. J.* **2012**, 18, 12628
12. M.B. Gawande, P.S. Branco, K. Parghi, J. J. Shrikhande, R. K. Pandey, **C.A.A. Ghumman**, N. Bundaleski, O. M. N. D. Teodoro, R. V. Jayaram. Synthesis and characterization of versatile MgO–ZrO2 mixed metal oxide nanoparticles and their applications. *Catal. Sci. Technol.*, **2011**, 1, 1653.
13. R. Said, **C.A.A. Ghumman**, O.M.N.D. Teodoro, W. Ahmed, A. Abuazza, and J. Gracio ; Effects of Bias Voltage on Diamond Like Carbon Coatings Deposited Using Titanium Isopropoxide (TIPOT) and Acetylene/Argon Mixtures onto Various Substrate Materials. *J. Nanosci. Nanotechnol*. **2010**, 10, 2552.
14. R. Said, N. Ali, **C.A.A. Ghumman**, O.M.N.D. Teodoro, and W. Ahmed; Characterisation of DLC Films Deposited Using Titanium Isopropoxide (TIPOT) at Different Flow Rates. *J. Nanosci. Nanotechnol.* **2009**, 9, 4298.
15. V.F. Neto, R. Vaz, N. Ali, M.S.A. Oliveira, J. Grácio, **C.A.A. Ghumman** and O.M.N.D. Teodoro. Carbon diffusion into steel during diamond chemical vapour deposition. *Int. J. Nanomanufacturing*. **2008**, 2/ 3, 192.
16. V.F. Neto, R. Vaz, T. Shokuhfar, **C.A.A. Ghumman**, O.M.N.D. Teodoro, N. Ali, M.S.A. Oliveira, J. Grácio, Diffusion of critical elements in steel during thermal treatments in a diamond chemical vapour deposition atmosphere . *Defect and Diffusion Forum* **2006**, 258-260, 270.

1. INTRODUCTION

Since its early days SIMS (Secondary Ion Mass Spectrometry) has been extensively used for material characterization. Applications of SIMS have included the study of metals and semiconductors and, more recently, of oxides and other nonconductive samples. The potential of SIMS for the study of biological samples is now being explored. The advent of time-of-flight SIMS (TOF-SIMS) has brought increased power to the technique with a virtually unlimited mass range, high mass resolution and the advantage of the low dose of primary ions needed to obtain spectra from quasi-non destructive surface. Therefore, TOF-SIMS is now being used not only to provide elemental (including isotopic) and molecular composition in a range of industrial materials, but also for the characterization of an increased number of biomaterials. For instance, it was used for biological structure investigations [1, 2] and the study of the distribution of inorganic elements in the cells such as calcium, magnesium and boron [3]. Recently, we employed TOF-SIMS for the characterization of MgO–ZrO_2 mixed metal oxide nanoparticles [4] catalysts and the catalysts supported on Fe_3O_4 [5-7].

Secondary ion mass spectrometers developed in the mid-80s still remain the right tools for applied and fundamental research because of the quality of vacuum and analytical parts. However, these machines are equipped with old-fashioned electronics and in many cases, lost the operational technical support because the manufacturing companies moved to the newest productions or were closed down. We will briefly discuss the modernization and upgrading of data acquisition and control system of a TOF-SIMS VG Ionex IX23LS (Burgess Hill, UK) [8] making this instrument suitable for qualitative and quantitative analyses of real urinary stones.

1.1 Urinary calculi

The generation of solid stones inside the kidney (nephrolithiasis) and the ureter (urolithiasis) is an increasing danger to human health. These concretions (calculi) usually arise

due to the breakdown of a delicate balance in the body. Renal stones are common in western industrialized countries, whereas bladder ones are rather occasional. Worldwide, about 10% of the population is affected by this pathology at some stage of their life with the maximum incidence occurring between the ages of 20 and 40 [9].

The prevalence and incidence of nephrolithiasis are reported to be increasing across the world. These increases were seen across sex, race and age [9]. The pathogenesis is still unclear. It may be due to aspects of dietary intake, including the quality of drinking water. It may also be due to an inherent metabolic disorder of the patient, such as association of cystine stones with cystinuria. Nephrolithiasis is one of the most painful illnesses, because of the mechanical irritation of the stones on the urinary tract tissues. Severity of pain depends upon the size and surface roughness of the stone and varies from patient to patient. The ureteral stone passage study [10] shows that patients with ureteral stones <10mm undergo spontaneous stone passage (with or without medical therapy) while most of the patients with stones >10mm require surgical removal of the stones followed by preventive treatment against recurrence. The selection of treatment to prevent recurrence, which is about 50% [11], depends upon the chemical composition of patient's stone [12].

The chemical composition of urinary calculi is quite different; these can be composed of a variety of organic and/or inorganic substances. The main groups of urinary stone components include:

- Inorganic crystalline substances: calcium oxalates, calcium phosphates and magnesium ammonium phosphates.
- Organic crystalline substances: uric acid, urates and purine derivatives.
- Cystine and arginine.
- Organic non crystalline substances: protein, matrix stones, blood coagulum.
- Artifacts, falsifications.

A majority of kidney stones are calcium stones, with calcium oxalate and calcium phosphate accounting for approximately 80% of all kidney stones, about 10-15% are Struvite stones, occurrence rate of uric acid is about 5-10%, cystine is not that frequent with less than 1%, but it is important because of the high recurrence rate without metaphylaxis (measures to minimize or eliminate an expected occurrence) and rest are other components [13].

The management of stones found in humans requires a combined clinical and surgical approach. In general, severe obstruction, infections, intractable pain and serious bleeding are indications for the removal of a stone. Considerable progress has been made in the investigation

of the formation of urinary stones, attempting to identify promoting and inhibiting factors in their growth. However, extensive interdisciplinary studies are required in order to correlate the calculi composition with the pathophysiology of illness. A better understanding of the physiochemical principles underlying the formation, promotion and inhibition of calculi needs more accurate information on their chemical content. Imprecise chemical analysis can lead to wrong planning of their treatment and of ways to stop their reoccurrence.

The compositional analysis of urinary stones is an important requirement for a successful management of the disease, which implies not only a proper evaluation and treatment, but also prophylaxis to prevent recurrence, which is impossible without knowing the composition of the urinary stones involved.

1.2 Current analytical approaches

Currently, several chemical and physical techniques are available for the investigation and routine analysis of urinary stones. These techniques include: wet/dry chemical methods[14] although obsolete but still practiced, Fourier transform infrared spectroscopy but it may produce complex spectra resulting from the interference of known biomaterial with unknown substances [15,16, 17] common in such complex natural samples, X-ray diffraction but it is unsuitable for the analysis of amorphous substances such as carbonate apatite [18 ,19], scanning electron microscopy [18] but the material in urinary calculi is also prone to irradiation damage during electron microscopy , laser induced plasma spectroscopy [20], X-ray photoelectron spectroscopy [21], thermal decomposition suited for a few types of kidney calculi such as Struvite [22], X-ray absorption near-edge spectroscopy with synchrotron radiation [23] and micro-computed tomography [24,25]. However, only Fourier transform infrared spectroscopy and X-ray diffraction are the methods recommended by the European Association of Urology (2011), although, these techniques have also some limitations, which are beyond the scope of the present study.

1.3 Thesis overview

In this work we have used time-of-flight secondary ion mass spectrometry (TOF-SIMS) for the analysis of urinary stones as it is a well-established and widely applied surface analytical technique equally suitable for organic and inorganic materials.

Although TOF-SIMS is an acknowledged technique for biomaterial investigations, to the authors' knowledge there has been no report on its use for the investigation of human calculi (except authors´ own recently reported work [26-29]). The aim of this work is to demonstrate the applicability of TOF-SIMS for the identification of various inorganic and organic species in human calculi. The simple sample preparation procedure combined with the capability of detecting $[M+H]^+$ or $[M–H]^-$ ions (in the case of organic calculi) and fragment ions (in the case of inorganic stones) makes TOF-SIMS suitable not only for routine analysis, but also for the identification of trace elements, and imaging of such samples. Let us briefly describe chapter wise the scheme of this comprehensive study.

In the following chapter (2) we will briefly describe the fundamentals of secondary ion mass spectrometry; sputtering of organic and inorganic materials, ionization of sputtered materials based on the ionization models. And finally different modes of SIMS analysis and some usefully methodologies to characterize the sample from the SIMS measurements e.g. constructive-SIMS (C-SIMS), a new methodology proposed in this work for molecular structure revelation.

In chapter 3, we will discuss the working principle of TOF-SIMS; mass analyzer, ion sources. The instrumental description will also be presented including the upgrade of the TOF-SIMS instrument made in the framework of the present study, especially the data acquisition and control system designed and developed. New ion source tungsten tip wetting (with liquid metal) methodology under ambient conditions will be presented. Finally, the presently used sample preparation techniques will be discussed, especially from the powder samples. We will propose a new sample preparation method for the non-conducting powders which is always considered to be a challenging task to produce good SIMS results. The sample prepared by the proposed technique gives very good molecular ion yield even without any charge compensation.

In chapter 4, the analysis of organic calculi (uric acid, sodium/potassium urates, cystine and cholesterol) will be presented [26-28]. The results will be compared with that of reference chemicals for the classification. The classified stones will be further compared within same class for different individuals. In this study we clearly identified uric acid, and cystine form their protonated $[M+ H]^+$ and deprotonated $[M-H]^-$ molecules. The organic salts like sodium urate were identified by the more intense sodiated uric acid peaks as compared to protonated uric acid. Cholesterol stone was recognized through its most abundant ion peak at m/z 269 $[M-OH]^+$. The absence or presence of any additional components was also identified, e.g. metabolite of vitamin B6 was identified in urate stone [27].

In chapter 5, the results of calcium oxalate stones will be presented, we clearly identified calcium oxalate stones admixed with calcium phosphates and uric acid. We identified calcium

formate ($CaH_2C_2O_4$) in one of the calcium oxalate stone [27]. The results of stones identified as core & shell as uric acid & calcium oxalate respectively and vice versa in stones of two individuals will be presented. Finally, in this chapter we will present the overall difference observed in the stones data by comparing with that of reference chemical resulting identification of calcium phosphate in all stones (100%) classified as calcium oxalate, although in some of them calcium phosphate was less than 10%.

In chapter 6, the new method of phase identification for calcium phosphates will be presented. Only a limited number of authors have reported analysis of these important biological materials using SIMS as complimentary technique. But according to our knowledge, there are no publications on the SIMS quantification of these components, especially calcium phosphates and calcium oxalate forming approximately 80% of real human stones [13]. To correlate the chemical nature of the stones with appropriate medical diagnoses, the phase identification and quantification of calcium phosphates in calcium oxalate are of a great importance for clinical investigations because calcium phosphate contents could be a useful factor for the prediction of recurrence [30]. The quantification makes possible to classify the stones by knowing the relative contents, which is regarded as an important factor in general practice, especially in shock wave lithotripsy treatments [31].

In the TOF-SIMS studies [32-35] of calcium phosphates, *Chusuei et al*. [34] and *Lu et al.* [35] used polyatomic and monatomic primary ions for the phase identifications, the relative intensities of molecular secondary ions PO_2^- and PO_3^- were used. However, the values of PO_3^-/PO_2^- ratio for five out of six calcium phosphates were so close in pairs that they might be indistinguishable in real samples. In our study [29] using Ga^+ as primary ions, we demonstrated clear phase identification both for pure calcium phosphates and in their mixture with calcium oxalate via proper selection of the characteristic positive secondary ions.

In chapter 7, the TOF-SIMS results of struvite stones will be presented which will be compared with reference chemicals and with other stones classified as struvite. Again it might be interesting to state that no TOF-SIMS study on struvite urinary stones, geological samples, or standard samples was found (except the part of present study [26]). In our study we clearly identified the pure struvite stones, mixed with calcium phosphates, and urates. The only calcium phosphates we found in these stones were tri-calcium phosphate and hydroxylapatite. It might be interesting to state here that in this work we revealed that it is possible to recognize calcium oxalate from calcium phosphates present in struvite stones. We did not found calcium oxalate in these stones. Furthermore, association of Na^+ with hydroxyapatite and K^+ with struvite

components was also revealed statistically in 13 struvite stones which we have also confirmed in a single sample with micro-analysis TOF-SIMS chemical image mode.

In chapter 8, we will briefly summarize the results of total 38 stones including two dog stones identified as struvite and cystine. We will also present our compositional statistical analysis to estimate the occurrence frequency of different urinary components from the stone formers in the population of Portugal.

2. SECONDARY ION MASS SPECTROMETRY

Secondary Ion Mass Spectrometry (SIMS) is the mass spectrometry of secondary ions which are produced when a surface is bombarded by energetic primary projectiles, typically ions for example, Au_n^+, Ar_n^+, Bi_n^+, Cs^+, C_{60}^+, Ga^+, O_2^+, O^+, and O^- etc. where *n* represents for number of atoms. The sputtered secondary particles are electrons; neutral species of atoms or molecules; elemental, molecular and cluster ions. The vast majority of species emitted are neutral (~ 99 %) but it is the secondary ions accounting for ca. 1% of sputtered species that are detected and analyzed by a mass spectrometer. The resulting mass spectrum gives detailed chemical composition of the subject material.

Time-of flight SIMS (TOF-SIMS) is a leading experimental choice of static SIMS that emerged as a technique of potential importance in surface science as a result of the work of Benninghoven and his coworkers in Münster in the late 1960s. The working principle is very simple and is shown in Figure 2.1. When an energetic (1-30 keV) beam of ions bombards a surface, the particle energy is transferred to the atoms or molecules of the surface at impact site. A cascade of collision occurs between the atoms and molecules in the target material: some collisions return to the surface and result in the emission of atoms, atomic clusters, molecules and molecular clusters; some of which are ionized in the course of leaving the surface.

While the technique is apparently destructive, the essence of the static mode is to use an extremely low dose of primary ions ($< 10^{13}$ ions cm^{-2}), such that the top surface layer of atoms or molecules do not receive more than one ion impact within the time scale of the experiment. The spectral information arising in static mode is of representative of surface chemistry and can be exploited in many fields of applications. In addition to static SIMS mode, TOF-SIMS is now routinely used in imaging and depth profile modes. The mass spectrum is the essential part of all modes of operation. To interpret the SIMS results one should consider secondary ion yield, which depends on sputtering and ionization of sputtered material. Let us discuss these parameters briefly; details are available in literature [36].

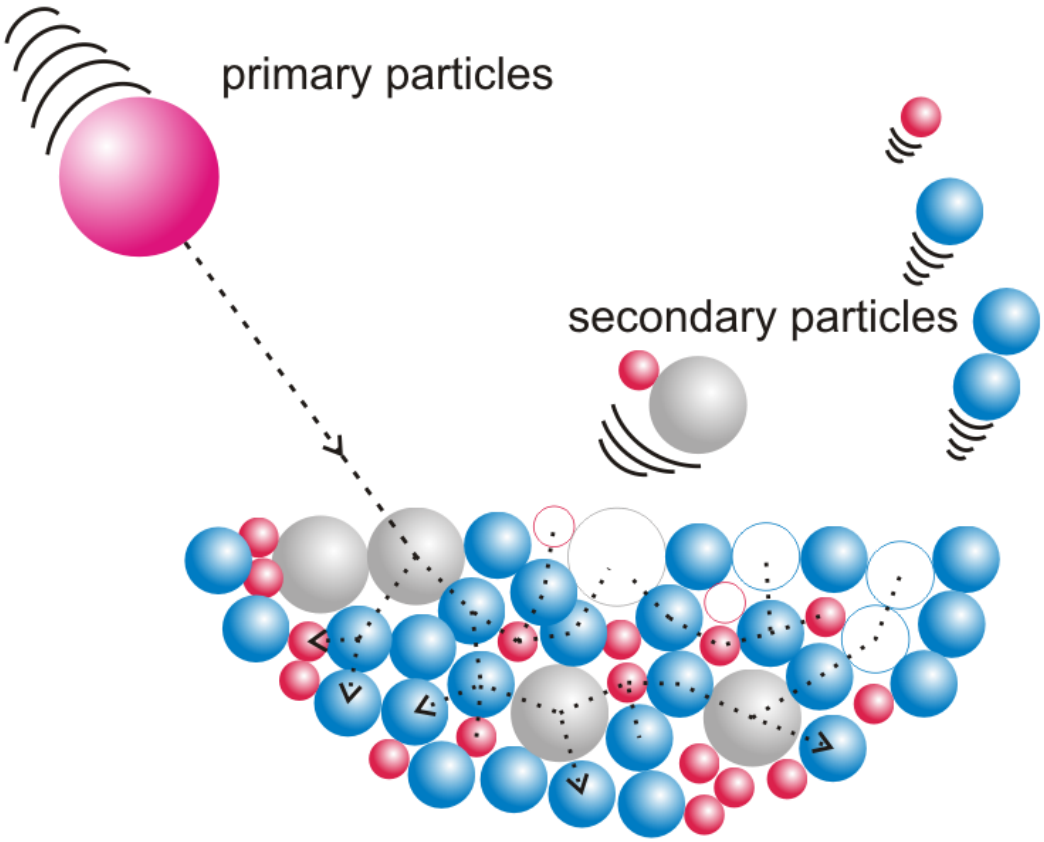

Figure 2.1. Schematic diagram of the SIMS principle.

2.1 SECONDARY ION YIELD

Sputtering and ionization are the basic processes in surface analysis by SIMS. More extensive details concerning the sputtering and secondary ion emission can be found elsewhere [36 and references therein]. SIMS is concerned with the analysis of secondary ions. Ionization occurs at, or close to, the emission of particles from the surface with the consequence that the matrix participates in the electronics processes involved. This means that the yield of secondary ions is strongly influenced by the electronic state of the material being analyzed consequently complicates the quantitative analysis. The signal intensity of particular species is governed by the basic secondary ion yield equation (2.1) as follows;

$$I_m^+ = I_p Y_m \alpha^+ C_m \eta \qquad (2.1)$$

Where I_m is secondary ion intensity of species m, I_p is the primary particle flux, Y_m is the sputtering yield, α^+ is ionization probability of *positive ions*, C_m is the fractional concentration of the species m in the surface layers and η is the transmission of the mass spectrometer.

2.1.1 Sputtering of inorganic materials

Sputtering of a target by energetic ions or recoil atoms is greatly reviewed by *P. Sigmund* [36, 37] based on the cascades of atomic collisions. The parameter characterizing the sputtering process is sputtering yield (Y), which is defined as the ratio of the average number of the ejected to the number of bombarded particles. The parameter Y_m in Equation (2.1) is the sputtering yield and $\alpha^+.Y_m$ is the average number of positive ionic particles of species *m*, per primary ion impact. It also increases with primary particle mass, charge, and energy, although not linearly. Figure 2.2 shows the energy dependence of sputtering yields of Ni by a variety of ions at normal incidence [38]. The target structure (crystallinity, texture), surface topography, beam-induced changes in both structure and topography, target temperature, and incident angle affect the yield. The threshold is not at the surface binding energy *U (~3eV)* but at a substantially higher energy.

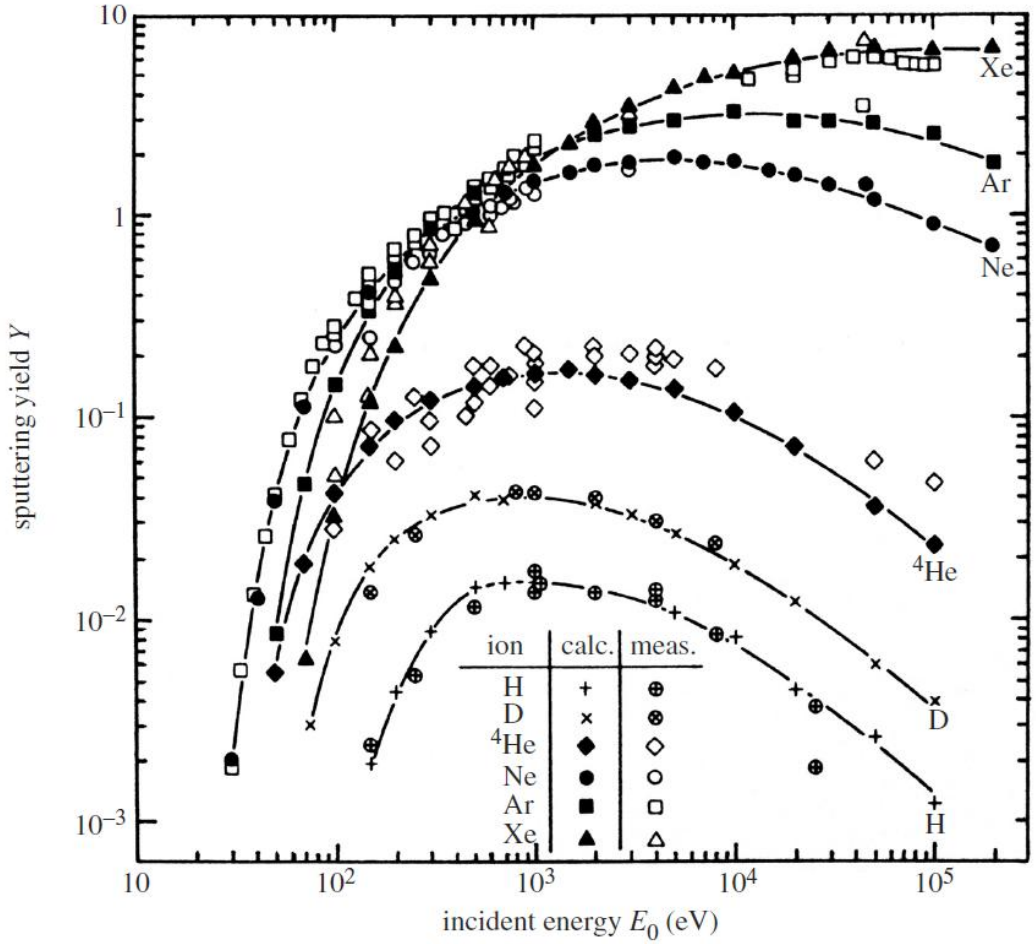

Figure 2.2. Sputtering yields of Ni by different projectiles versus projectile energy. Also shown are values calculated using the transport of recoils and ions in matter (TRIM) Monte Carlo simulation program [3].

Typical threshold of the sputtering occurs at about 15–40 eV primary particle energy [39, 40] and yield tends to maximize with energy up to 50 keV. For lighter primary particles the maximum is

reached at ca. 1 kev. Beyond this energy, yield drops away as the primary particles penetrates deeper into the solid and less energy returns to surface region.

2.1.2 Sputtering of organic materials

Sputtering is damaging process; consequently it is more difficult to measure sputtering rates for the organic materials. The sputtering yield of elemental carbon and nitrogen can be measured, but in static SIMS we are more interested in using the technique to detect and measure the chemical structure. In sputtering of organic materials; atoms, structural fragments and molecules are removed from the surface resulting destruction of chemical structure within area from which these species are removed. In molecular materials, every impacted molecule will be significantly destroyed, whether complete molecule or small fragment of the molecule is removed. In polymer materials, the impacted monomer unit will be destroyed. Thus instead of sputter rate the concept of damage cross-section, б, has found to be useful. The loss of structurally important species from the SIMS spectrum as a function of accumulative bombardment dosage in time ´*t*´ is taken to be measure of increasing damage. Obviously the greater the damage cross section lesser will be the molecular ion yield. The relation between the secondary ion intensity (I_m) of specie *m* and damage cross section ´*б*´ is as follows [36];

$$I_m = Y_m \, exp(-\sigma I_p) \qquad (2.2)$$

W. Sicthermann and *A. Benninghoven* measured damage cross-sections of around 10^{-14} cm^2 (or 1 nm^2) from amino acid and other small molecules on the metal surface [41]. For elemental sputtering, secondary ion yields and damage cross sections for organic materials increases with primary ion mass, energy and increasing angle of incidence away from the normal. In recent years with the development of argon gas cluster ion sources at Kyoto University [42] molecular ion yield boost up compared to other polyatomic and cluster ion sources [43]. The enhancement in the molecular ion yield increase with increasing cluster size at same energy due to more gentle impacts on the surface resulting low damaging.

2.1.3 Ionization

2.1.3.1 Ionization of inorganic materials

Ionization of sputtered secondary particles is strongly influenced by the electron exchange processes between departing species and the originating surface. Thus the electronic state of the surface is an important factor in SIMS. The secondary ion yield of elemental species

can vary by several orders of magnitude across the periodic table, and strongly depends on the chemical state of the surface that is called matrix effect i.e. the strong dependence of the secondary ion yields on the analysis conditions and on the characteristics of the target.

Matrix effect plays an important role in SIMS quantitative analysis. The inconsistency of ion yields is the major problem as the surface composition changes. The same species will not have same secondary ion yield in different chemical environment, making direct comparison difficult among samples. The environment of a single sample can change during the analysis. As a result, differential removal of particles from the specimen can occur due to preferential sputtering [39]. Moreover, the probability of ion formation can vary as a result of change in the sputtering process due to ion beam damage and implantation of bombarding species as shown in Figure 2.3.

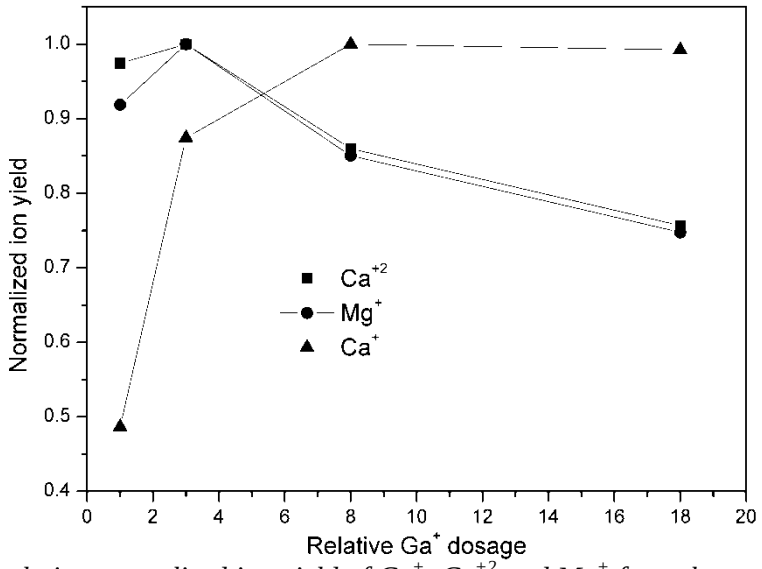

Figure 2.3: The relative normalized ion yield of Ca^{+}, Ca^{+2} and Mg^{+} from the sample with Ca/Mg atomic ratio of 2.373 under Ga^{+} bombardment. Due to surface modification the ion yield of singly charged calcium (Ca^{+}) increased while magnesium(Mg^{+}) decreased, the decrease similar to magnesium was observed for doubly charged calcium (Ca^{+2}) [from the present work].

These variations in the ion yield are due to surface modification that can be explained on the basis of well known [36] modifications of electronic state of the surface by oxidation and cesiation commonly used for enhancement of positive and negative secondary ions respectively. Oxidation can be achieved by oxygen flooding on the surface or by bombardment with oxygen species (O^{-}, O^{+}, and O^{+2} etc) while cesiation can be achieved by bombardment with cesium ions or neutral Cs deposition of sub-monolayer coverage.

In order to understand these useful surface modification effects and hence interpret the SIMS results, one has to consider some fundamental ionization models. Before we discuss the ion formation in organic materials let us first illustrate few common ionization models [44, 45].

2.1.3.2 Electron Tunneling Model

In the electron-tunneling model [45], the discrete electronic level of the sputtered atom interacts with the continuum of electronic states of the solid. The central feature of this continuum of electronic states is the Fermi level which separates occupied and unoccupied states. During the removal of the particle, while it is still in the vicinity of the surface, the atomic levels of the sputtered atom overlap with the electronic levels of the metal. The Fermi Level E_F of the metal can be higher or lower than the atomic level after the sputtered atom has reached a certain distance R_C from the surface, and therefore an exchange of an electron is energetically possible as shown in Figure 2.4.

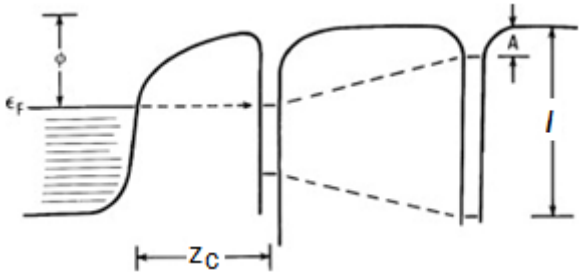

Figure 2.4. Energy-level diagram for an atom or molecule characterized by its highest occupied (image-potential-upshifted) valence level I and lowest unoccupied (downshifted) affinity level A interacting with a metal surface. The lowering of the affinity level allows a Fermi-level electron from the substrate to tunnel into the atom/molecule thus creating a negative ion. This possibility is turned on at a separation Z_c where the shifted affinity level coincides with the Fermi level [46].

The direction of the charge transfer is depending on the values of the work function Φ of the metal and the ionization potential I (or the electron affinity A, respectively) of the sputtered particle. A potential barrier between the electronic states inhibits the charge transfer, but tunneling of the electron to/from the atom is possible with a probability that is exponentially dependent on the distance where the energy levels become equal (determined by the work function Φ of the metal) and on the normal component of the velocity $v_\perp$ of the sputtered particle (determining the time for interaction). The ionization probability for negative (P^-) and positive (P^+) ion formation can be described by following equations 2.3 and 2.4 for the tunneling of electron from the surface and towards the surface, respectively.

$$P^- \propto exp\,(-2\Delta(Z_c)/\hbar\gamma v_\perp).exp(-(\Phi-A)/\mathcal{E}_n) \tag{2.3}$$

$$P^+ \propto exp\,(-2\Delta(Z_c)/\hbar\gamma v_\perp).exp(-(I-\Phi)/\mathcal{E}_p) \tag{2.4}$$

Where, $\Delta\,(Z_c)$ is a function describing the broadening of the atomic level at the distance Z_c (Figure 2.5) when the Fermi level crosses the atomic level $\mathcal{E}_a$. $v_\perp(Z_c)$ is the normal component

of the velocity at distance Z_c; $\mathcal{E}_p$, $\mathcal{E}_n$ are proportional to the normal component of the velocity, and γ is a characteristic length parameter.

One way to make use of the exponential dependence of the ionization probability on the work function of the surface is to lower the work function as much as possible to enable charge transfer to the sputtered atom at low distances Z_c. This increases the probability for negative ion generation by several orders of magnitude. It can be obtained by covering the surface with a sub-monolayer of alkali metals, e. g. from a Cs sputter ion gun performing used for SIMS analysis.

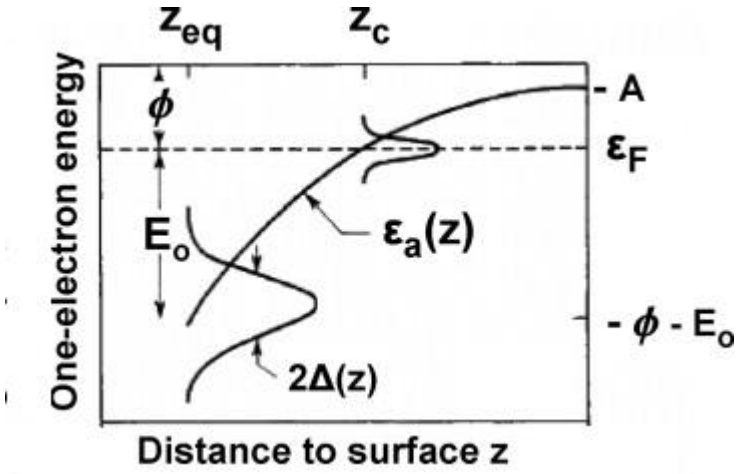

Figure 2.5. Variation of an atomic affinity level $\mathcal{E}_a$ with distance Z from a metal surface. $\mathcal{E}_a$ crosses the Fermi level $\mathcal{E}_F$ at Z_c, and approaches the free atom affinity level –A. As the atom moves away from the surface, the width Δ of the level decreases [46, 47].

From the equation (2.3) for P^-, an exponential increase of the ionization probability with Cs surface concentration is expected. The probability (P^-) decreases when all sputtered atoms are ionized or when the work function has reached its minimum value. For the emission of positive ions (eq. 2.4), a low work function can be detrimental. If for example a positive ion is leaving the surface, the first unoccupied atomic level can be lower than the Fermi level, making an electron transfer from the surface to the ion possible, which re-neutralizes the emitted ion. This is illustrated by the Cs^+ intensity during Cs sputtering, which increases at low Cs coverage according to the increase in Cs concentration. As soon as the work function is lowered significantly, the Cs^+ intensity decreases again. At this stage, re-neutralization starts to suppress the increase by high concentration and therefore sputtered Cs atoms [48, 49]. Typically, this is the case as soon as the work function is only about 0.5 eV higher than the ionization potential of Cs. Whether or not the under Cs bombardment is depending on the sputter yield of the target material at the given energy and angle of incidence, which determines the maximum Cs concentration and hence the minimum work function decrease of the positive ionization probability is observed with increasing Cs coverage

2.1.3.3 Bond Breaking Model

For oxides (and halides), which are present on almost all elemental targets or can be formed by bombardment or chemisorption, the bond breaking model [50, 51] describes the ionization as a consequence from the breakup of an ionic or covalent bond. An electropositive atom leaving the surface is ionized by breaking its bond to another surface atom and leaving one electron behind.

A very concise discussion of this model is given in the cited reference [52 and references therein]. The practical result of this discussion is an expected exponential decrease of the ionization probability with increasing ionization potential '*I'*. Electropositive elements in an oxide or halide environment will effectively be ionized by breaking the surface bonds, which is utilized when a surface is bombarded or flooded with oxygen to incorporate it into the altered layer. Thus the ionization probability for electropositive species is increased by up to three orders of magnitude [45]. Oxygen bombardment and/or oxygen flooding is extensively used for all kinds of materials. The sputter yield also depends on the degree of oxidation [53] resulting in a further influence on the ion yield.

2.1.3.4 Recombination Model

In contrast to the two models described above, the recombination model is specifically valid for cluster ions of matrix species with one or two Cs atoms originating from the sputter beam or presence of alkali metals in the target surface. Basically, the model assumes the emission of Cs^+ ions together with sputtered neutrals M that (re)combine above the surface to form MCs^+ or MCs_2^+ cluster ions.

Although the strong emission of these clusters has been known longer [54], their importance for some application like detection of rare gases [55] and the quantification of matrix compounds [56, 57] was recognized only in early 1990s.

As already mentioned in electron tunneling model, a surface covered with a submonolayer of Cs emits Cs^+ ions with a very high degree of ionization. This high degree of ionization is virtually independent of the matrix, since the work function is mainly defined by the Cs over-layer itself. Only if the Cs concentration becomes very high, the degree of ionization is reduced and becomes dependent on the surface concentration.

The composition of the flux of sputtered particles from the target is representative of the concentrations in the bulk as soon as the sputter equilibrium has been reached.

The yield of cluster ions formed by combining Cs^+ ions with sputtered neutrals should therefore be independent of the chemical state of the surface.

$$Y_{MCs}{}^{+} \propto Y_{Cs}{}^{+}.Y_{total}.C_M.\ f_{MCs} \tag{2.5}$$

If at all, only a weak matrix effect is observed. Apart from f_{MCs} (the formation probability for the cluster ion), all factors in eq. (2.5) are constant and rather well understood. For quantification purposes, the formation probability is assumed to be constant, and the yield $Y_{MCs}{}^{+}$ divided by the Cs^+ intensity should be directly proportional to the concentration C_M of M.

2.1.3.5 Ionization of organic materials

Secondary ion formation from the organic materials can occur by a number of mechanisms. Loss or gain of an electron to form an odd electron molecular radical ions M^+ or M^-, polar molecules may undergo acid base reaction to form protonated $[M+H]^+$ or deprotonated $[M-H]^{\pm}$ molecules; cationization or anionization of neutral molecules may occur. These processes are mainly relevant to molecular species, low mass fragments also provide important information for chemical structure determination, e.g. the molecules with OH terminals gives $[M-OH]^+$ signals rather higher than protonated/deprotonated molecules. Ionization of these species probably occurs via collision cascade mechanism due to direct interaction with primary ion or energetic recoil atoms within the material. The exact location of these ionization processes is still mystery, but likely in the emission region within or just above the surface. Matrix effects (surface coverage, substrate) do influence secondary ion yields from organic materials, but they are generally not so marked as from inorganic systems. Ion yields from copolymers have been observed to be sensitive to identity of the components. Clearly cationization will be favored when suitable cations (Ag, Na, K, and Cs etc) are present in the matrix. We will briefly discuss different types of ions formation from the organic and inorganic materials; details can be found elsewhere [36].

2.1.3.6 Formation of protonated and deprotonated ions ($[M+H]^+$, $[M-H]^-$)

The analyte molecule mass *m* can be directly derived from the protonated and deprotonated molecule observed. The formation of these molecular ions molecules strongly depends on structure of the analyte. The emission $[M+H]^+$ is often surface coverage dependent.

The protonated molecules are formed if analyte molecule contains basic groups. For peptide (polymers of amino acids), for example, the signal intensity of $[M+H]^+$ is most intense if they contains basic side chains ($-NH_2$). No protonated molecules are formed if peptide does not contain any basic side chain and additionally its N-terminus is blocked. In a few cases, the production of protonated ions is blocked for a sub-monolayer coverage e.g. fatty acids and

glycerol-monostearate. An intermolecular proton transfer is supposed to be responsible for this behavior, although a detailed understanding of the underlying mechanism is still unclear.

Deprotonated molecules can be produced if the analyte molecular structure contains acidic groups (-COOH). All fatty acids show $[M-H]^-$ emission. In contrast to the $[M+H]^+$, the formation of deprotonated ions is layer independent. However, it is influenced by the substrate properties. Sometimes it has been observed as decomposition of $Ag^+(M-H)^-$ complexes or by intermolecular proton transfer between adjacent molecules.

As the influence of chemical environment on the $[M+H]^+$ and $[M-H]^-$ emission is strong, it is always worthwhile to tailor the substrate properties specifically in order to promote the respective ion formation. Gusev et al. for example, reported on the enhanced $[M+H]^+$ emission of peptide from HBr treated surfaces [see reference therein 36].

2.1.3.7 Formation M^+, M^-, and by loss of small functional groups

These ionization pathways are distinctively influenced by the chemical structure of the analyte molecule and, generally, are only seldom observed in SIMS experiments. However, they can be the only pathway in thick layers.

The formation of M^+ and M^- occurs mainly out of pre-formed states, for example if the molecule contains N^+ centers or from pre-charged dyes. The ion like $[M-CH_3]^-$, $[M-OH]^+$ are observed by the loss of functional groups if such groups can easily be cleaved. For example, glycerol and cholesterol forms $[M-OH]^+$ ions by elimination of hydroxyl (OH) group, and signals of these peaks are intense that other molecular ions in neighboring *m/z* range.

2.1.3.8 Cationization by Alkali metals $[M+alkali]^+$

If the surface of analyte molecules is bombarded with ion beam of Cs^+ or if alkali metals like Li, Na, K, or Cs are present in the vicinity of analyte molecules under ion beam bombardment, $[M+alkali]^+$ are formed by attachment of molecule with these alkali ions, we observed such ion for uric acid sample as shown in Figure 2.6. The formation of alkali attached ions is also dependent on the chemical structure of the analyte molecule. It can be observed if analyte molecule contains basic groups or free electron pairs. In contrast to the $[M+H]^+$ formation, which is also correlated with the existence of basic groups, the $[M+alkali]^+$ formation normally do not depend on the coverage of the organic material on the metal support.

Most of the materials which show cationization with alkali metals can also be cationization by the metal substrate when prepared as monolayer on the metal substrate.

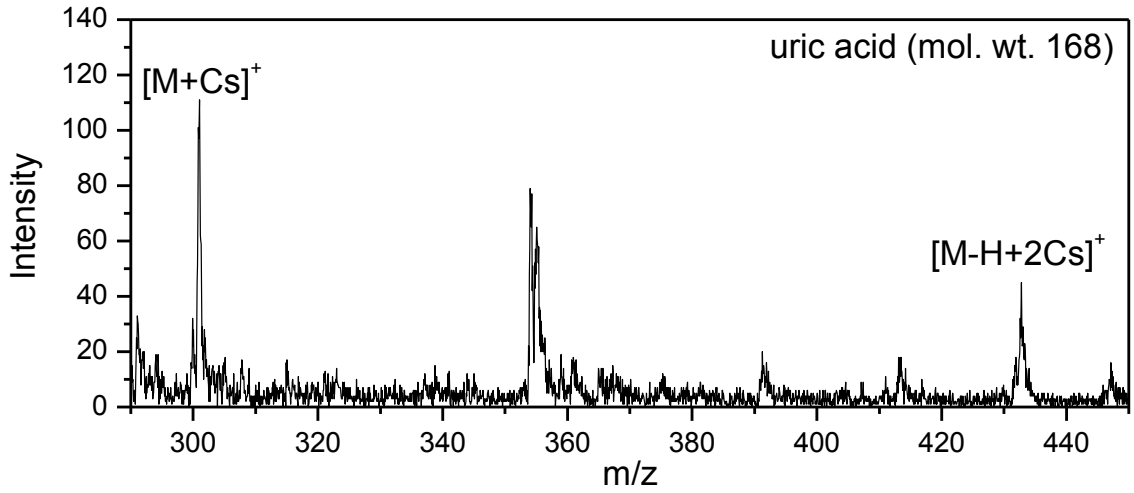

Figure 2.6. Positive TOF-SIMS spectra from the uric acid sample. Neutral Cs was deposited prior to analysis [from author´s own work].

2.2 Characterization of samples from the SIMS measurements

The fundamental unit of information of SIMS is the mass spectrum; material can be characterized directly from the experimental spectrum by assigning the observed peaks to analyte component or after some treatment on the experimental data to achieve better level of presentation.

2.2.1 S-SIMS

The mass spectrum from the inorganic samples resulting fewer peaks, are characterized by the presence of their elemental peaks as well as from the few polyatomic peaks resulting in the combination of different species present in the molecular formula of the analyte surface. In case of unknowns, libraries search is useful to compare with known compositional spectrum. In contrast in organic samples immense number of peaks arise in S-SIMS spectrum which is due to the formation of different kind of heavy ions comparable to mass of the analyte molecules as discussed before so called molecular ion peaks. These ions give direct identification of molecular species present in the surface, beside these main peaks some peaks are the direct fragment of the analyte molecule and in majority are those peaks arise due to the rearrangement of different fragments sputtered and surface degradation. The relative intensity of the molecular ion peaks and direct fragments highly depends on the many parameters already discussed e.g. primary ion mass, and energy etc. resulting from different plasma temperature at impact site. Based on this physical fact *I.S. Gilmore and M.P. Seah* proposed a method to extrapolate the mass spectral intensities at low plasma temperature called gentle SIMS (G-SIMS) intensities. This procedure makes the mass

spectrum more simple comprising only main characteristic peaks fewer than respective S-SIMS. We will briefly describe this procedure in the following section; details can be found in literature [58]. Based on this method two spectra are acquired at two different energies, or different primary ion species, or both of these favorable parameters. In this study, we proposed C-SIMS (constructive SIMS) that is based on the damage cross section which is much simpler than G-SIMS and gives relative intensities of characteristic ion peaks corresponding to initial surface conditions by eliminating the ion beam damage effect incorporated in S-SIMS.

2.2.2 G-SIMS

As we discussed above the identification of a material from the static SIMS spectra is not straightforward especially in organic materials. Mainly this is achieved by pattern recognition and comparison with library spectra. These patterns may change significantly for different ion beam species and energies with large number of ion peaks with quite different relative intensities. A method called G-SIMS was proposed [58] to reduce the large number of peaks in the static SIMS spectra produced by excessive fragmentation but to leave those peaks of ions which are more clearly diagnostic of the material. This method leaves those fragments ejected from the surface characterized by a low surface plasma temperature the state where only unreconstructed fragments are observed. As a result, the spectra are less complex, contain more structural information and are simpler to interpret. In general, G-SIMS spectra more closely look like electron ionization mass spectra than S-SIMS spectra. To retain useful intensity using a monatomic ion species, the ratio of the intensities, $I_x^+(E_2)$, for low energy E_2 to those at high energy, $I_x^+(E_1)$., gives a factor, F_x . This term is related to the effective surface *plasma temperatures* T_{p1} and T_{p2}, since T_{p1} and T_{p2} are of a quite similar magnitude where T_{p2} is less than T_{p1} by very small value of ΔT to extrapolate the mass spectrum (E_1) to further lower surface *plasma temperature* of T_{p2}-ΔT one can use F_x^2. Thus, one could use F_x^{13} or some high power to deduce the result at a significantly lower surface plasma temperature than that relevant to any of the recorded spectra, where 13 is the gentle index. Additionally m_x, the mass of emitted fragment was also introduced to further enhance the natural fall in the intensity with mass due to the transmission and detection inefficiencies. The resulting gentle intensity is derived from the following equation;

$$I_g(x) = I_x.m_x.F_x^g \qquad (2.6)$$

Where I_x is the experimentally measured intensity at $m/z = m_x$ using gentle index of g. We will explain its usefulness in real analytical sample provided by *Dr. Manoj* to confirm the

presence of cysteine on Fe_3O_4-cysteine catalyst. It might be interesting to mention here that catalyst was previously used in the application reaction.

Two S-SIMS spectra were acquired using Ga^+ as primary ion source operating at 14 keV and second with 10 keV, fixed extraction potential of +5 keV was applied to sample. The integrated intensities with *m/z ± 0.5* were divided by the total intensity of all peaks in the mass range of 0-250 and multiplied with 100; the resulting % intensities of two spectra are shown in Figure 2.7 and 2.8 respectively.

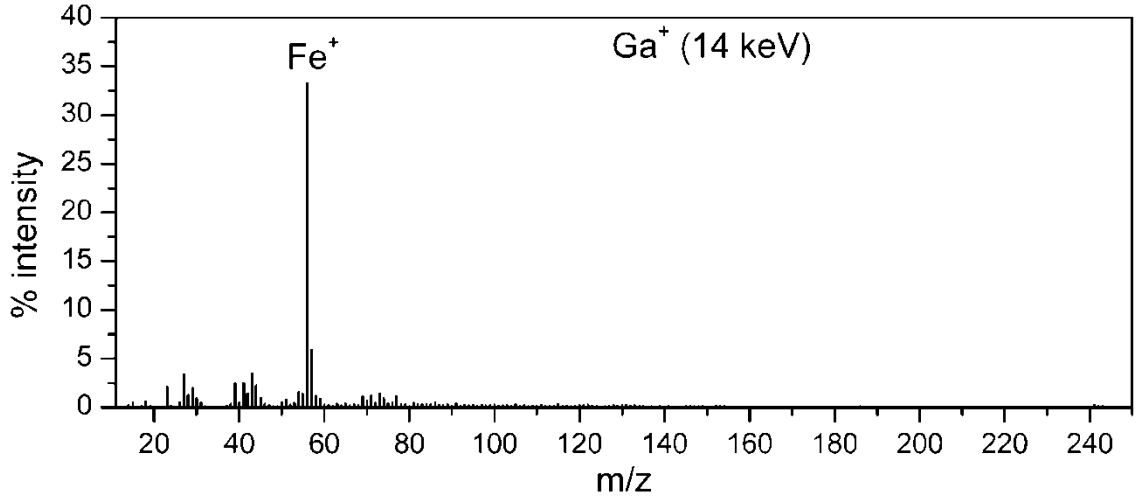

Figure 2.7. Static SIMS spectrum from Fe_3O_4-cysteine used catalyst acquired at Ga^+ impact energy of 9 keV [from present work].

To calculate the gentle factor (F_x), the respective % intensities in spectrum shown in Figure 2.8 were divided by the intensities of spectrum shown in Figure 2.7. The resulting F_x is shown in the scattered graph in Figure 2.9, the points corresponding to cysteine direct fragments and protonated molecule are indicated in the graph with respective *m/z*.

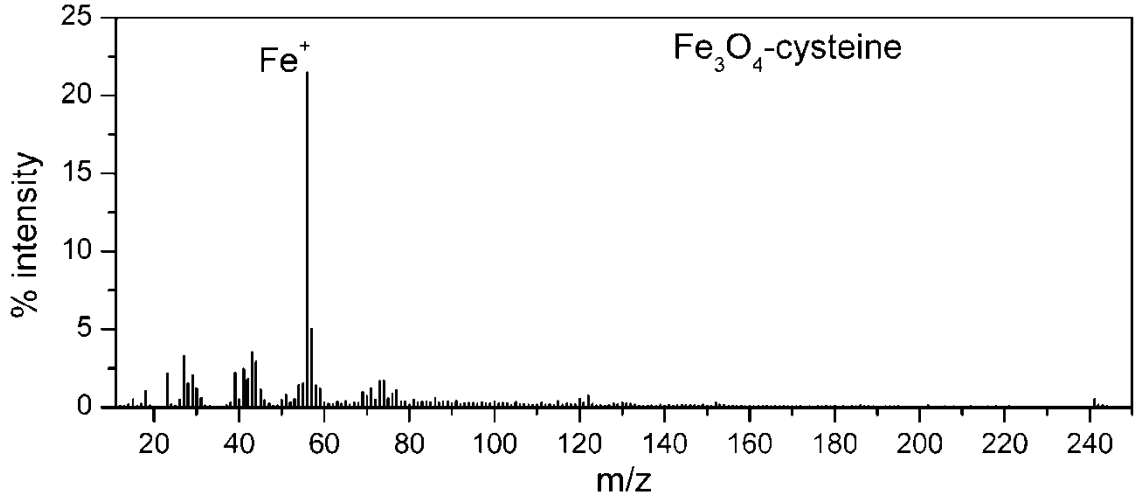

Figure 2.8. Static SIMS spectrum from Fe_3O_4-cysteine used catalyst acquired at Ga^+ impact energy of 5 keV [from the present work].

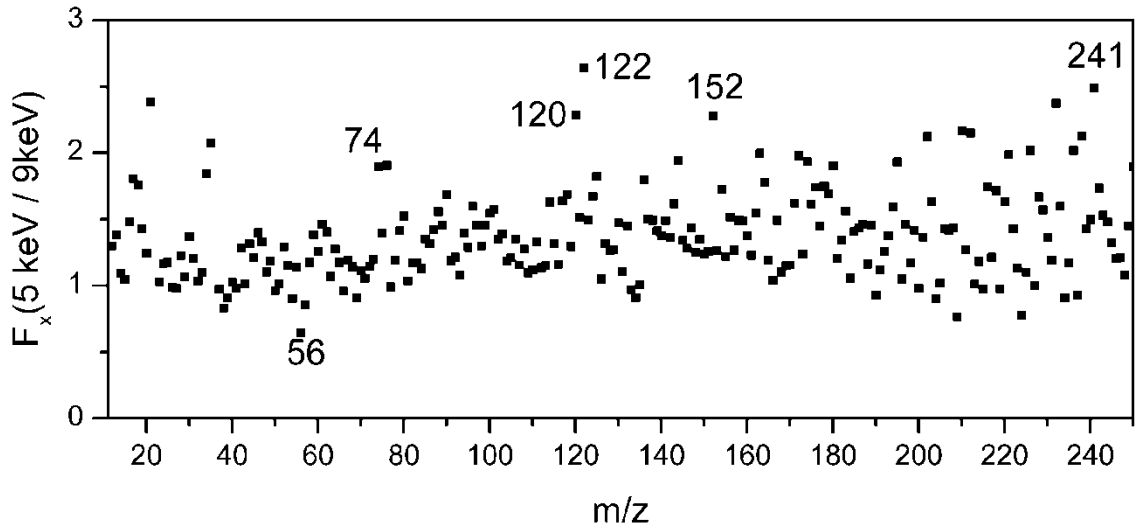

Figure 2.9. scattered plot of the respective intensity ratios of Fe_3O_4-cysteine spectra at 5 keV to 9 keV using Ga^+ ion beam with fixed extraction potential of +5 keV applied to sample [from present work].

The gentle SIMS intensity was obtained using equation (2.6) with *g-index* 2. The resulting G_2-SIMS is shown in Figure 2.10 with identified ion peaks of cystine along with the main matrix elemental peak of Fe^+ (*m/z* 56). Ion peak assignments are based on the similar samples reported elsewhere [5, 28].

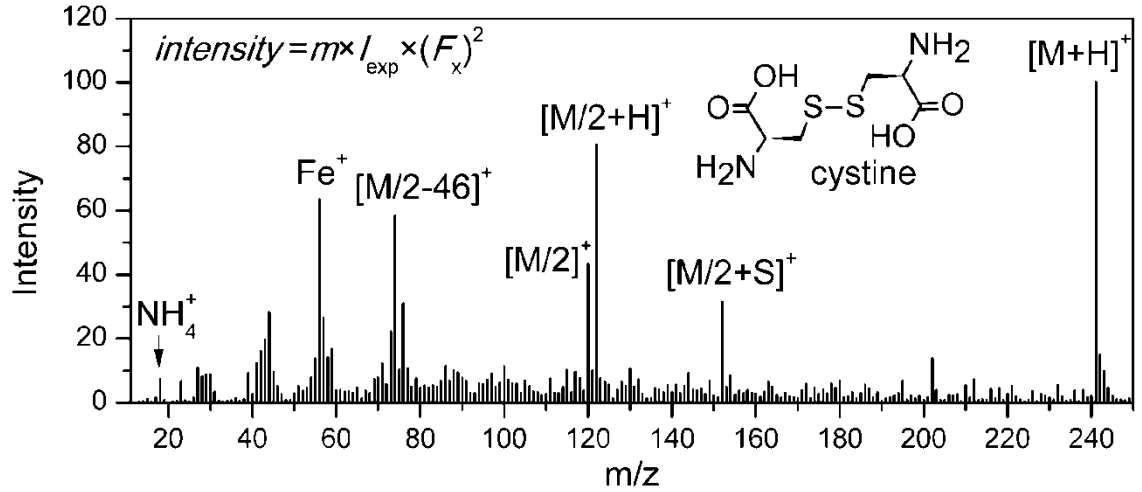

Figure 2.10. Positive ion G_2-SIMS of Fe_3O_4-cysteine spectrum, corresponding S-SIMS is shown in Figure 2.8 [part of present work].

2.2.3 C-SIMS (Constructive-SIMS)

Proposed constructive SIMS (C-SIMS) is based on another physical parameter '*damage-cross section ($\sigma_t = \sigma.t$)'*. This technique can be used to produce characteristic ion signals intensities corresponding to initial surface conditions. In S-SIMS, the intensities of the major characteristic molecular ions ($[M+H]^+$, $[M-H]^-$, $[M-OH]^+$, and $[M+alkali]^+$ etc.) and structural

fragments decreases exponentially as function of accumulative dosage i.e. the total damage cross section (σ_t) at any time '*t*'. Thus the ion yield equation (2.2) of specie *m* can be rewritten as;

$$N(t_1) = N(t_0).exp[-(\sigma_{t1} I_P)/qA] \quad (2.7)$$

$$N(t_2) = N(t_0).exp[-(\sigma_{t2} I_P)/qA] \quad (2.8)$$

Where $N(t_0)$, $N(t_1)$, and $N(t_2)$ are the ion yields of specie *m* at time t_0, t_1 and t_2 respectively, I_P is the primary ion current, *q* is charge on bombarding particle and *A* is the raster area. As all parameters on the left hand side of the equations are constant (constraint of proposed constructive SIMS) except the total damage cross σ_{t1} and σ_{t2} corresponding to low and high damaged surface at t_1 and t_2. By dividing eq. (2.7) with (2.8) will give following relation

$$N(t_1)/N(t_2) = exp(K.\Delta\sigma) \quad (2.9)$$

$$N(t_1) = N(t_2).exp(K.\Delta\sigma) \quad (2.10)$$

Where $K = I_P/qA$ is experimental constant and $\Delta\sigma = \sigma_{t2} - \sigma_{t1}$. By knowing the value of $\Delta\sigma$ one can extrapolate the ion intensity of that particular specie corresponding to theoretically further low damaged surface. The value of $K.\Delta\sigma$ can be easily calculated from the experimental data. Let us illustrate with an example.

We prepared sample on Al foil using reference chemical powder of arginine (mol. wt. 174). The molecular structure of arginine contains four NH_2 and one OH group. As we have already discussed the organic compounds containing basic $-NH_2$ give protonated molecules, and compounds containing OH group give $[M\text{-}OH]^+$. When we analyzed this sample using Ga^+ ion beam bombardment we observed the said expected ions, the intensity of protonated arginine molecules $[M+H]^+$ was much higher than $[M\text{-}OH]^+$. We collected a series of spectra from the same area and sum of the intensities of principal ions for each spectrum observed at *m/z* 18, 43, 59, 60, 70, 87, 100, 130 and 175 was plotted (Figure 2.11) as function of time (i.e. relative total damage cross section) along with calculated intensities using following equation

$$N(t) = 84067.\ exp(-0.00069 s^{-1} t) \quad (2.11)$$

Where, the constant '$N(t_0)=84067$' is the extrapolated total intensity of the selected arginine characteristic ions from the surface if each pulse of primary ion hits a surface with null total damage cross section (intact surface). We call this intensity as constructive-SIMS intensity. The contribution of each characteristic ion in the constructive-SIMS intensity is quite diverse depending upon the sensitivity of each ion to surface modification during spectral acquisition. For the present sample protonated arginine $[M+H]^+$ observed at *m/z* 175 has highest sensitivity compared to its other characteristic fragments which is obvious in the selected ion peaks plot shown in Figure 2.12.

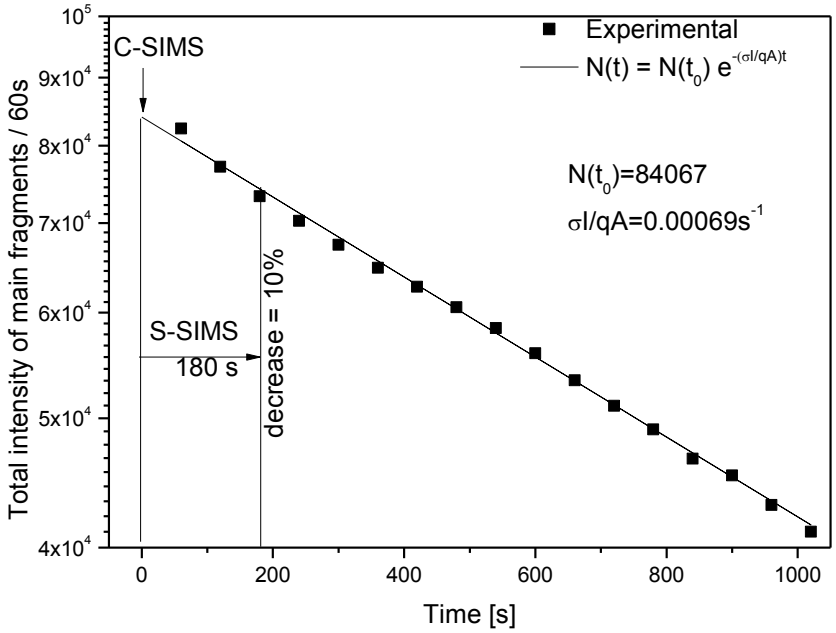

Figure 2.11. Experimental and extrapolated total intensity of arginine characteristic ion peaks. [present work].

The intensities of all ions observed in the mass spectrum can be extrapolated to lower surface damage resulting more intense intact molecular and structural species compared to rearranged fragments created during sputtering. The resulting spectrum gives higher signal intensities of molecular species compared to S-SIMS spectrum and represents very well the analyte organic molecules initially present on the intact surface. For arginine sample we observed decrease in the intensity of fragment ions observed at *m/z* 59, and 87 while increasing trend was observed for the ion peaks at *m/z* 60 and 70 up to certain time and then started to decrease.

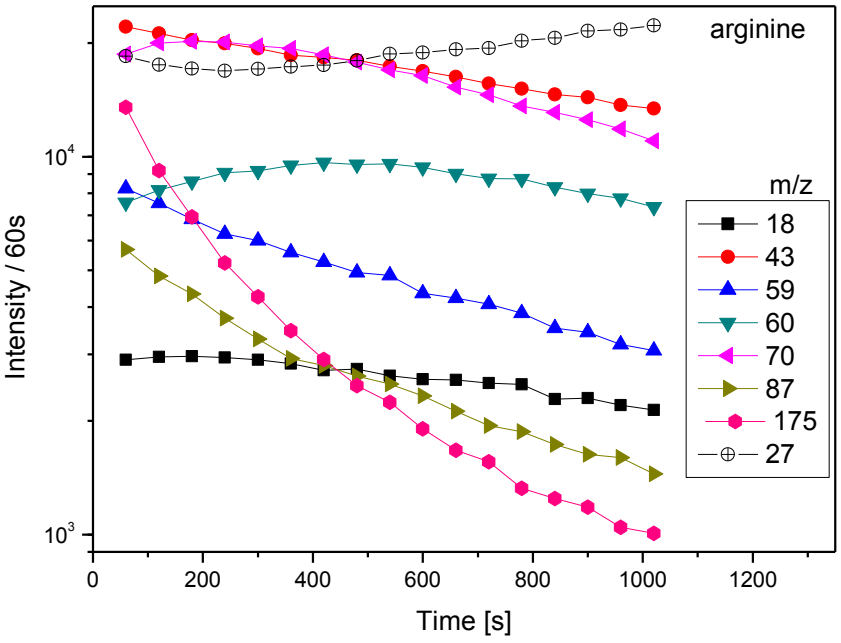

Figure 2.12. Intensities of selected peaks (m/z 43, 59, 60, 70, 87 and 175) of arginine sample as function of time (surface damage), and the ion peak of m/z 27 is mainly from substrate (Al).

The constructive-SIMS is more simple than G-SIMS, it requires two spectra with same experimental conditions (primary ion specie and energy) from the same sample area. As for as G-SIMS is concerned, every SIMS instrument facility does not have two analytical ion species, so only option left is to acquire spectra at two energies. To operate the primary ion source at two energies while controlling all parameters is also quit complicated and needs more expertise and most of the time source instability occurs.

The two consecutive mass spectra of the arginine sample acquired from the same area are shown in Figure 2.13 and follow up in Figure 2.14. We have clearly seen the decrease in the protonated molecular peak at *m/z* 175. To calculate the constructive factor F_x we divided the integrated intensity of the each ion peak of first spectrum (Figure 2.13) by respective ion peak of second spectrum (Figure 2.14), these values were then plotted as function of *m/z* as shown in Figure 2.15. The corresponding constructive factor has highest value for protonated molecules as compared to $[M\text{-}OH]^+$ and its other fragments.

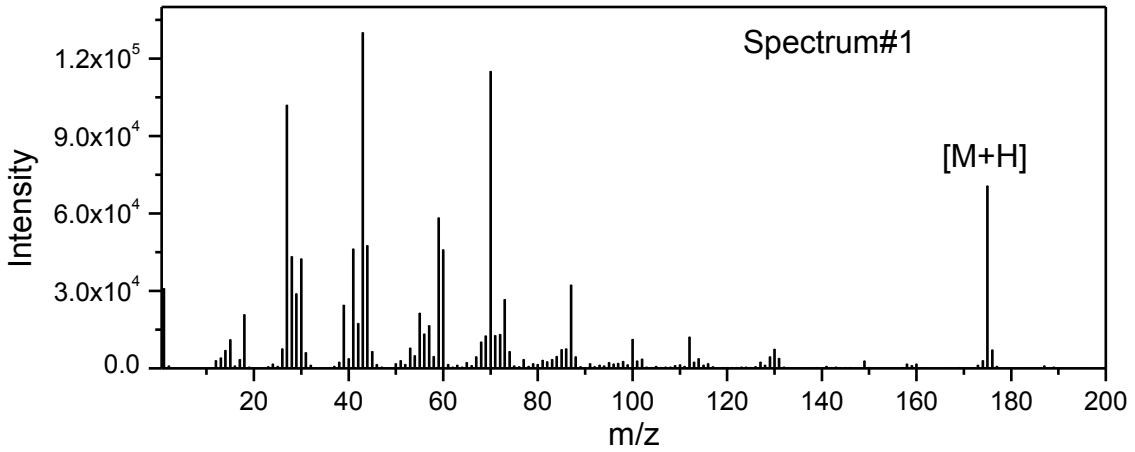

Figure 2.13. Positive ion TOF- SIMS mass spectrum (1) from arginine sample acquired at Ga^+ impact energy of 9 keV using data acquisition time of 5 minutes.

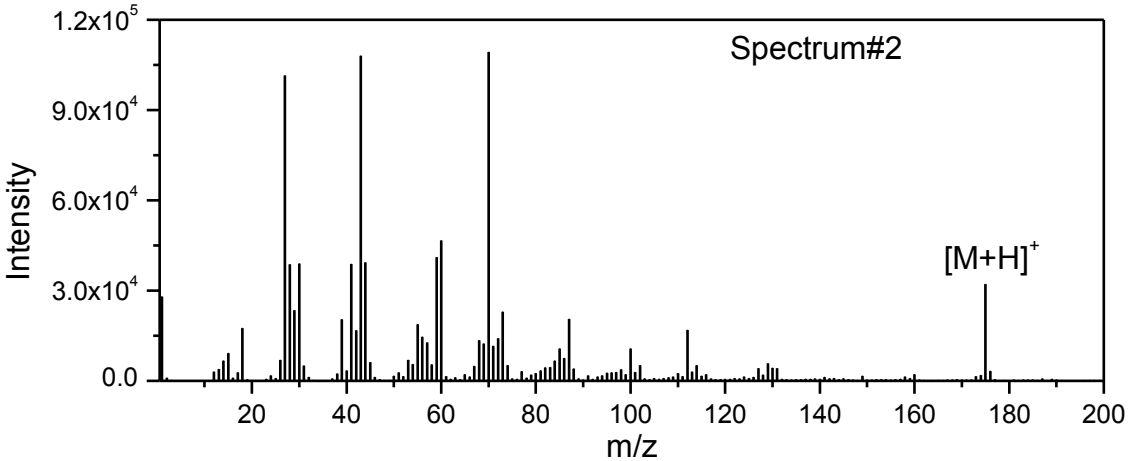

Figure 2.14. The follow-up TOF- SIMS spectrum (2) using same conditions from same area [present work].

As we observed in Figures 2.13 and 2.14, with same experimental parameter conditions the intensity of the characteristic peaks also changes in the two spectra acquired one after other from the same area. This is mainly due to damage cross section; resulting in decrease of intact molecules mainly due to rearrangement or recombination of the surface species (surface modification) under ion beam bombardment. This will decrease these species in the follow-up spectrum while enhancing the fragments produced by rearrangements is expected.

Using the constructive surface factor (F_x), the resulting C-SIMS intensity is derived from the following equation;

$$I_{C\text{-}SIMS} = I_{exp}.F_x \tag{2.12}$$

Where I_{exp} is the experimental intensity of respective ion peak.

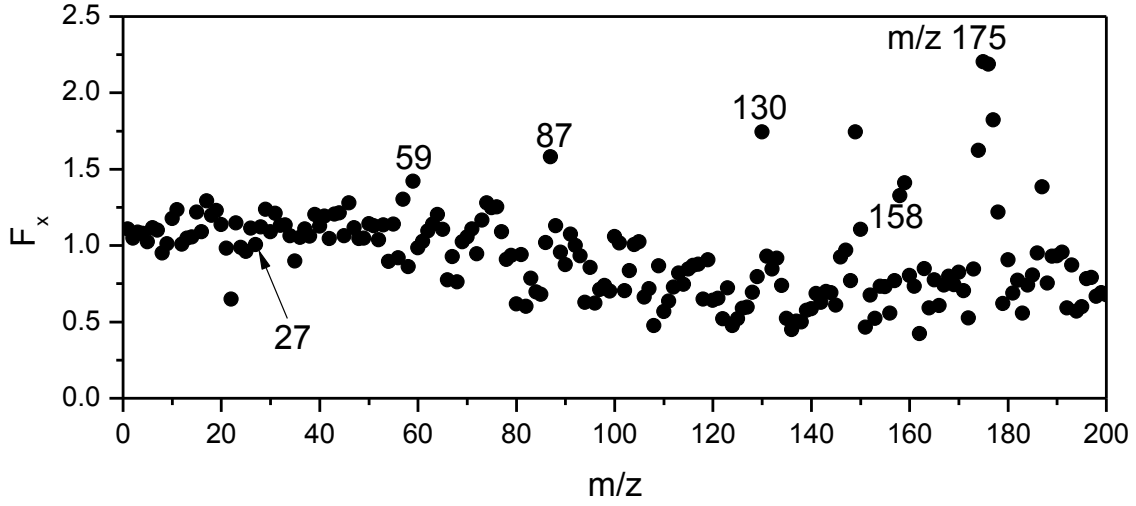

Figure 2.15. Ratio of positive ion intensities from spectra shown above acquired form arginine on Al substrate with impact energy of 9 keV Ga^+ [present work].

The enhancement in the intensities of intact fragments and protonated molecules of arginine is evident in C-SIMS spectrum (Figure 2.16) by extrapolating the experimental ion intensities observed in Figure 2.13 to more intact surface corresponding to constructive factor F_x. The resulting intensity of protonated arginine molecule is comparable to its other fragments. The fragmentation scheme is shown in Figure 2.16. From these demonstrations we can conclude that the organic samples can be clearly identified by using C-SIMS by sufficient suppressing of all the fragments against the molecular species and loss of intensity in S-SIMS can be recovered.

The modern TOF-SIMS instruments are also used in chemical imaging and depth profile modes; here we will describe briefly the principle of chemical imaging and depth profile. Although, depth profile results will not be presented here, author exploited this mode in a collaborated work using this instrumental facility on diamond like coatings and multilayer structures [59-63]. Detailed descriptions of SIMS applications can be found in literature [36].

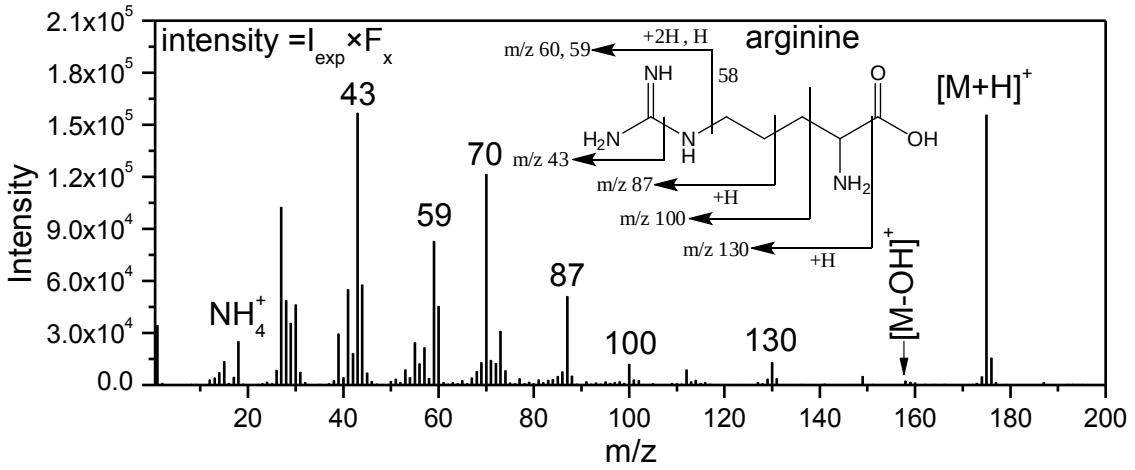

Figure 2.16. C-SIMS spectrum, corresponding TOF-SIMS (spectrum#1) shown in Figure 2.13 [present work].

2.2.4 Chemical Imaging

The spatially resolved chemical composition of a specimen is obtained by digitally raster scanning the focused primary ion beam of very small spot size (typically in nanometers) over an area of interest. A complete mass spectrum is obtained at each pixel of the raster area. The required acquisition time can be few minutes to several hours depending on the total number of pixels and the acquisition time/pixel e.g. for image of 128x128 pixels with 50 ms/pixel requires 13 minutes and 39 seconds. After the data acquisition, particular ion or combination of ions can be selected and their distribution of intensities is mapped as function of their position (X, Y). The topographic maps of the sample surface are generated from the ion induced secondary electrons (similar to scanning electron microscope) or from the total secondary ions emission which are very useful to interpret the chemical images. The topographic images are also used to focus the ion beam at particular area on the sample surface.

2.2.5 Depth Profiling

Usually in static SIMS only sub-monolayer amount of material is removed from the sample. In this case, the total area that is damaged by the ion beam after the analysis, which is the sum of the microscopic areas damaged by each ion impact, is below 1 % of the selected analytical area. If an additional high current ion beam is applied together with the pulsed ion beam, the sample is continuously eroded and the intensity of the masses of interest can be displayed as a function of the depth in a depth profile. For several years, the performance of conventional computers has been sufficient to store the time-of-flight for each secondary ion detected, together with the lateral coordinates of the corresponding primary pulse, in a raw data file. This file stores

the full information of the measurement and opens up a wide variety of post-measurement data treatment routines to be applied in order to retrieve the maximum amount of information from the data (*retrospective analysis*).

3. TOF-SIMS instrumentation and sample preparations

In this chapter, very briefly we will discuss the working principle of SIMS based on time of flight spectrometer on which the analytical work of the present study was carried out, and the instrumental upgrading will also be presented which is considered to be a backbone of the success of present project as well as plentiful collaborated work published and is being prepared to be published. As sample preparation from materials of unusual shapes (e.g. powder, wires etc.) is considered to be a challenge to produce good SIMS results, a very simple new sample preparation technique from powder inorganic and organic materials will be presented.

3.1 Principles of Time of Flight-SIMS

Since the first results from TOF-SIMS instrument based on Linear TOF analyzer reported in 1981 by Chait and Standing [64], a number of mass analyzer were proposed and instruments were built on those proposed designs. The purpose of all novel developments was to improve the quality of results in terms of resolution and performance of the analytical technique. Despite diversity in the design of mass analyzers, fundament principle is same which is quite simple although the implementation is quite complex.

The working principles and plentiful applications are described in comprehensive book on TOF-SIMS [36], and in the review articles [65-67].

Secondary ions mass spectrum generated from a single pulse is the fundamental of a TOF-SIMS instrument. The mass m of each ion with charge q is measured via its time-of-flight, generally the time taken by the ion (Figure 3.1) from the departing surface sample to detector, and is described by following equation (3.1).

$$t = L\,(m/2qU_a)^{1/2} \tag{3.1}$$

Where L is the length of analyzer and U_a is a common acceleration voltage applied to pulse of secondary ions. Since all parameters on right side of the equation (3.1) are constant under applied experimental conditions except the mass of secondary ions in the single pulse, which implies that the flight time of secondary ions is proportional to square root of their masses, providing a simple equation for time to mass calibration as follows,

$$t=a+b(m)^{1/2}, \qquad \text{or} \qquad m= [(t-a)/b]^2 \tag{3.2}$$

Where the constants ´*a*´ and ´*b*´ can easily be measured from the known mass peaks in the TOF spectrum, a typical TOF-Spectrum is shown in Figure 3.1.

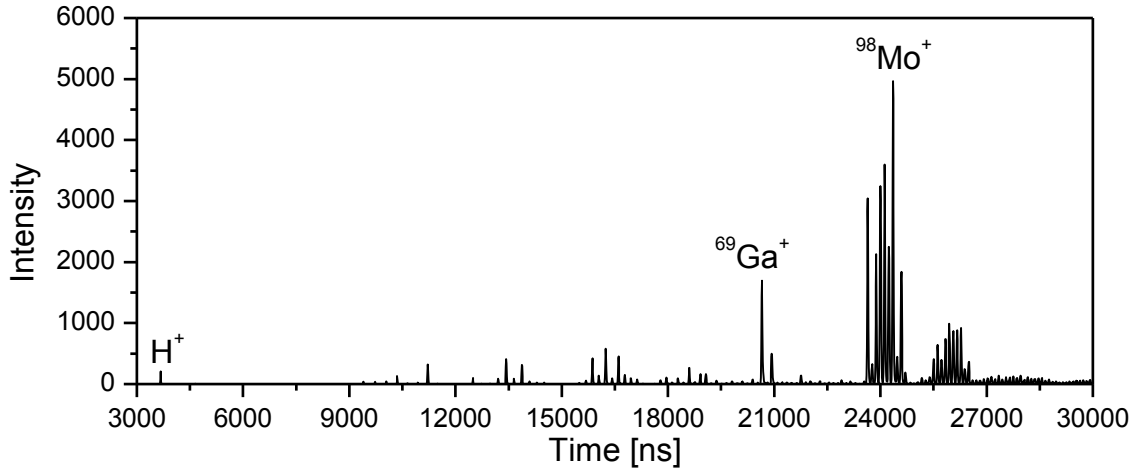

Figure 3.1. Positive ion TOF spectrum from molybdenum surface [present work]

The quality of mass spectrum depends on the mass resolution provided by the analyzer which is defined by the primary pulse width Δt_{PI}, the energy distribution leading to a flight time difference Δt_{SI} for different ions of the same mass and the uncertainty of the registration system $\Delta t_{stop\text{-}start}$, defined by following relation;

$$m/\Delta m = t/2\Delta t \tag{3.3}$$

Where

$$t/\Delta t = t/ (\Delta t^2_{PI} + \Delta t^2_{SI} + \Delta t^2_{stop\text{-}start})^{1/2} \tag{3.4}$$

Since the secondary ions are generated with an energy distribution "ΔE" of some eV width for organic species and tens of eV (1-100) for atomic secondary ions, Δt^2_{SI} dominates the mass resolution if no means of energy focusing is applied. A number of energy focusing techniques are used to achieve mass resolution of up to 10000 for organic and inorganic species. However, we will describe here Poschenrieder analyzer of medium resolution used in the subject state of art instrument.

3.2 The Poschenrieder analyzer

An energy-compensating TOF analyzer consisting of a single electrostatic analyzer (ESA) was proposed by Poschenrieder [36]. One specific analyzer system of single toroidal ESA with deflection angle of 164.4º and two drift regions of equal length of $2.37R_0$. The general geometry of the system is indicated in Figure 3.2.

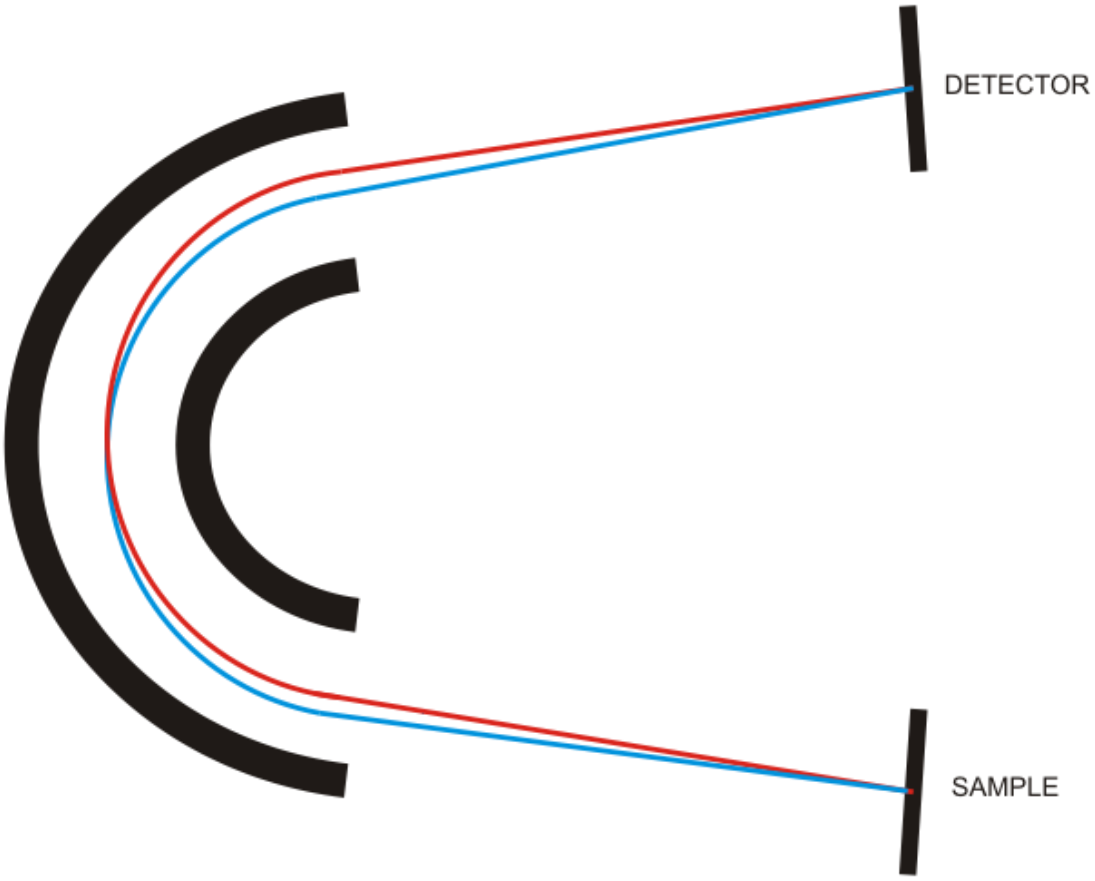

Figure 3.2a. Illustrates the focusing properties of the analyzer. An image of the source is projected into the centre plane of ESA and from there to detector. In other words, the system projects a stigmatic image from the sample to the detector. Electrostatic lenses can be employed to improve the angular acceptance of the system.

The energy focusing of Poschenrieder analyzer is illustrated in Figure 3.2b. Secondary ions of different energies disperse along the spectrometer axis in the drift region to ESA. When travelling through the ESA, the ions of higher energy penetrate deeper into the sector field than the low energy ions. At symmetry axis, the high energy ions have reached the longest part of their flight path and now "behind" the low energy ions. On the way to detector, the spacing between high and low energy ions decreases until they reach a time focus at detector.

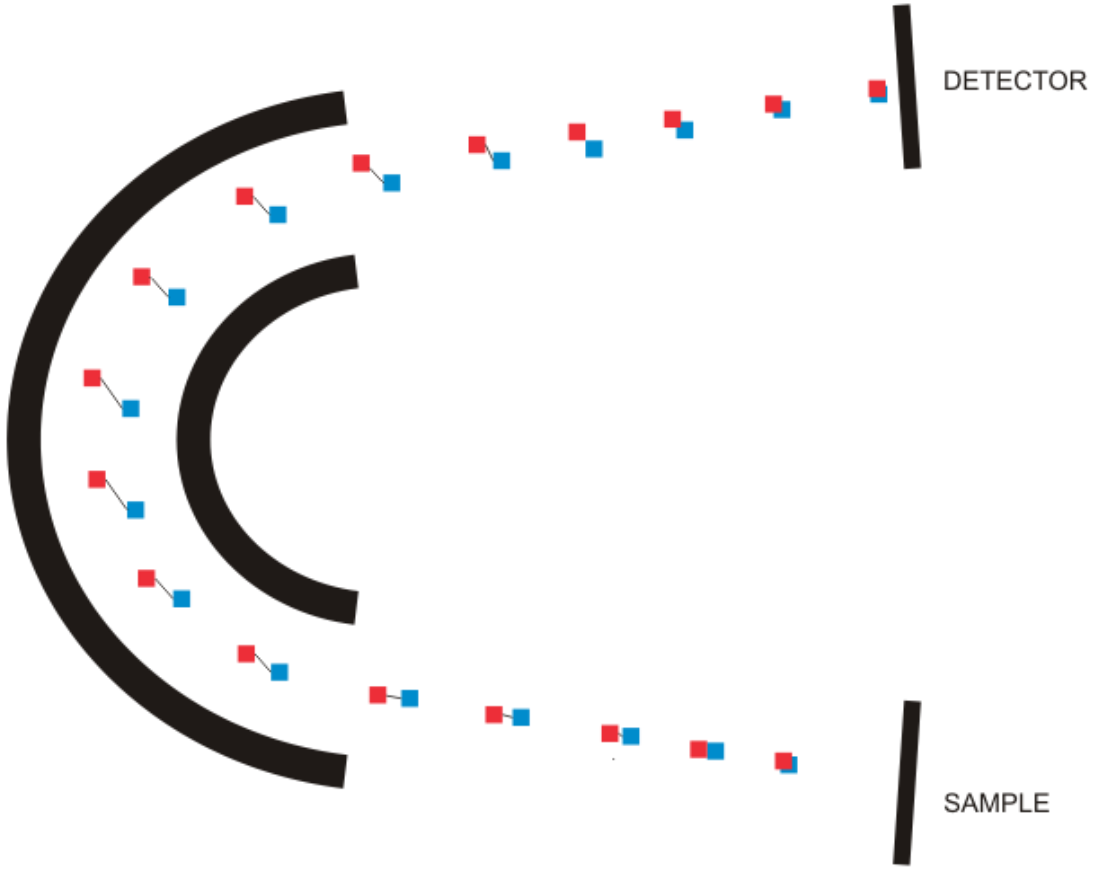

Figure 3.2b. Illustration of energy compensation of slow (blue) and fast (red) ions of same mass departing from the same spot at same time normal to the sample surface.

This relatively simple TOF analyzer system has demonstrated moderate mass resolution in SIMS. The mass resolution of 500-2000 has been reported by J. C. Vickerman and co-workers [68] depending upon the optimizing experimental adjustments.

Parallel Detection of all Masses

The most exciting feature of TOF analyzer is its capability of so called "parallel" ion detection. Because ions of different masses arrive at the detector sequentially, each pulse of primary ions generates a full mass spectrum of the surface, although the intensity in a single pulse spectrum is very low. Usually, only a few secondary ions are generated per primary pulse depending on the current density. Secondary ions of all masses are collected in parallel and the spectrum is accumulated from many primary pulses. This feature of TOF-SIMS together with the high transmission of the analyzer (typically ca. 10% compared to 1% in quadrupole mass spectrometer [68]) and the low background due to the single ion counting allows very high sensitivity for surface species.

3.3 Primary ion sources

There are mainly three types of ion sources being used in SIMS instruments as primary bombardment particles; Liquid metal ion sources, gas ion sources, and surface ionization ion beam sources. Here only the liquid metal ion source and gas ion source will be described briefly, details can be found elsewhere [36], since these are used in the equipment under description.

3.3.1 Field emission Liquid metal ion source (LMIS)

The most versatile ion source used in TOF-SIMS instruments are the liquid metal ion sources of gallium, gold, indium and bismuth. Of these, gallium is the most frequently used.

The typical assembly of gallium LIMS is given in Figure 3.3. This source comprises of a reservoir for storing a metal to be ionized and needle electrode to which the metal is fed from the reservoir to the tip of the needle through small pits formed by the chemical etching procedure of tip production. The Figure 3.3 shows the source in place with an annular extraction electrode (⌀ 1.5 mm) close to the tip of the needle.

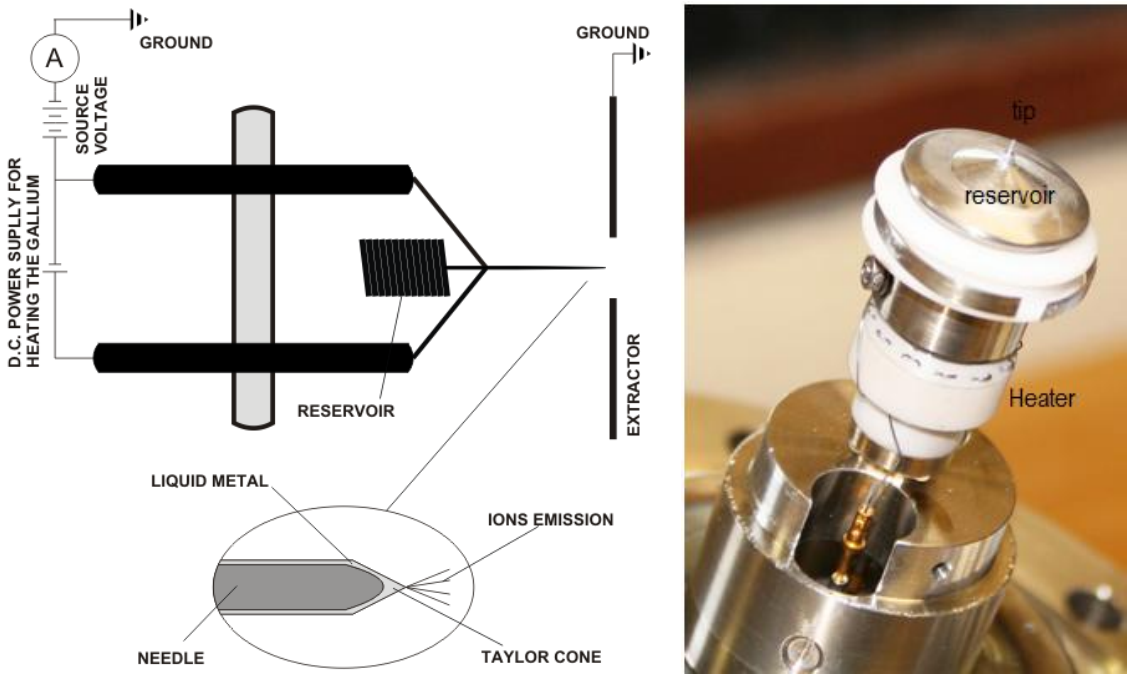

Figure 3.3. Schematic diagram of gallium liquid metal ion source along with electrical connections (left) [69, 36], Ion source assembly of MIG 300PB ion gun (right).

The source is normally mounted on an insulating mounting inside the ion gun source housing and is connected to positive high voltage source (0-30 keV) with floating heater circuit to drive the filament.

When the extractor has a potential typically in the range of -5 to -10 keV relative to source, an intense electric filed is setup around the tip of the needle. In the resulting electric force, Ga^+ ions near to the tip move forward, while electrons travel back down the needle. This results in the liquid metal extending to form a cone. The electrostatic and surface tension forces are in equilibrium when the cone has a half angle of 49.3º. This is known as Taylor cone as shown in Figure 3.4. Following the formation of the Taylor cone ion emission can start from the cusp at the apex and source moves into a state of dynamic equilibrium with a constant flow of ion current from the tip. The emission site is as small as 10 nm in diameter and so the tip of the cone forms a virtual point source. Hence the LMIS is a bright source capable of delivering high current density into small spot.

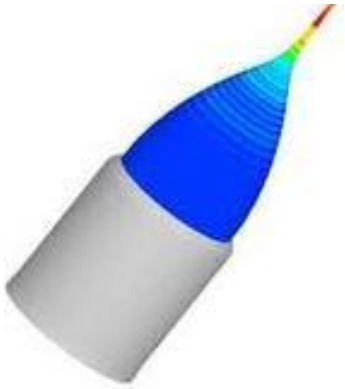

*Figure 3.4. Simulation of a Taylor Cone [70] (Flow Science Inc**).***

Stability of ion beam depends on the balance between the electrostatic forces and surface tension of the metal surface. Gallium is particularly suitable material for this type of source because of favorable properties and also its low melting point (29.8ºC). Gallium ion source can generally be run at room temperature, however, when operation is continued at room temperature, one can lose ion stability due to dynamic equilibrium disturbance of feed of gallium from reservoir to the apex of the needle.

Gallium ion source is also called work horse in SIMS, due to good stability and consistency in operation as well as relatively simple servicing compared to high mass reactive sources (indium, and bismuth and gold). These high mass species ion sources offer better secondary ion yield as compared to gallium, but they have relatively large melting points. Gold is very attractive primary ion specie for mass spectrometry; unfortunately its higher melting point (1064ºC) and tendency to vaporize in vacuum make it difficult material to use in LMIS.

3.3.2 Gas ion source

In this type of ion beam systems, gaseous elements are used to generate ions with duoplasmatron or by electron ionization, for example noble gases (Ar^+, Xe^+), oxygen (O^-, O_2^+), nitrogen (N_2^+) or even ionized cluster molecules such as C_{60}^+, or SF_5^+ (generated from SF_6). This type of ion gun is easy to operate and generates roughly focused beam of high current. These ion beam systems are often used for etching in dynamic SIMS applications.

A plasma source generally produces ion beam of high brightness. The duoplasmatron shown in Figure 3.5 is the chief example of gas ion sources. The simplest form of this ion source consists of a hollow cathode, an intermediate electrode and an anode mounted coaxially.

Gas is leaked in through gas inlet with opening at the base of cathode. When a current is applied between cathode and anode, arcs form between cathode and intermediate and between intermediate and anode. The plasma in the later space is further intensified by a magnetic field parallel with the axis which confines electron orbits close to the axis. As this plasma protrudes through a small aperture in anode an extraction field captures ions from it. In modern TOF-SIMS instruments these beams are generally used for etching rather than as analysis beams as the LMIS are better suited to applications requiring high lateral resolution.

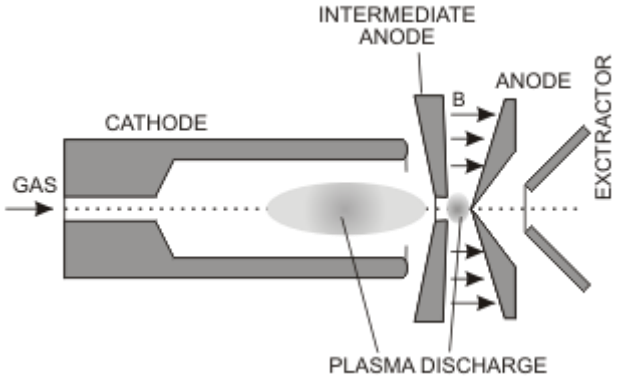

Figure 3.5: Schematic of duoplasmatron source [36]

In contrast to these conventional gas ion sources, gas cluster ion beams (Figure 3.6) has potential application in secondary ion mass spectrometry. For example, SIMS depth profile of biological samples and enhanced secondary ion yield was reported in comparison with C_{60}^+ cluster ion beam [43]. A new technique developed at Kyoto University [42] is now being used to produce low energy (<100 eV/atom) high-intensity gas clusters of average size 10,000 atoms/cluster. These gas clusters are produced when a high pressure gas (ca. 10 atm. pressure) expands into a vacuum (ca. 10-5 atm). The gas expands adiabatically and cools then condenses into clusters. Much effort has been made to increase beam currents of gas cluster ion, such as Ar_n^+. More than 1 mA of cluster beam current has been reported with typical acceleration voltages

of 20 kV [42 reference therein]. This new ion beams provide many opportunities to realize novel surface modification, such as a GCIB (gas cluster ion beam) assisted thin film deposition [42 reference therein], surface smoothing [42 reference therein] etching without inducing roughness or damage [42 reference therein], and ultra shallow ion implantation [42 reference therein]. One of the key phenomenons of cluster impact is low energy effect. As each atom in the cluster ion shares the total acceleration energy, an ion beam with ultra low energy of several eV/atom can be easily realized. For instance, when the total acceleration energy is 20 keV and the cluster size is 2000 atoms, each atom in the cluster has only 10 eV/atom.

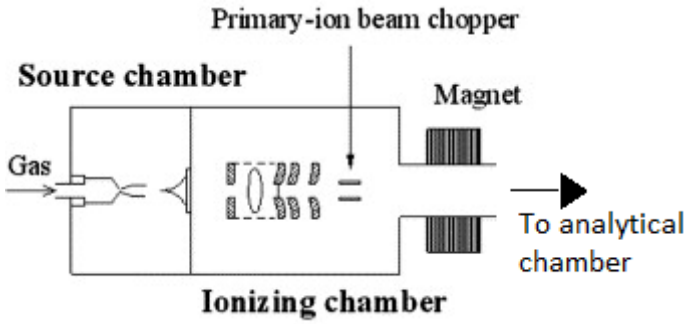

Figure 3.6: Gas cluster ion source [42].

3.4 VG IONEX TOF-SIMS instrument

In the past two decades, advances in SIMS application have stimulated the development of novel instrumentation with time-of-flight or magnetic sector mass analyzers. However, such state-of-the-art SIMS equipments are very expensive, making it affordable for a limited number of university laboratories and research centers. Simultaneously, the development of "low-cost" MiniSIMS by Millbrook [71] proved unsuccessful due to the poor analytical characteristics of this machine. Custom-built installations based on commercially available mass analyzers and ion-beam sources along with bolt-on SIMS are reasonably priced instruments as compared to standard SIMS; quite a few quality applied and fundamental investigations have been carried out using these instruments [72, 73].

An alternative approach consists in upgrading the SIMS equipped with old-fashioned data acquisition and control system, but possessing both vacuum and analytical facilities of acceptable quality.

The modernization of IX23LS TOF-SIMS developed and manufactured by VG Ionex (Burgess Hill, UK) in the mid-eighties [74, 75] was achieved as part of present work [8]. Let us describe the current state-of-the-art and main features of present developments.

The schematic diagram of an upgraded TOF-SIMS VG Ionex IX23LS is shown in Figure 3.7 and its main features are briefly summarized below. The instrument was assembled as a fully bakeable ultra-high vacuum (UHV) system composed of three stainless steel vessels isolated from each other by UHV gate valves and evacuated using Edwards EO4 diffusion pumps with polyphenyl ether pumping fluid and incorporating CCT100 liquid nitrogen cold traps. Throughout the course of the experiments the pressure in the analytical chamber is maintained at the level of (0.5–1) $\times 10^{-7}$ Pa. The duoplasmatron ion-beam column possesses two differential pumping stages, and the liquid–metal ion gun is equipped with an auxiliary 30 ls^{-1} ion pump to reduce the oxygen pressure in the source's region. The vacuum system did not undergo any major alterations, only a resistance heated evaporator with a replaceable Cs dispenser by SAES Getters (Milan, Italy) was mounted in the preparation chamber.

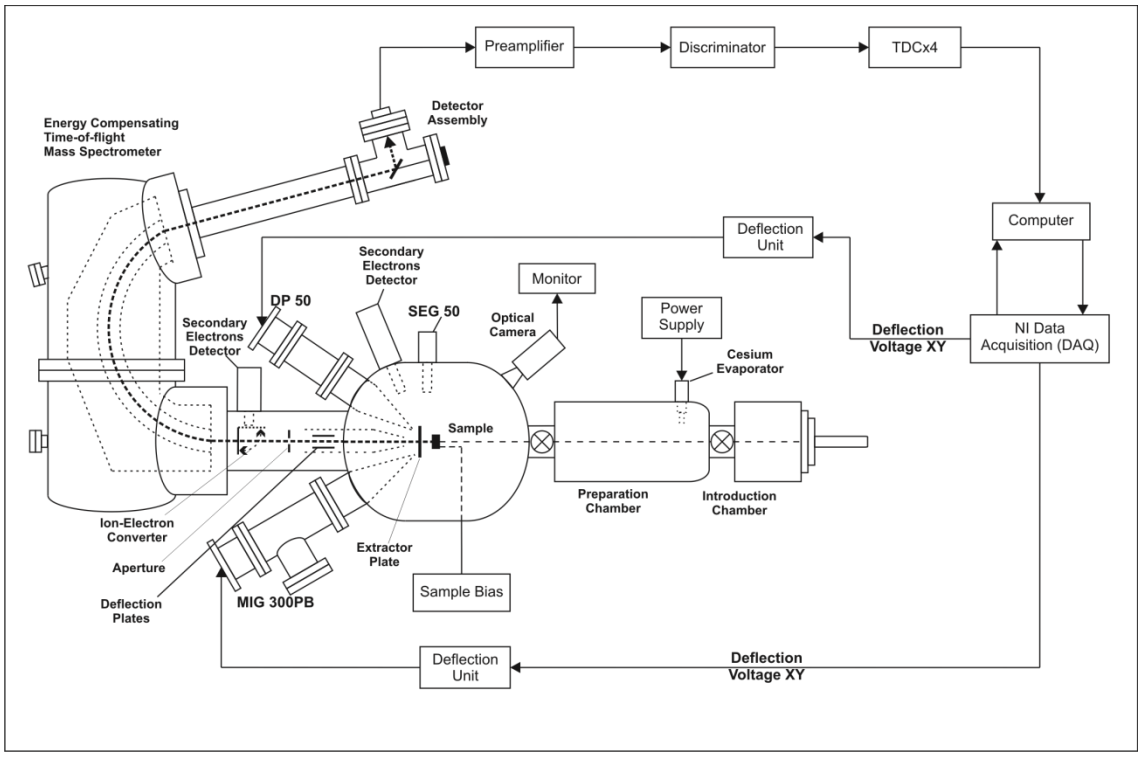

Figure 3.7. *Schematic view of the upgraded TOF-SIMS VG Ionex IX23LS [8].*

Positive and negative secondary ions are analyzed and detected using the energy-compensated mass spectrometer consisting of a 164.4◦ Poschenrieder-type analyzer [76, 78] with a flight path of 2.26 m [75] and newly installed ChevronTM MA detector assembly with two microchannel plates by Photonis (Sturbridge, MA, USA). Extraction of the secondary ions is performed along the normal to the sample surface applying ±5 kV to the sample holder; the distance between the sample surface and extraction electrode is situated between 5 and 10 mm. Typical mass resolution is 500 (full width at half maximum) and mass range is 0.5–1000 Da.

A liquid–metal ion gun MIG 300PB is used as a source of primary ions with an incident angle of 60º to the surface plane (excluding the change of the ion-beam direction due to the accelerating-retarding electric field in the space between the sample surface and extraction electrode). At present, this gun is fitted with a gallium field emitter operating at up to 30 kV; the schematic diagram of the primary ion beam column is shown in Figure 3.8.

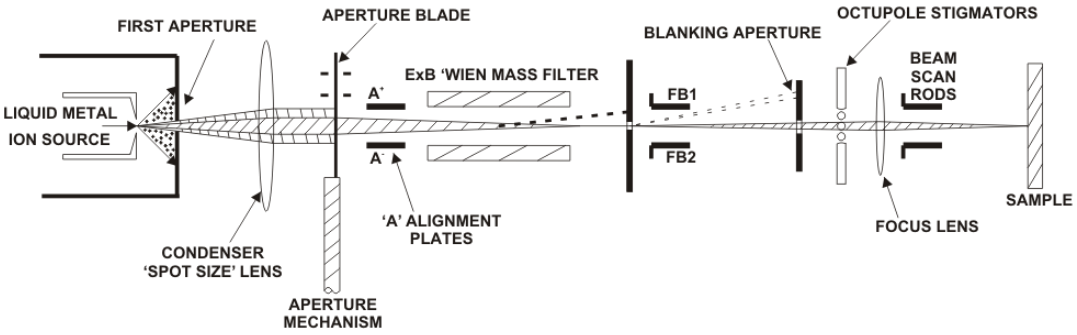

Figure 3.8. Ion beam column of MIG 300PB ion gun.

The gun has condenser and focus asymmetric einzel lenses, a Wien mass filter for separation of $^{69}Ga^+$ and $^{71}Ga^+$ isotopes, octupole stigmators and scan rods. For continuous beam with the maximum size aperture a sample current of 30 nA is obtained. In pulsed mode, auxiliary internal deflector plates chopped the ion beam producing 5–50 ns pulses with a maximal repetition frequency of 20 kHz. We repaired this ion source time to time by mechanical cleaning procedure used by SIMS community; we received the details from John Watts (Surrey University, UK). We also investigated a new procedure of wetting freshly prepared tip from the tungsten wire (⌀ 0.25 mm) and will be described later in this chapter.

SIMS depth profiling is carried out in the dual beam mode [78] using a DP50B duoplasmatron gun by VG (East Grinstead, UK) for the controlled removal of the sample materials. This gun operates with a hollow "cold" Ni cathode producing 1–10 keV O_2^+ ions with the incident angle of 60º to the sample surface. The ion-optical column contains 3 lenses (two condensers and a focus), a Wien mass filter with external magnets and scan quadrupoles. The analysis and sputter ion beams are interlaced in the course of depth profiling. At first, 12–20 keV Ga^+ pulsed beam is used to perform the analysis with ±5 kV extraction potential applied to the sample. Then, during 2–5 s the sample potential is decreased to zero, and then, a 2–8 keV O_2^+ continuous beam of 100–150 nA and 30–50 nm spot erodes the sample surface. Usually, the sputter beam is scanned over an area of 250 μm ×250 μm, and the analysis beam is directed towards the center of the sputter crater. During the delay and sputter period low-and nonconductive samples can be exposed to 5–10 eV electrons for charge compensation. For that a SEG 50 low-energy electron gun by VG is used. Physical images related mainly to the

topographical features of the sample surface are collected either with a secondary electron detector consisting of a scintillator and photomultiplier assembly fitted to the analytical chamber or with a secondary ion-electron converter placed in the entrance of TOF analyzer. This includes a metal plate mounted on a rotary feed-through and another scintillator/photomultiplier. Recently, a CCD camera for monitoring the sample position has been installed in the analysis chamber.

3.4.1 Data acquisition and control system

The schematic diagram of the newly developed 'data acquisition and control system' [8] as part of present study is shown in Figure 3.9. The system is designed around a Pentium 4 quad core computer running under Microsoft Windows7 Professional. A brief resume of the upgraded data acquisition and control system is given in Table 3.1.

Table 3.1. A brief resume of the upgraded data acquisition and control system

System component	Function and main features
Computer Pentium IV	Quad core, with PCI slots for hosting data acquisition cards. Microsoft Windows 7 Professional operating system is used.
PoschTOFSIM software	Software was developed in our lab using LabView™ platform by the National Instruments™.
National Instruments™ PCI-6259 (Austin, USA)	Used to provide 4 analog output and 2 analog input channels for the scanning and acquisition of secondary electron or total secondary ion signals: • resolution 16 bit (± 32.768) • voltage range ± 10 V • sampling rate 1.25 MS/s. It also provides 48 TTL digital I/O with the maximum clock rate of 10 MHz used for the blanking the ion beams and two 32-bit counters with plus generation capability of 10.2 ns.
Fishcamp Engineering FPCI-DIO (Santa Maria, USA)	PCI card is used to control and acquire the ion events arrival time from time-to-digital converter.
TDCx4 time-to-digital converter by IONWERKS (Houston, USA)	TDCx4 is a multi-channel single start multi-stop time-to-digital convertor used to register the ion events arrival times: • resolution 25 ps • pulse pair resolution 20 ns • in multiplexed mode pulse pair resolution 3 ns.
LeCroy 4608C discriminator (Chestnut Ridge, USA)	It converts event signal received from detector into a well defined pulse for TDC.
Chevron™ MA detector assembly	Used for the detection of secondary ions. Electron gain at 2.4 kV is ca. 10^7 (minimum)

Two PCI based data acquisition and control interface cards are installed in this computer. A PCI-6259 by the National Instruments^{TM} (Austin, TX, USA) contains four 16-bit analog output channels with a sampling rate of 2.86 MS/s, thirty-two 16-bit analog input channels with a sampling speed of 1.25 MS/s, forty eight TTL digital I/O with a maximum clock rate of 10 MHz and two 32-bit counters with pulse generation capability of 10.2 ns. This card also has triggering

and synchronization capabilities. The four analog outputs are used for scanning both ion beams using custom-built XY deflection amplifiers. The analog input channels are used to read the signal from secondary electron detectors for the physical imaging of the sample. Switching to continuous/pulsed mode and blanking/un-blanking of both ion beams are carried out via a custom-built interface board [8].

A FPCI-DIO card (Fishcamp Engineering, Santa Maria, CA, USA) is used to control a TDCx4 time-to-digital converter (IONWERKS, Houston, TX, USA) and to acquire the arrival time of each secondary ion previously registered by TDC. This card is a parallel digital interface for PC supporting the PCI expansion bus. It provides ninety-six TTL compatible signal lines, which can be configured into groups of eight to act as either input or output signals.

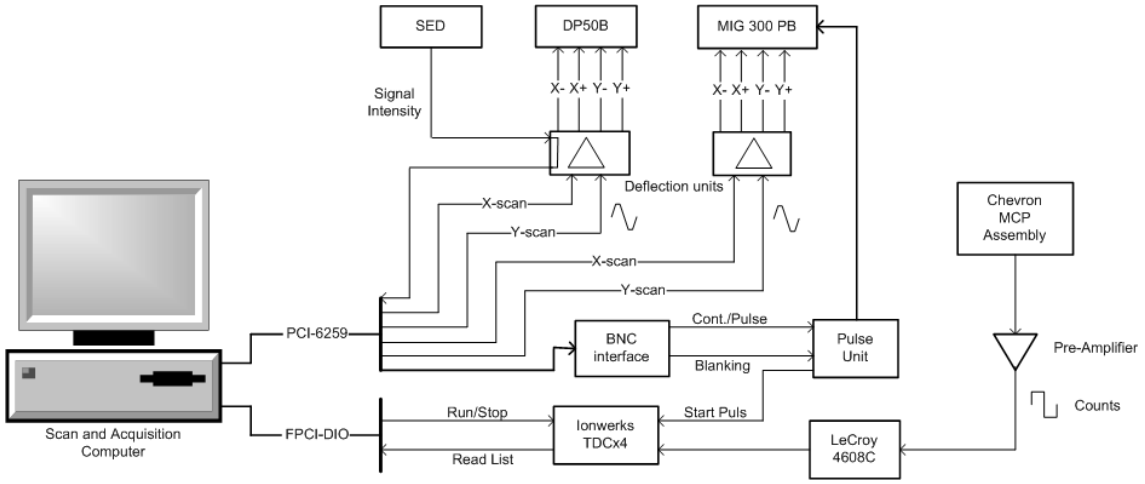

Figure 3.9. Schematic diagram of the newly developed data acquisition and control system [8].

Interconnection between the TDCx4 and FPCI-DIO is performed via three 50-pin ribbon cable headers on the card. TDCx4 is a multi-channel single start multi-stop time-to-digital convertor. It accepts standard fast signals from up to four inputs simultaneously and processes them in parallel with a digitizing resolution of 625 ps and a 20 ns worst case pulse pair resolution within each of the four channels. Alternatively, as in our case for the single-detector configuration, the input can be multiplexed into four TDC channels to increase the pulse pair resolution to 3 ns with worst case dead-time of 15 ns before the next four pulses can be encoded. Cycle time is a user-controlled input, defined through control software ranging from 2.544 to 1310 µs with 2.56 µs steps. After the secondary ions are separated by the TOF analyzer, they are detected by a Chevron^{TM} MA detector assembly with an electron gain of ca. 107 at 2400 V producing pulses with a typical duration of 650 ps. The signals are amplified before passing to a model 4608C discriminator (LeCroy, Chestnut Ridge, NY, USA), which in turn is connected to TDC [8].

3.4.2 Software

We developed dedicated software PoschTOFSIMS by using LabVIEW™ graphical programming environment by the National Instruments. Using LabVIEW™ system control software can be programmed with a significantly minimum development time compared to conventional programming languages. Now a days, a large number of scientific instruments and computer based hardware produced by National Instruments and third party manufacturers is being supported by LabVIEW™ graphical programming platform. Such support is an important factor for scientists and engineers when developing data acquisition and control software which can be easily extended / modified in future as requirements of application grow/change.

The building blocks in LabVIEW™ are virtual instruments (VIs), each designed for a specific task. These VIs are provided by the instrument manufacturers or by the National Instruments supporting third party instruments. These VIs are not available for TDC4X either by the manufacturer or by the National Instruments. We developed these VIs using DLL system files provided by the TDC manufacturer by using Call Library Function in LabVIEW™ as shown in Figure 3.10. We created VIs need for our applications by using the functions available in TDCX4.dll.

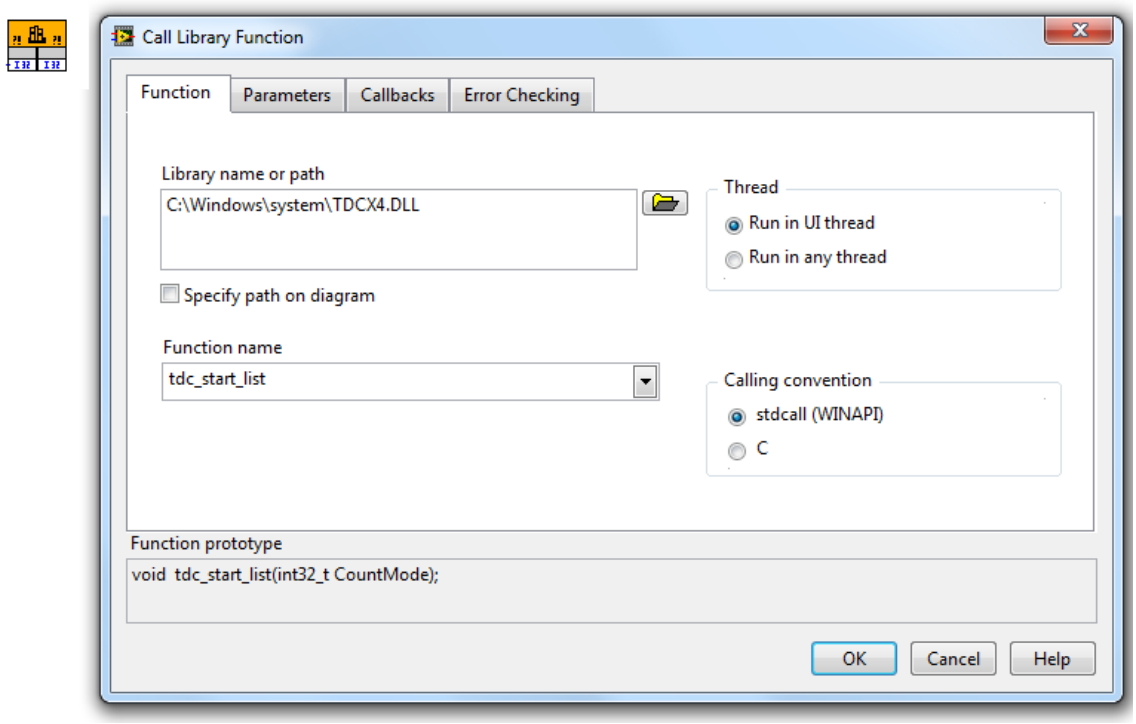

Figure 3.10. The Call Library Function in LabVIEW™ interface.

The functions in TDCx4.DLL fall into three general categories: initialization and configuration functions, spectrum definition functions, and data acquisition functions. The names of the functions are grouped by category as given below.

Initialization and Configuration Functions

```
config_datasys()
datasys_iobase()
get_histfifo()
get_histmemk()
get_tdc_id()
get_tdc_speed()
tdc_do_initialize()
tdc_do_reset()
```

Spectrum Definition Functions

```
tdc_get_actcount()
tdc_set_actcount()
tdc_get_actcountmax()
tdc_get_actcountmin()
tdc_get_acttime()
tdc_set_acttime()
tdc_map_acttime2count()
tdc_map_count2acttime()
tdc_get_histlenk()
tdc_set_histlenk()
tdc_get_histlength()
tdc_get_histtime()
tdc_get_mode()
tdc_get_histlength()
tdc_get_histtime()
tdc_get_mode()
tdc_set_mode()
tdc_get_numchans()
tdc_set_numchans()
tdc_get_numpages()
tdc_get_params()
tdc_set_params()
tdc_get_resolution()
tdc_get_shiftmax()
tdc_get_shiftmin()
tdc_map_shift2res()
```

Data Acquisition Functions

```
histogramming()
get_tdc_status()
get_shift_page()
set_shift_page()
read_histw()
report_hist()
tdc_clear_histogram()
tdc_clear_memory()
tdc_clear_events()
tdc_get_events()
tdc_clear_starts()
tdc_get_starts()
tdc_get_acquiring()
tdc_get_histogram()
tdc_map_address()
tdc_start_acquire()
tdc_stop_acquire()
tdc_get_listw()
tdc_start_list()
tdc_stop_list()
```

The description of each function can be found in the manual describing Win32 application programming interface (API) for Ionwerks´ TDCx4 Time-to-Digital Converter. This manual contains a procedure to install the software that comprises the API and description to write custom Windows software for the TDCx4 hardware. The functions given in bold face are mainly used in groups and developed following four VIs shown in Figure 3.11 for our application. The histogramming memory was not installed in our TDC so we utilized only the list mode for data acquisition.

Figure 3.11: VIs mainly used in the software to communicate with TDC and to acquire the registered time events.

The VIs can be called from the user interface and closed after completion of the task. Currently, the PoschTOFSIMS can perform the following tasks:

- Acquisition of the time spectra, followed by the recalculation of the time to mass scale,
- Sputter depth profiling in the interlaced mode with the scanning of analysis and sputter ion beams and with charge neutralization using low-energy electrons,
- Physical imaging of the sample with secondary electrons and ions (without mass separation) as shown in Figure 3.12 (Left) , and
- Chemical mapping of the sample (with mass separation of the secondary ions) shown in Figure 3.12 (middle and right) .

Ion counts are acquired from TDC in the list mode, 32 bits per stop. Data is processed and displayed in real time with a one second refreshing time, and are written to ASCII files according to ISO 22048 (2004) specifications allowing data to be analyzed by different spreadsheet analysis/plotting packages.

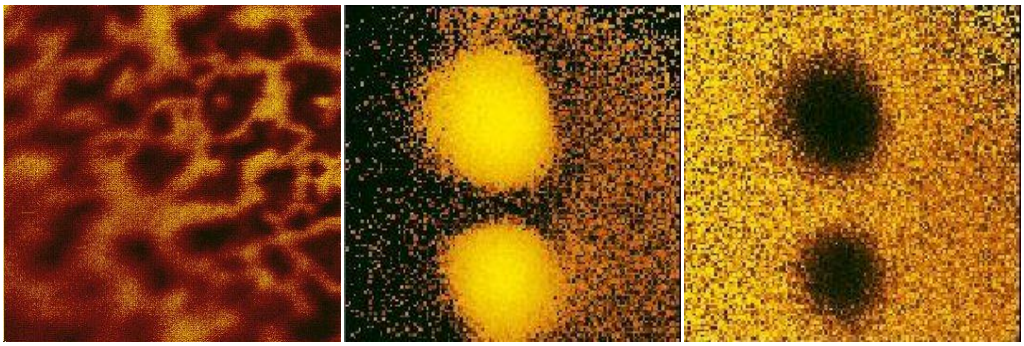

Figure 3.12. Secondary electron image giving topography of DLC sample (left), chemical image of Cs^+ spots deposited on a niobium substrate (middle), and complementary image of Nb^+. These images were acquired and processed with new data acquisition system [from authors' own work].

3.5 New tip wetting technique with gallium

Generally, tungsten wires of diameter ca. 0.20 mm are used as needle electrode for gallium ion sources. The sharp tip of conic shape at free end of the wire is produced by electrolytic process using aqueous solution of sodium hydroxide (ca. 5-15%) as electrolyte, followed by electro-polishing to one side of the tungsten wire. To improve the performance (long flashing interval) of the gallium ion source 1N aqueous solution of sodium hydroxide is

recommended instead of conventional sodium hydroxide aqueous solution. The complete length of the needle surface is also slightly polished to form a mirror surface while the needle electrode is moved vertically as shown in Figure 3.13 and a D.C. voltage of about ca. 5-10 V is applied between two electrodes. The etching along the complete length will increase the surface area along the complete length from the reservoir up to the tip of the needle ensuring better ion source stability. The stability is achieved by fine grooves (channels) produced on the surface of needle electrode by electrolytic process which permits smooth feed of a liquid metal from the reservoir to the tip of the electrode.[80]. These channels produced on the surface of the conic part of the needle are of the size of 0.1µm to 1.5 µm with density of 5×10^{4} mm^{-2} to 5×10^{6} mm^{-2} [69].

Wetting of freshly prepared needle is not straightforward in ambient conditions because of the surface contaminations, especially when it is electropolished in NaOH solution, sodium becomes major contaminant. Further cleaning with other chemicals will exchange the contaminant and after drying and then trying to wet with gallium it is impossible.

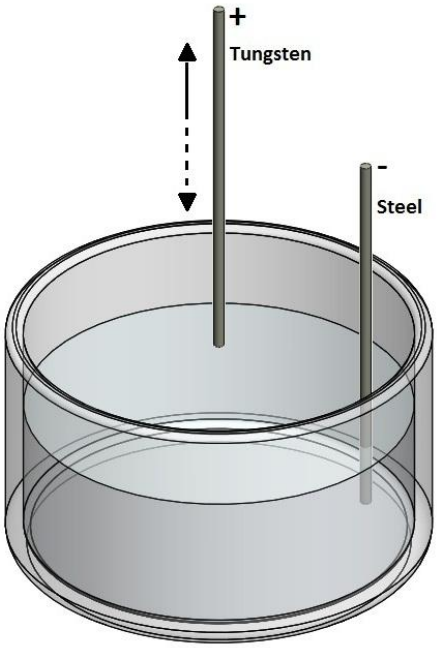

Figure 3.13. Schematic of electro-polishing of tungsten tip for LMIS.

As the objective is to wet the needle with gallium, we rinsed the prepared (described above) tungsten needle by melted gallium in ultrasonic bath at ca. 50ºC well below the boiling point of the water to avoid any water vapor contamination. In the similar manner, we rinsed the conic part of reservoir with liquid gallium under same conditions to remove any contamination especially from the capillary tube hosing the needle and to wet the capillary with gallium. Fresh gallium was used to fill the reservoir, mounted the ion source in MIG 300PB ion gun. We experienced good stability in the operation quite similar to that of commercial ion sources. In the

commercial ion sources wetting and coating of the metals [81], which are mechanically/chemically polished and chemically cleaned, are further etched by plasma treatment under UHV conditions. These contamination free surfaces of metals are then coated with plasma of desired liquid metals/alloys in same UHV or at least high vacuum conditions.

3.6 Sample preparation for SIMS analysis

Virtually all kind of materials can be analyzed by SIMS technique. The foremost constraint is that sample must be UHV compatible. There are several reasons for performing the analysis under these pressure conditions.

First, the main components of the instrument require UHV conditions for their effective operation (primary ion sources, electron flood gun, detector, etc). Secondly, it guarantees the primary ions from the ion source and secondary ions from the sample surface travel to their destinations (sample and detector) without undergoing collisions with other atoms, molecules, or ions. Third, the composition and structure of the sample remains conserved up to some extent during analysis by preventing sample contamination during SIMS analysis. Since SIMS is surface sensitive and can detect species present in the concentrations in ppm to ppb range.

The sample in the form of well defined smooth surfaces like thin films are straightforward to analyze with SIMS in reasonable physical dimensions. But most of the time samples in unusual shape (powder, fibers, etc) are to be analyzed. Powder samples are thought to be the difficult to prepare for TOF-SIMS analysis, especially the powders of organic materials with very poor conductivity. There are a number of methods described in SIMS literature [36], out of them one technique is to fix the powder on double-sided adhesive tape, or dissolve the adhesive tape in solution like acetone and use a drop of solution on conducting substrate with subsequent sprinkle of powder on the wet surface.

As the thickness and morphology of the sample greatly effects the generation of secondary ions and accordingly the stability of SIMS measurements. The cleanliness of the sample surface and the organic matrix (adhesives) greatly complicate the results and their reproducibility.

The second most popular method is to use the ´indium sandwich´ in which powder is sprinkled on one piece of clean indium foil by placing the second on top and pressing them with pressing machine. Using tweezers, the two foils are subsequently peeled apart carefully taking into account to avoid the deformation of indium sheets. Deformation in at least one sheet could be avoided by placing the sandwich on a plane surface and removing the top foil. In our study we greatly avoided deformation by using indium-powder-aluminum sandwich method. This method

ensures smooth surface preparation of powder on the indium due to low sticking of powder with aluminum foil and no deformation while removing the aluminum foil from the top.

In the above method it is quite complicated to control the thickness of the powder agglomerates. If the powder is non-conductive the secondary ion emission is greatly effected by the local thickness and even the charge compensation by the low energy flood gun becomes complicated. Furthermore, if the thickness is very small or the analyte area is partially covered then in positive ion mode the signal intensity of analyte is often suppressed by the indium (In^+). .

To circumvent this problem in the present study we used a new method in which powder is sprinkled on Al foil, a second foil is placed on top, with subsequent rubbing the two foils face to face produces very uniform implantation of fine powder particles in the aluminum surface (Figure 3.14).

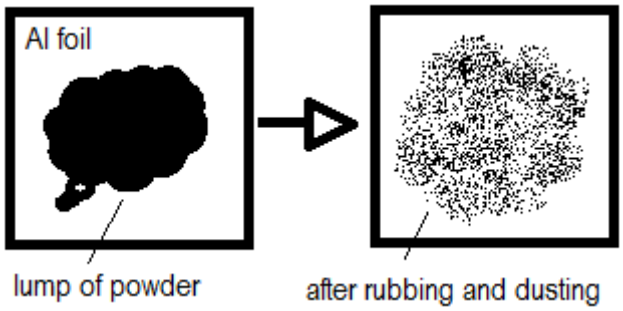

Figure 3.14. Powder on piece of Al foil (left) rubbed and dusted, the resulting sample on right

Some organic powders are waxy. In this case a face to face pre-rasping is recommended before sprinkling of the powder to produce fine scratches. Indium can also be used to prepare the sample in similar manner but indium is relatively softer than Al, while rubbing the sample powder on indium substrate the small analyte grains/particles are completely covered with indium that will decrease the analyte signal in SIMS measurements.

The other advantage is the surface contaminants detected in the reference aluminum foil are significantly negligible (Figure 3.15) as compared to indium foil as shown in Figure 3.16. The ionization potential and work function of Al (5.99 and 4.28) is also comparatively higher than In (5.79 and 4.08) resulting better ion yield for positive ion species for inorganic materials. It is also more economic material for the sample preparation.

We also observed higher molecular ion yield from the organic materials in the sample prepared on Al as compared to indium which we believe is mainly due to better conductivity due to very thin coverage of the substrate.

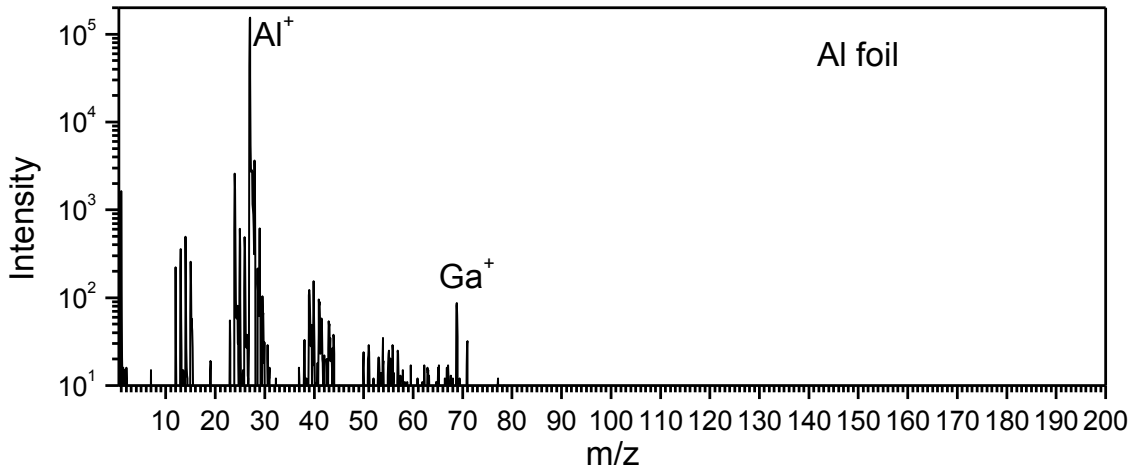

Figure 3.15: Positive ion static TOF-SIMS mass spectrum of reference Al foil without any cleaning with either chemically or sputtering with ion beam.

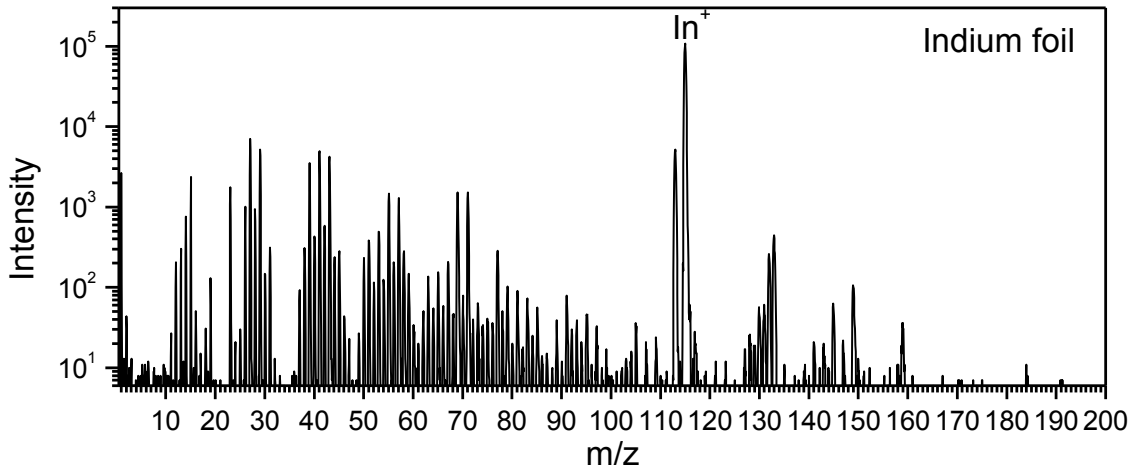

Figure 3.16: Positive ion static TOF-SIMS mass spectrum of reference indium foil scratched with clean knife.

3.7 TOF-SIMS analysis reference chemicals and stones

Thirty eight stones were collected from different patients at the Hospital Garcia de Orta (Almada, Portugal). The samples were rinsed with pure deionized water and then packed in special containers for transportation. In our laboratory the calculi were milled in an agate mortar and pestle into a powder of uniform and small grain size representative of its composition. The samples were prepared either pressing the powder on a 5N quality indium foil (Goodfellow, Huntingdon, UK) as described in sample preparation techniques [26-29] or rubbing the powder on the aluminum foil especially for organic samples to improve the conductivity and uniformity of the sample. The samples of reference commercial compounds were prepared in a similar manner to the human calculi. The reference compounds used in this study are listed in Table 3.2.

Table 3.2. List of the commercial kidney stone minerals used as reference samples in this work

Group	Appellation	Mineralogical name	Formula	MW(D)	Supplier
Organic	Cystine		$C_6H_{12}N_2O_4S_2$	240	Acros(Geel, Belgium)
	Cysteine			121	Acros
	Uric acid		$C_5H_4N_4O_3$	168	Acros
	Sodium urate		$NaC_5H_3N_4O_3$	190	Acros
	glyerol			92	Acros
Oxalates	Calcium oxalate monohydrate	Whewellite	$CaC_2O_4.H_2O$	146	Alfa Aesar (Karlsruhe, Germany)
	(dihydrate)	(weddellite)	($CaC_2O_4.2H_2O$)	(164)	
Calcium phosphates	Calcium hydrogen phosphate	Monetite	$CaHPO_4$	136	BDH (Poole, UK)
	(dihydrate)	(brushite)	$CaHPO_4.2H_2O$	(172)	
	Calcium dihydrogen phosphate monohydrate		$Ca(H_2PO_4)_2.H_2O$	252	Panreac (Barcelona, Spain)
	Tri-calcium phosphate	Whitlockite	$Ca_3(PO_4)_2$	310	Panreac
	Hydroxyapatite	HAP	$Ca_5(PO_4)_3OH$	502	Acros
Magnesium and potassium phosphates	Ammonium magnesium phosphate hexahydrate	Struvite	$NH_4MgPO_4.6H_2O$	245	Alfa Aesar
	Magnesium hydrogen phosphate trihydrate	Newberyite	$MgHPO_4.3H_2O$	174	Acros
	Potassium hydrogen phosphate		K_2HPO_4	174	Merck (Darmstadt, Germany)

TOF-SIMS analysis was accomplished with an upgraded VG Ionex IX23LS TOF-SIMS instrument (Burgess Hill, UK) already described in this chapter. For SIMS measurements, we used a pulsed (40 ns/6 kHz) Ga+ ions with 14 keV bombarding energy. The focused ion beam was digitally raster scanned (128×128 pixels) over an area of ca. 750 µm×750 µm. Extraction of secondary ions from the sample is performed by applying a high voltage (±5 kV for positive or negative ions, respectively) to the sample holder. At his acceleration voltage the mass analyzer gives the maximum transmission as shown in the Figure 3.17.

For each standard chemical and stone sample we acquired SIMS data from as prepared sample without any pre-sputtering and after controlled sputtering. However, in general (otherwise will be explicitly mentioned) for the data presented in the present work, no sputter cleaning of the organic samples was performed by either source in order to conserve the molecular information in a set of positive and negative mass spectra. While, pre-sputtering was done for inorganic samples with ion dose of ca. $2\text{-}5\times10^{13}$ ions/cm^2. We found this dosage sufficient to

remove the surface hydrocarbon contaminations to achieve better reproducibility and accuracy in quantification measurements.

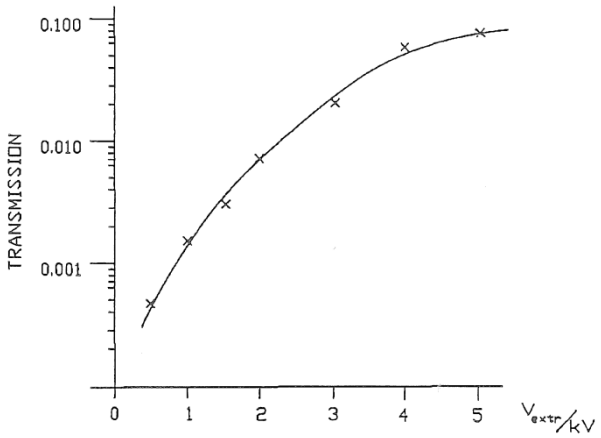

Figure 3.17. Variation of spectral intensity with secondary ion extraction/acceleration voltage, measured for Mo^+ from oxidized molybdenum sample [68].

4. TOF-SIMS analysis of organic calculi

There are two main organic urinary components found in kidney calculi. First is uric acid the one with most frequent occurring component found in our study, and the other is cystine that is the least frequent in humans. Analytical results of uric acid salts will also be discussed. In one of the urates (uric acid salts) containing stones, we found 4-deoxypyridoxine 5-phosphate which is a metabolite of vitamin B6 [27]. We suggest that its presence is due to the consumption of foods with high vitamin B6 content, or due to the use of vitamin B6 as a medication to prevent the growth of calcium oxalate kidney stones [82]. We also determined that the major component of this stone was sodium dihydrogen phosphate. The identification of cystine stones will also be made clear by the presence of its protonated/deprotonated molecular and characteristic fragment ions and we will also compare human stone analysis with that of dog stone. Finally the result of cholesterol gallstone will be presented, although it is not urinary calculus this sample shows that the application of present study with TOF-SIMS is not limited to urinary stones analysis but has a broad scope in similar biomaterial applications.

Although, the purpose of this work is to demonstrate the suitability of SIMS for the compositional characterization of calculi, the prevalence and pathophysiology of this disease is summarized below, as described in the literature found.

4.1 Uric Acid stones

Uric acid stones constitute ca. 8–10% of all kidney stones [83]. The global prevalence of uric acid (UA) stones is heterogeneous, with its highest prevalence in the Middle East [84] and in certain parts of Europe [85]. In the Midwestern region of the United States, the prevalence of UA stone formation has been shown to be exceedingly high. This abnormal tendency toward UA stone formation may be influenced by specific dietary habits of consuming a large amount of

purine with each meal. Over the past decade, major progress has been made in our understanding of the pathophysiologic mechanisms of UA stone formation. A preliminary study initially described a high prevalence of UA stones among patients with type 2 diabetes mellitus [86]. In studies following, a high prevalence of uric acid stones was also shown in obese patients [87, 88]. Furthermore, it was later described that higher body mass index and type 2 diabetes mellitus are independent risk factors for UA nephrolithiasis, and the prevalence of UA stones further rises with higher body mass index in the presence of type 2 diabetes mellitus [89]. These observations were consistent with multiple large epidemiologic studies displaying a link between obesity, weight gain, type 2 diabetes mellitus, an aggregate of features that are characteristic of the metabolic syndrome, and UA nephrolithiasis [86-90]. Different types of uric acid crystals are found in stones and are frequently combined with calcium oxalates.

Uric acid is the end product of purine metabolism in humans. In other mammals uric acid is further broken down into allantoin by the enzyme uricase. Allantoin is 10 to 100 times more soluble compared with uric acid. Humans and Dalmatian dogs are the only known mammals prone to uric acid stone formation. However, the mechanism of stone formation in the Dalmatian dog is related to an increased fractional excretion of uric acid [91].

Uric acid (2, 6, 8-trioxypurine) is a weak acid with 2 dissociation constants. Two factors contribute to uric acid solubility: uric acid concentration and solution pH. However, the solubility of uric acid in urine is primarily determined by urinary pH. The supersaturation of urine with uric acid occurs when urinary pH is less than 5.5. Uric acid stone formation requires supersaturation of urinary uric acid. Three factors contribute to the formation of these calculi: acidic urine, hyperuricuria and decreased urinary volume. One or more of these conditions may coexist in a specific patient and contribute to stone disease severity. All conditions contributing to acidic urine and low urinary output will increase uric acid supersaturation that promotes uric acid stone formation [92].

The color of uric acid stones varies from light yellow via red-yellow to red-brown [90]. Higher the content of uric acid hydration, more intensive the color in admixed stones. Their surfaces are mostly smooth. The urate stones mostly have a white to gray color with loose consistency.

The results of 8 stones listed in Table 4.1 will be presented in this chapter. The samples were prepared on indium and aluminum substrates according to two sample preparation techniques discussed in chapter 3 for respective substrate (cf. 3.6 and 3.7). The mass spectra presented here were acquired without presputtering.

Table 4.1. Experimental conditions and classification of organic stones analyzed

stone sample	presputtering	substrate used	classification with TOF-SIMS
UA1ǂ	No	Indium	uric acid
UA2	No	Al	uric acid
UA3	No	Al	uric acid
UA4	No	Al	uric acid
UA5	No	Al	uric acid
UA6	No	Al	uric acid
Urate1*	No	Indium	Na/K-urate
human cystine *	No	Al	cystine
dog cystine	No	Al	cystine
cholesterol*	No	Al	cholesterol

The symbol (*) corresponds to our results published in Ghumman et al. [26-28].

4.1.1 TOF-SIMS analysis of uric acid stones

The molecular structure of uric acid is shown in Figure 4.1. First sample (UA1, ca. 6mm × 4mm in size) that we are discussing here came from a 60-year old male patient with a diagnosis of ureterolithiasis and diabetes mellitus type 2, it was slightly soft with a rough surface of yellowish brown color. The powder produced from the stone was pressed in indium foil. The sample was highly nonconductive and charge compensation was used during analysis.

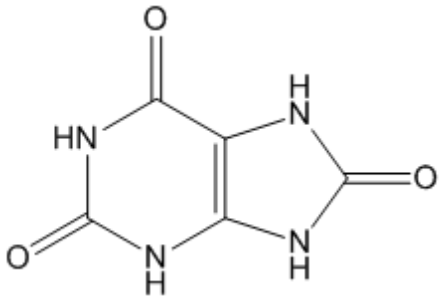

Figure 4.1. The molecular structure of uric acid; mol. wt. 168

The negative TOF-SIMS spectra of the human stone and reference uric acid are shown in Figure 4.2. The two spectra look very similar; the most intense molecular ions above *m/z* 100, are observed at *m/z* 167 followed by 124 are assigned to deprotonated uric acid $[UA\text{-}H]^-$ and its fragment $[UA\text{-}H\text{-}HCNO]^-$ the molecular structure of these ions are shown in Figure 4.3 the assignment of these ions are in accordance with Gorman et al. [93] study on uric acid samples extracted from human urine. Additionally, very small intensity of deprotonated xanthine molecules at *m/z* 151 was observed for both reference uric acid and stone samples which are believed to be a fragment of uric acid form by the loss of oxygen from deprotonated molecule. The two cyanide ion peaks at *m/z* 42 and 26, assigned to CNO^- and CN^-, are also characteristic to uric acid [26].

In principle, the characteristic peaks appearing in the negative ion spectra confirm the presence of uric acid. However, for the detection of electropositive elements and their compounds

we have also acquired the positive ion TOF-SIMS spectra. In the range above *m/z* 100 (Figure 4.4) protonated uric acid $[UA+H]^+$ at *m/z* 169 is the dominant ion peak. Other key ions here are at *m/z* 153, which correspond to protonated xanthine resulting from fragmentation of protonated uric acid molecule by the loss of oxygen $[UA+H-O]^+$, and *m/z* 126. The latter ion is a typical fragment ion for xanthine and uric acid, generated by loss of HCN and HCNO, respectively, from their protonated molecules $[M+H]^+$. The possible molecular structures of these three ions as well as sodiated uric acid molecule are shown in Figure 4.5.

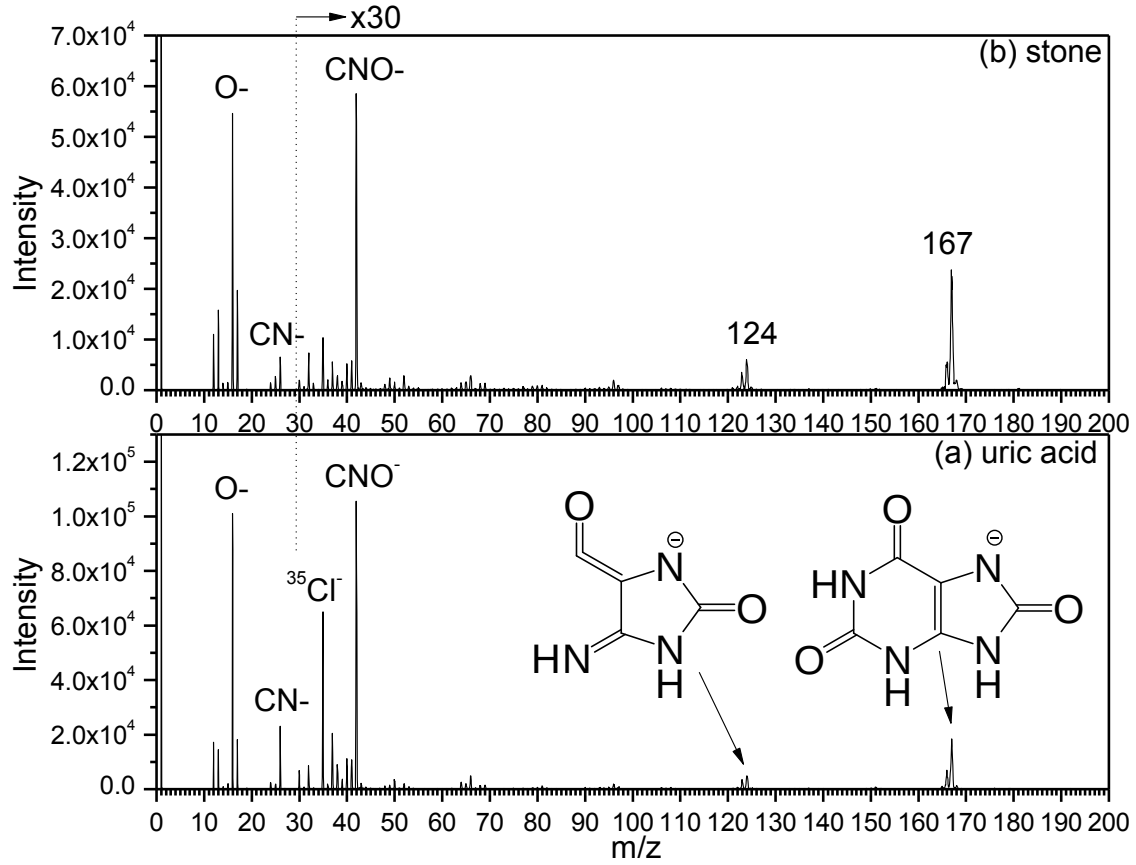

Figure 4.2. Negative ion spectra of reference uric acid (a) and that of human stone UA1 (b) [48].

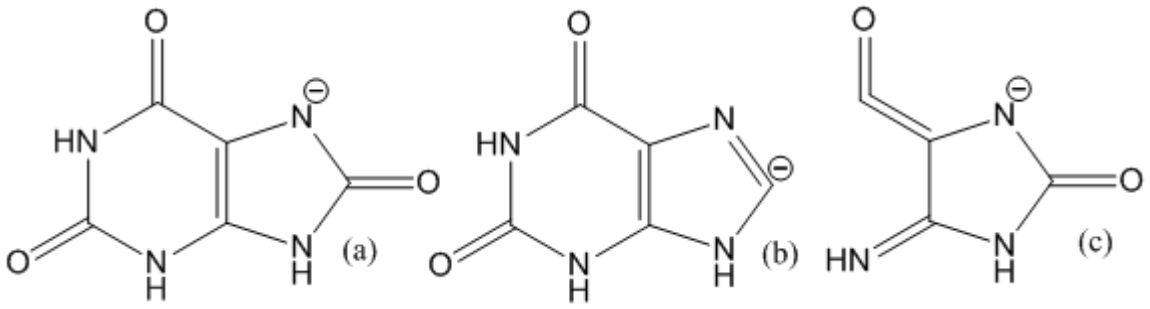

Figure 4.3: Possible structure of negative ions observed at m/z 167 (a), 151 (b), and 124 (c).

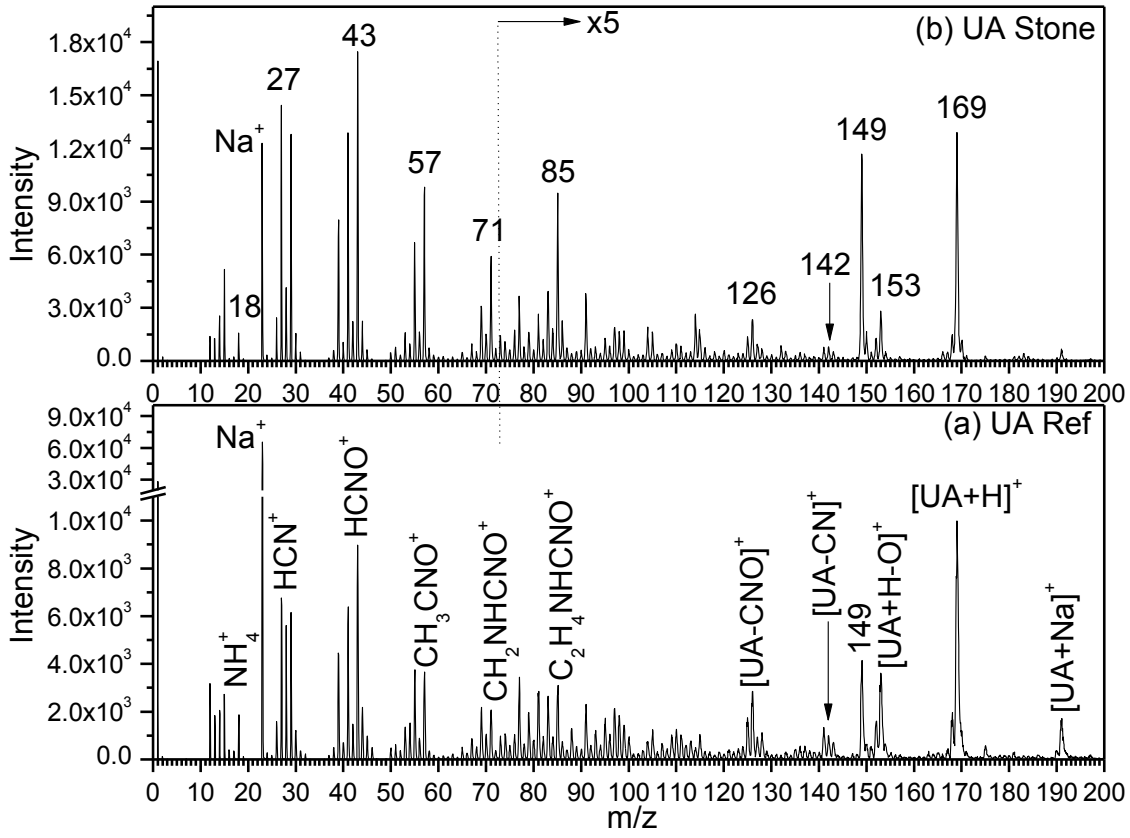

Figure 4.4. Positive ion spectra of reference uric acid (a) and that of human stone UA1 (b).

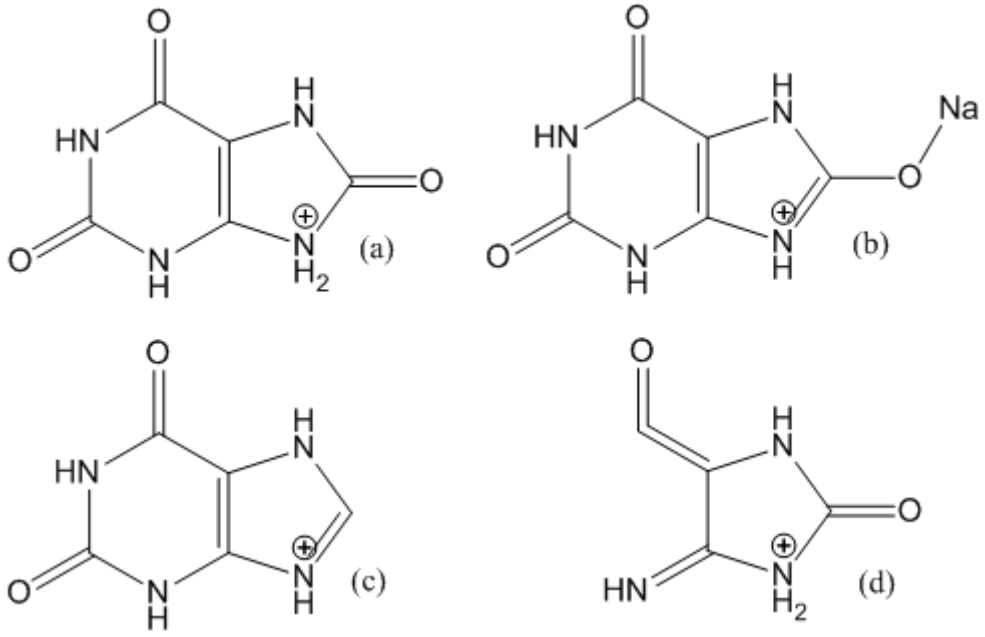

Figure 4.5: Possible structure of positive ions observed at m/z 169 (a), 191 (b), 153 (c), and 126 (d).

Similar ions are revealed in the lower mass range for the kidney stone and the uric acid reference except for the presence of the Na^+ peak at *m/z* 23. This peak is more intense in the synthetic uric acid reference (Figure 4.4a) than in the naturally occurring kidney stone (Figure

4b). For this sample, we also observed the sodiated uric acid molecule $[UA+Na]^+$ at *m/z* 191 due to presence of sodium as impurity in the reference chemical. The other major ions at *m/z* 27, 43, 57, 71 and 85 correspond to HCN^+, $HCNO^+$, CH_3CNO^+,CH_2NHCNO^+ and $C_2H_4NHCNO^+$. Thereby, the human kidney stone analyzed here was identified as being pure uric acid. It is important to mention here that the most intense peaks in the electron ionization spectrum of uric acid are at *m/z* 43 and 125 (see the NIST Mass Spectral Library14).

If we look on the positive mass spectra, the ion peak at 149 is observed for both reference chemical and urinary stone samples, the intensity of this peak is comparable with that of protonated uric acid in the human stone sample. In our preliminary study we observed this peak but could not assign it. Is it a fragment of uric acid? Let us try to understand its origin in following section by comparing with other stones identified as uric acid.

4.1.2 Comparison of uric acid stones by scattered intensity plots

The two stones shown in Figure 4.6 were identified as uric acid stones (UA2, UA3) on the basis of the ion pattern observed and discussed above for UA1. The mass spectra (Figure 8.1a) from both stone samples were quite similar except the relative intensities of few peaks e.g. at *m/z* 149. The integrated intensities in the range of ±0.5 at each *m/z* were normalized by dividing with total intensity of all ions observed in the *m/z* range of 0-200 and scaled by 100.

(a)  (b) 

Figure 4.6. Morphological appearance of the stones identified with TOF-SIMS as uric acid UA2 (a) and UA3 (b).

The results from these stones (UA1, UA2, and UA3) are directly comparable; the relative intensities of corresponding ion peaks are shown in the scatter plots in Figures 4.7a and 4.7b along with the outputs of linear regression analyses. The UA1 compares very well with UA2, giving a slope agreement within 3 % and a relatively small intercept of 0.015 counts. The low relative signals of protonated uric acid molecule at *m/z* 169 compared to intense fragment peaks

(e.g. at *m/z* 43) in the UA1 and vice versa for UA2 are due to different sample preparation methods used for two stones. The sample for UA1 was prepared by pressing the powder into indium matrix as thick film while for UA2 was prepared as thin film on Al by rasping the powder on Al foil with subsequent gentle dusting as discussed in chapter 3. Similar trend was believed to be observed for the ion peak at *m/z* 149 corresponding to (92+57) and its associated fragments at *m/z* 85, 71, and 57.

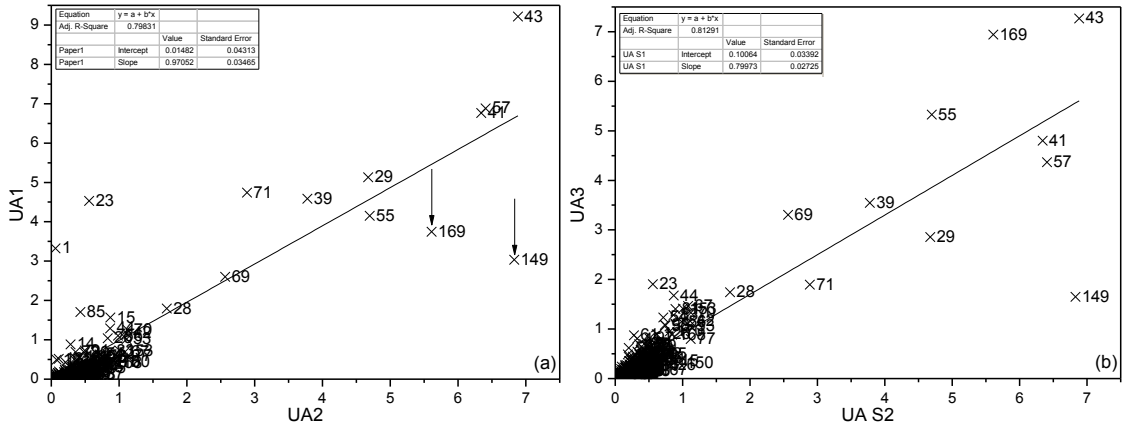

Figure 4.7. The scattered plot comparison of UA1 with UA2 (a) and UA2 with UA3 (b).

UA3 and UA2 comparison (Figure 4.7b), gives relatively high value of intercept (0.1) of linear regression line with slope of 0.79. These samples were prepared and analyzed with repeatable experimental conditions; the disagreement of 20% in the slope can be attributed to quite different amount of organic material present in two stones which is also evident from the departure of m/z 149 from the regression line. The regression line also separates the associated fragments of 149 which are mainly observed in interfering ion peaks with that of uric acid at m/z 85, 71, 57, 41, and 29. If we eliminate these 6 peaks from the two spectra, similar measurements gives slope of 0.96 within 4% agreement along with 5 times smaller intercept of 0.02 and correlation factor r^2=0.95 as shown in Figure 4.8.

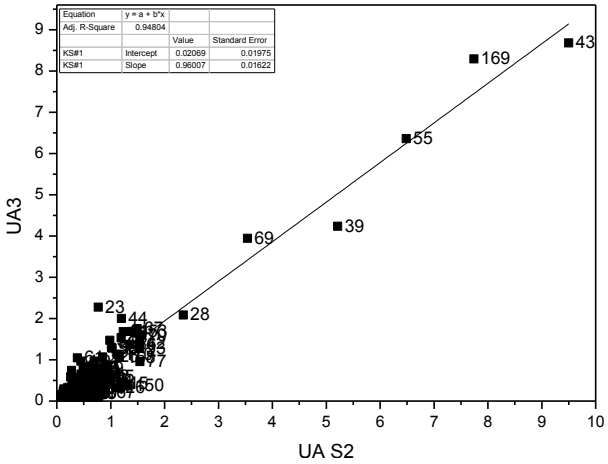

Figure 4.8. The resulting intensity scattered plot after elimination of interfering peaks of glycerol with uric acid in UA2 and UA3.

These results suggest that the ion peak often observed (very intense for few samples) in uric acid stones 'at *m/z* 149' is not a fragment of uric acid but has different origin which we assigned to glycerol. The mass spectra from the reference glycerol sample are shown in **appendix *A***. The main characteristic peaks of reference

glycerol are clearly identified in constructive SIMS spectrum where peak at *m/z* 149 is assigned to $[2Gly+H-2H_2O]^+$ or $[Gly+57]^+$. The mass peaks at *m/z* 57 corresponds to glycerol fragment $C_3H_5O^+$, we also observed the alkalized ions (cf. 2.1.3.8) due to presence of sodium in the reference glycerol but these ions were not observed for the urinary stone samples. Thus, the detection of glycerol containing ions in the stone samples might be due to presence of lipids such as triglyceride contents in stones. As, stone formers excrete more lipids in urine [94], the level of excretion varies from patient to patient, e.g. *Peng et al.* reported urinary triglycerides (TGs) ranging from 10 to 1955 mg/dl in 13 individuals with a history of chyluria [95]. Moreover, the presence of glycerol might be due to medication (remedy) in which glycerin is used to expel the stone naturally. In the present SIMS qualitative results the intensity ratio $[gly+57]^+/[UA+H]^+$ varies for three stones according to UA2>UA1>UA3 relation that reflects the relative glycerol contents incorporated in stones of three individuals. The white contents (Figure 4.6a) in UA2 are believed to be due to glycerol which is not so evident in case of UA3. Beside these stones (UA1-UA3) discussed here we also identified glycerol in other stones (UA4-UA6) identifies as uric acid.

4.1.3 TOF-SIMS analysis of sodium and potassium Urate stones

Four urate containing stones (obtained from a patient in a single episode) were analyzed with TOF-SIMS. The stones were in the form of hard spherical balls each with dimensions ca. 4 mm × 4 mm. Two of them are shown in Figure 4.9. In these stones we found 4-deoxypyridoxine 5-phosphate which is a metabolite of vitamin B6. We suggest [27] that its presence is due to the consumption of foods with high vitamin B6 content, or due to the use of vitamin B6 as a medication to prevent the growth of calcium oxalate kidney stones [82]. We also determined that the major component of this stone was sodium dihydrogen phosphate. The sample was analyzed for positive and negative ions spectra as shown in Figure 4.10, we propose that this complex stone is composed of three components: (i) uric acid and urates (ii) metabolite of vitamin B6, and (iii) sodium dihydrogen phosphate, NaH_2PO_4 [27].

Figure 4.9. The urate stones (urate1) in the shape of spherical balls.

In the negative ion spectrum shown in Figure 4.10(a), the presence of uric acid is supported by the presence of deprotonated uric acid at *m/z* 167, the molecular ion formed with the loss of two hydrogen $[M–2H]^-$ at *m/z* 166, and characteristic fragments at *m/z* 151 $[M–H-CN]^-$,

124 [M–H–HCNO]$^-$, 123 [M–2H–HCNO]$^-$, 66 ($C_3H_2N_2^-$), 42 (CNO^-), and 26 (CN^-) [27]. The difference between the spectrum observed for this sample and that of pure uric acid [26] samples discussed above is a very weak protonated uric acid molecule at *m/z* 169. The weak signal intensities of the protonated molecule, sodiated and potassiated uric acid at *m/z* 191 and 207, respectively, as compared to higher sodium/potassium adduct ion peaks at *m/z* 213 [UA+2Na–H]$^+$ and 235 [UA+3Na–2H]$^+$, 245 [UA+2K-H]$^+$ (Figure 4.10(b)) is due to the stone contents of urate salts rather than uric acid [96]. The presence of 4-deoxypyridoxine 5-phosphate, a metabolite of vitamin B6, is proposed from the ions at *m/z* 232 in negative ion mode and *m/z* 234 in positive ion mode which we assign to deprotonated $C_8H_{11}NO_5P^-$ and protonated 4-deoxypyridoxine 5-phosphate $C_8H_{13}NO_5P^+$, respectively. The other main fragment ions of this metabolite are observed at *m/z* 150 ($C_8H_8NO_2^-$), 134 ($C_8H_8NO^-$), 118 ($C_8H_8N^-$), 97 ($H_2PO_4^-$), 96 (HPO_4^-), 81 ($H_2PO_3^-$), 79 (PO_3^-), 65 ($H_2PO_2^-$), 64 (HPO_2^-), and 63 (PO_2^-) in negative ion mode. The third component of this sample is sodium dihydrogen phosphate, as is evident from the $NaH_2PO_4^+$ ion at *m/z* 120, with other associated ions observed at *m/z* 104 ($NaH_2PO_3^+$), 88 ($NaH_2PO_2^+$), and 72 (NaH_2PO^+). Elemental sodium at *m/z* 23 (Na^+) and potassium at *m/z* 39 (K^+) were observed in an intensity ratio of 2:1. It might be interesting to compare this value with the intensity ratio of 4.5:1 obtained for the urine sample (5.5 pH) from a healthy individual; the sample was prepared by wetting the scratched Al foil with drop of urine.

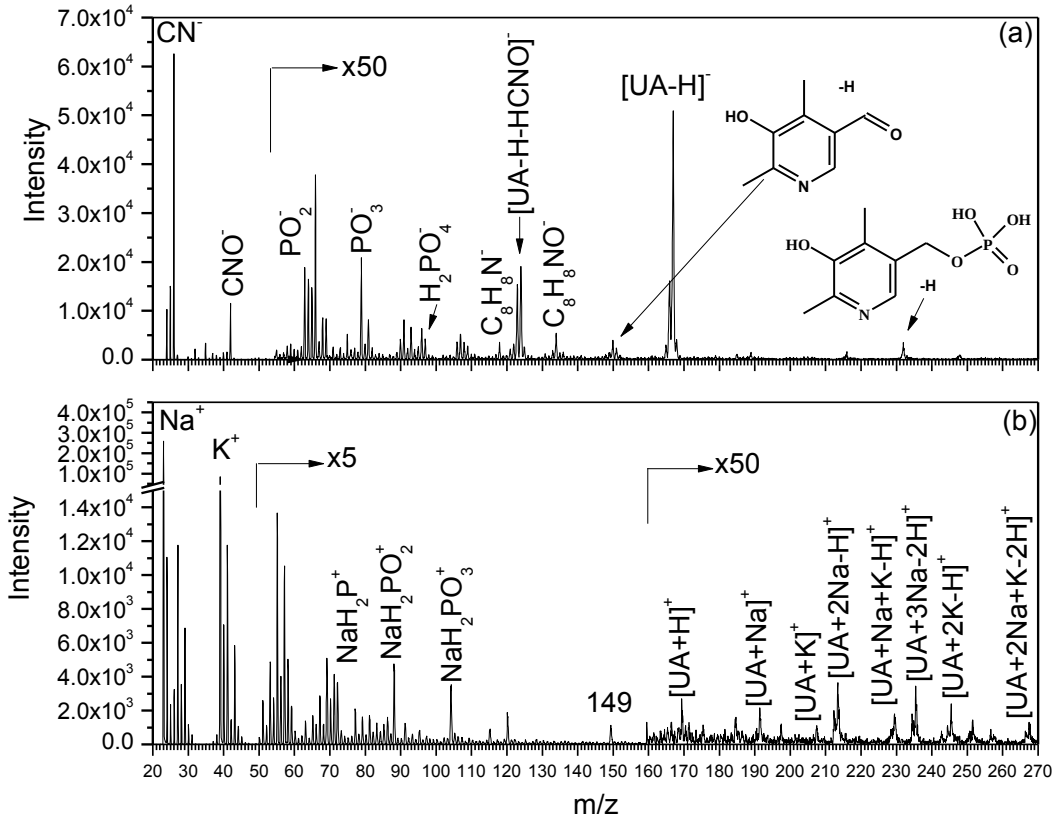

Figure 4.10. Negative (a) and positive (b) TOF-SIMS spectra of urate stone.

Incorporation of a vitamin B6 metabolite, identification of sodium and potassium urate from uric acid demonstrates that TOF-SIMS in static mode is a reliable technique for the multi-component urinary stones analysis.

4.2 Cystine stones

Cystine stones are mostly produced in patients of cystinuria, an autosomal recessive genetic disorder, and account for up to 2% of all renal stones and up to 10 % of childhood stone disease [97]. Patients affected by this inherited disease suffer from recurrent stone formation, leading to repeated surgical/endoscopic interventions, consecutive renal impairment, and, consequently, a significant impairment of life quality. The responsible genes causing cystinuria were first described in 1994 [98, 99].

This genetic disorder results in an impairment of reabsorption of the dibasic amino acids cystine ($C_6H_{12}N_2O_4S_2$, mol. wt. 240), ornithine ($C_5H_{12}N_2O_2$, mol. wt. 132), lysine ($C_6H_{14}N_2O_2$, mol. wt. 146), and arginine ($C_6H_{14}N_4O_2$, mol. wt. 174) in the kidney and the small intestine. Usually about 98–99% of the filtered load of those amino acids is reabsorbed in the proximal tubule [100]. The defect of the transporter causes a dramatic increase in urinary concentration of these substances while serum concentration is reported to just drop by 20–30% [101]. Although all of these amino acids reach high concentrations within the urine, only cystine is insoluble enough to form stones. Cystine is poorly soluble at physiological urine pH values between 5 and 7, and stones are formed especially at concentrations exceeding 240–300 mg/L (1.33–1.66 mmol/L). Higher pH values >8 lead to a threefold increase of cystine solubility [102]. Other known and yet unknown factors seem to play a role since the effect of pH on cystine solubility varies among patients [103-105]. Factors known to influence cystine excretion are dietary salt and animal protein intake. Both increase cystine excretion, yet no prospective studies have demonstrated changes in stone activity as a result of sodium restricted diets [103]. As for protein intake, just one study demonstrated that lowering intake of cystine's dietary precursor methionine reduces urinary cystine excretion [106]. Stones of cystine have a typical yellow color and a wax-like surface. The consistency is very solid [89].

4.2.1 TOF-SIMS analysis of cystine stones

In this study two stones were identified as cystine; one from the human [28] and other was from dog. As received human kidney stone was hard and very large with two-dimensional size of ca. 20 mm × 10 mm. It was of yellowish color with a rough and sharp surface as shown in

Figure 4.11a. The stones from the dog were of completely different visual morphology in terms of size, shape color and were smoother as shown in Figure 4.11b.

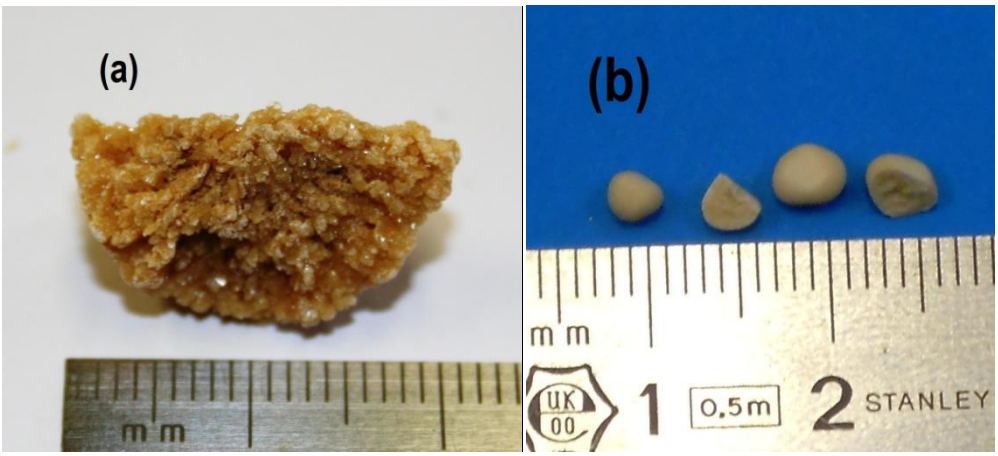

Figure 4.11. Morphological appearances of human stone (a) and dog stone (b).

The samples prepared from human kidney stone powder and two reference chemicals (cysteine and cystine) were analyzed in both positive and negative TOF-SIMS modes. The molecular structure of cysteine (cySH) is shown in Figure 4.12a. It is a non-essential amino acid, which means that cysteine is biosynthesized in the human body under normal physiological conditions. The positive ion spectrum of cysteine was magnified along the intensity axis, and is shown in Figure 4.12a. The main characteristic ions of cysteine at *m/z* 18, 76, and 122 correspond to the protonated ammonia NH_4^+, the fragment ion $[cySH\text{-}CO_2H]^+$, and its protonated molecule $[cySH+H]^+$, respectively. The assignments of these ion peaks to respective fragments were made on the basis of collision-induced dissociation and MALDI TOF/TOF MS studies on amino acids [107-109].

The cystine (cySScy) is a dimeric amino acid formed by the oxidation of two cysteine residues that covalently links to make a disulfide bond; its molecular structure is shown in Figure 4.12b. Cystine is water-insoluble, while its monomer (cysteine) is soluble in water. The positive ions spectrum of cystine is shown in Figure 4.12b with the characteristic ions at *m/z* 18, 74, 120, 122, 152, and 241, corresponding to NH_4^+, the most abundant peak of cystine fragment $[cyS\text{-}CO_2H_2]^+$, cysteine sulfenium $[cyS]^+$, protonated cysteine $[cySH+H]^+$, fragment containing disulfide bond $(cySS)^+$, and protonated cystine $[cySScy+H]^+$, respectively. The cysteine sulfenium (*m/z* 120) was mostly absent in the case of reference cysteine (Figure 4.12a); here it is considered necessary to reveal that protonated cysteine (*m/z* 122) is a fragment originating from protonated cystine molecule not from the monomer cysteine. The main fragment schemes and structures of these assigned peaks can be found in the study of disulfide amino acids with electrospray ionization and triple-quadrupole tandem mass spectrometry [110], although the relative peak

intensities of these fragments are quite dissimilar due to different ionization method used in our study.

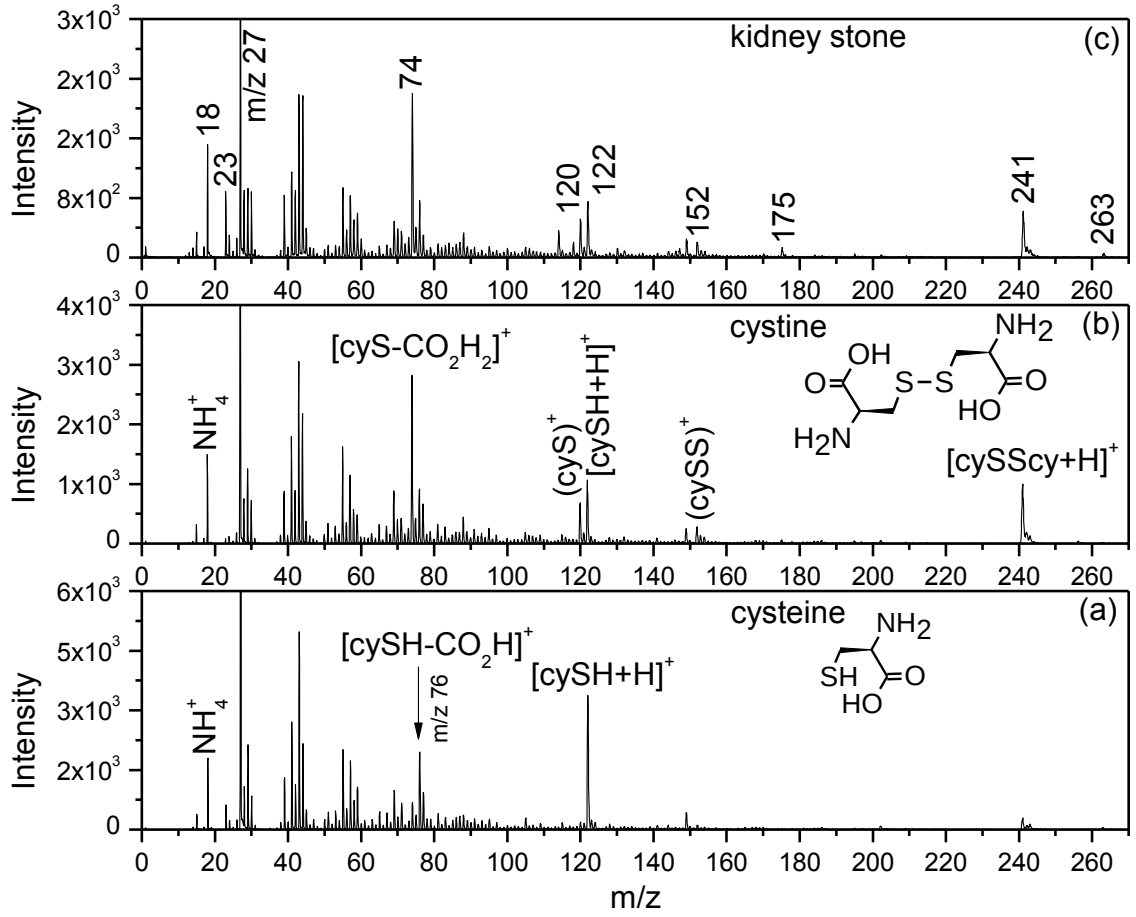

Figure 4.12. The positive TOF-SIMS mass spectra of reference cysteine (a), cystine (b) and human kidney stone (c).

The positive TOF-SIMS spectrum of the kidney stone looks very similar to the characteristic spectrum of the reference cystine (Figure 4.12b and 4.12c). The peaks at *m/z* 18, 74, 120, 122, 152 and 241 are the same as in the case of cystine (Figure 4.12b) corresponding to a distinct protonated molecule and the main fragments discussed above. In addition to the main characteristic ion peaks of cystine, the ion peak at m/z 175 corresponding to protonated arginine molecules $[Arg+H]^+$ is also evident, this assignment in accordance with our further study on reference arginine sample (cf. 2.2.3). We also observed sodiated cystine molecules $[cySScy+Na]^+$ at *m/z* 263, its fragment ion at peak (partial intensity) *m/z* 175 $[cySS+Na]^+$, and elemental sodium ion peak at *m/z* 23 are also evident from the spectrum. This could be due to the presence of a small amount of cystine salt produced by alkalization of the urine by sodium bicarbonate dosage. This method is generally used to dissolve the cystine stones by increasing the urine pH; cystine is soluble in urine at elevated pH, above 7.5 pH is recommended for treatment to improve cystine

solubility [111, 112] which is evident in the cystine solubility curve as function of urine pH (Figure 4.13).

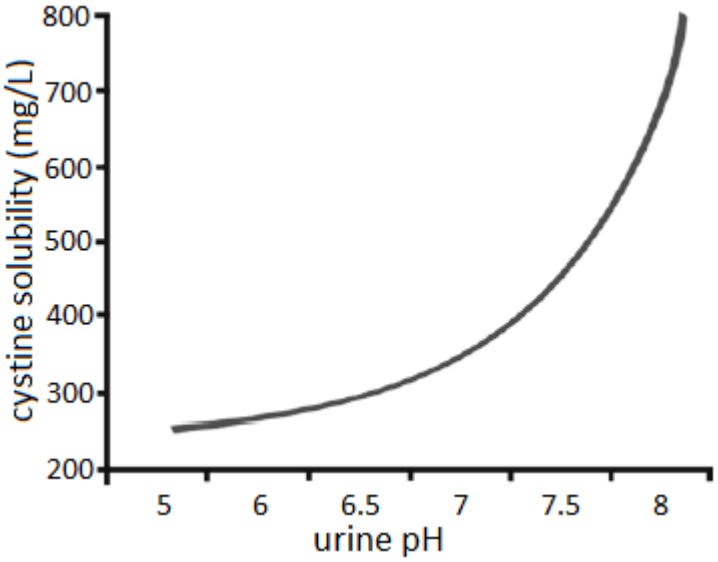

Figure 4.13. Solubility of cystine at different urinary pH values [112].

The negative TOF-SIMS spectra of reference cysteine, cystine, and the kidney stone are shown in Figure 4.14. The distinct series of ion peaks are observed for each sample. The peaks at *m/z* 32, 48, 64, 80, and 120 are detected in case of reference cysteine sample; these peaks correspond to S^-, SO^-, SO_2^-, SO_3^-, and the deprotonated cysteine $[cySH\text{-}H]^-$. The negligible dimmer peak at *m/z* 239, corresponding to $[cySScy\text{-}H]^-$, is also observed. In addition to cysteine characteristic peaks, trace amount of glycerol was also identified via the discrete series of foremost characteristic peaks observed at *m/z* 93 $[M+H]^-$, 185 $[2M+H]^-$, and 277 $[3M+H]^-$ [113].

For cystine, we observed all the peaks mentioned above for cysteine along with the peaks due to its dimmer nature at *m/z* 239, and 152, corresponding to deprotonated cystine $[cySScy\text{-}H]^-$, and a fragment containing dimmer of sulfur at *m/z* 152 $(cySS)^-$. This peak was also observed in positive mode, possibly by making a double bond between two sulfur atoms after fission of S-C bond, the complementary ion peak is obvious at *m/z* 87 $[cy\text{-}H]^-$. The peaks with masses corresponding to the negative ion peak of cysteine sulfenium (*m/z* 120) and the fragment at *m/z* 74 $[cyS\text{-}CO_2H_2]^-$ are also observed in the positive ion spectrum of cystine. The other distinctive features are the different relative abundance of ion peak at *m/z* 64, in the case of cystine this peak has also S_2^- contribution, and the relative abundance of SH^- (*m/z* 33) and S^- (*m/z* 32). The higher abundance of the peak at *m/z* 33 is due to S-H bond present in the molecular structure of cysteine (Figure 4.12a).

The negative ion spectrum of the kidney stone has all characteristic peaks along with their relative abundance are indeed similar to that observed for reference cystine at *m/z* 32, 33, 48, 64, 74, 87, 120, 152, and 239, corresponding to S^-, SH^-, SO^-, (SO_2^-, S_2^-), $[cyS\text{-}CO_2H_2]^-$, $[cy\text{-}H]^-$, 120 $(cyS)^-$, $(cySS)^-$, and $[cySScy\text{-}H]^-$, respectively. From the resemblances of kidney stone spectra in both modes, with that of cystine, we can reveal that the cystinuria stone is composed of cystine

that is insoluble in acidic urine below pH 6.5; on the other hand, cysteine is soluble in water. These results are consistent with the stone formation studies.

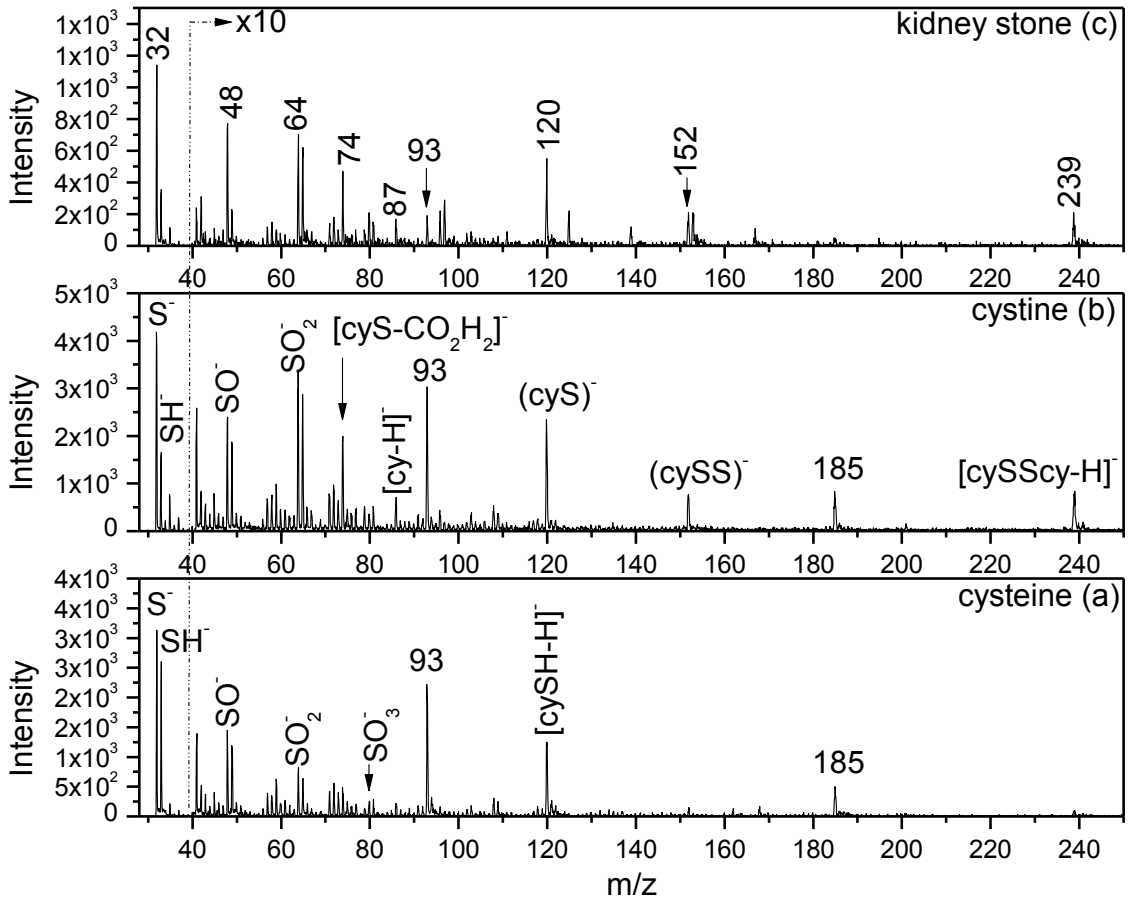

Figure 4.14. The negative TOF-SIMS mass spectra of reference cysteine (a), cystine (b) and human kidney stone (c).

In this study, we identified this renal stone as cystine by comparing the mass spectra with reference cystine and its monomer cysteine. In this stone we have not detected the ion peaks characteristic for PO_4, a stoichiometric component common in calcium phosphates and struvite stones, nor the particular elemental/polyatomic ion peaks of Ca^+, CaO^+, and $CaOH^+$, which correspond to calcium containing kidney stones (will be discussed in following chapters). The absence of uric acid is also obvious from the non existence of protonated and deprotonated molecules in positive and negative modes respectively, along with other characteristic fragments reported in our previous study [26]. The mass spectrometric signals corresponding to protonated and deprotonated molecules were obtained for cystine, which provided its directed identification. Moreover, the cystine spectra gave distinguishing intensity ratios for its principle fragments when compared with the corresponding ion peaks of cysteine, as shown in the Table 4.2. The intensity ratios for the selected peaks in the positive mode are almost the same for both cystine and the

stone sample; these values are almost a factor of ten bigger than the respective intensity ratios for cysteine.

For further confirmation, we compared these results with the dog stone TOF-SIMS spectrum in positive mode (shown in Figure 4.15), as in canines the occurrence of cystine stones is much higher (ca. 26%) than that in human. Although, the morphology is quite different as obvious in Figure 4.11, chemical compositions are very similar. The relative peak intensities for human and dog stones are also comparable as shown in Table 4.2. In the lower *m/z* range we identified the distinguishing ion peaks at *m/z* 28 ($CHNH^+$), and 44 ($C_2H_4NH_2^+$) which are minor in uric acid while in cystine high intensities of these peaks are as a result of direct fragmentation of the molecular structure, additionally the peak at *m/z* 43 ($C_2H_3NH_2^+$) can also be due to a direct fragment (unspecified ionic structure) while for uric acid at the same *m/z* identified ion is $HCNO^+$. The dog stone also contained arginine contents which are evident by the presence of protonated arginine molecules at m/z 175$[Arg+H]^+$. The ion peak at 149 corresponding to presence of glycerol in more intense in this stone compared to human stone.

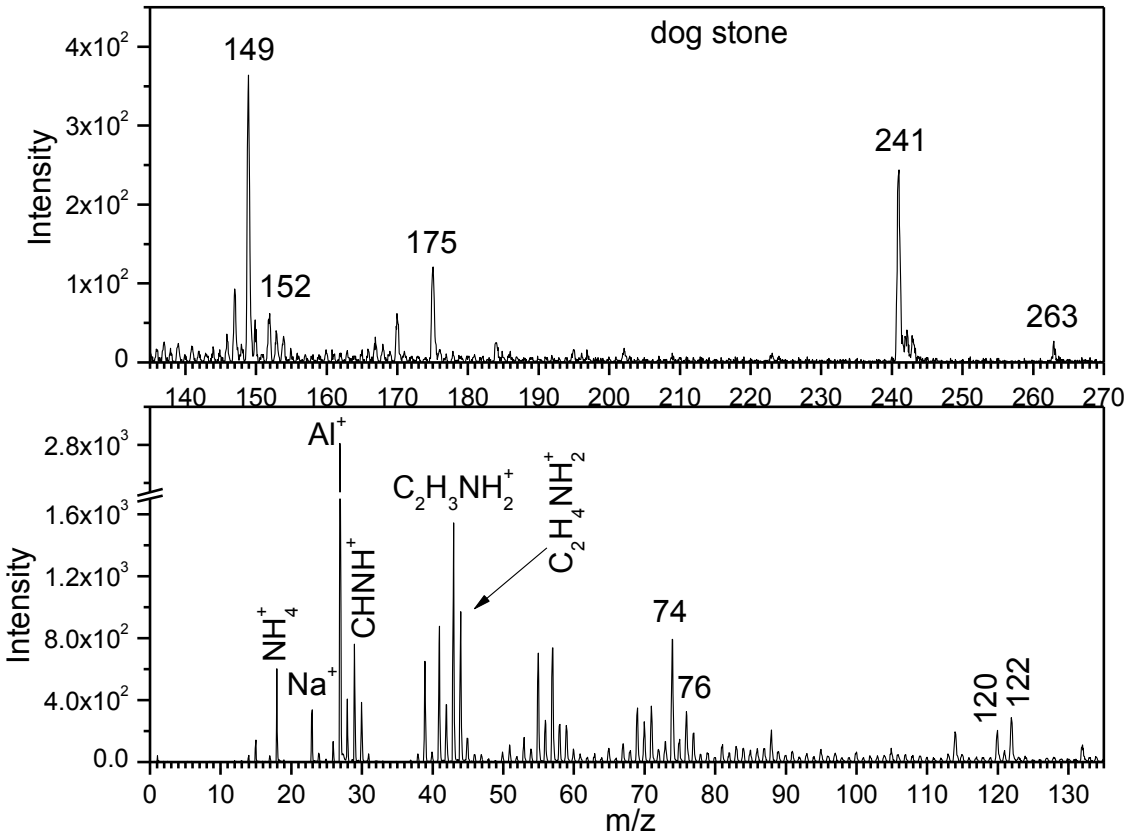

Figure 4.15. The positive TOF-SIMS mass spectrum of dog stone.

The intensity ratios in negative ion mode are about 2.5 times higher for cystine and human stone as compared to cysteine. The lower value of S^-/SH^- in cysteine is due to presence of S-H bond and the higher value of other peaks ratio in cystine is due to presence of S-S bond.

Table 4.2. The intensity ratios of the characteristic ion peaks of cysteine, cystine, human stone [28], and dog stone.

Sample	Intensity ratios			
	Positive ions		Negative ions	
	$[cyS\text{-}CO_2H_2]^+$/ $[cySH\text{-}CO_2H]^+$	$(cyS)^+/[cySH+H]^+$	S^-/SH^-	*m/z (64+65)/(48+49)
cysteine	0.33	0.06	1.00	0.62
cystine	3.10	0.69	2.38	1.55
human stone	2.96	0.69	2.57	1.59
dog stone ☼	2.50	0.65	--	--

$(S_2^-(+SO_2^-) + S_2H^-(+SO_2H^-))/(SO^-+SOH^-)$, ☼ was not reported in [28].

The Fourier transform infrared spectroscopy (FTIR) is the most commonly applied stone analysis method. However, it is inadequate to analyze cystine in compounds with a mixture of struvite, calcium oxalate and uric acid because of the overlapping of characteristic absorption bands; this technique often requires the confirmation by some other complementary methods. When chemical analysis is used as a complementary technique with FTIR for cystine containing stone identification, surprisingly very low success rate (10%) was confirmed by scanning electron microscopy with energy-dispersive X-ray spectroscopy (SEM-EDX) [114]. The confirmation with SEM-EDX resulting in an unanticipated cystine stone occurrence rate of 0.2% (3 out of 1300 stones), which is 5-10 times lower than the worldwide statistical data (1 - 2%). The low rate of cystine confirmation might be due to its sensitivity in the complex matrix.

4.3 Cholesterol stone

Cholelithiasis is also one of the most prevalent diseases affecting the gastrointestinal tract. Gallstones are a major cause of morbidity and mortality throughout the world. Progress in the understanding and treatment has been rapid during the past decades.

Gallstones are composed mainly of cholesterol, billirubin and calcium salts, with smaller amounts of proteins and other materials. In western countries, cholesterol is the principal constituent of more than three quarters of gallstones, and many of these stones are more than 80 percent cholesterol [115].

In the simpler sense, cholesterol gallstones form when the cholesterol concentration in bile exceeds the ability of bile to hold it in solution. Composition knowledge of gallstone is essential for understanding the pathogenesis of disease, which will contribute to the prevention of gallstone [116].

4.3.1 TOF-SIMS analysis of cholesterol stone

As-received gallstone was of an oval shape, extremely large in size (ca. 40 mm × 25 mm) about half the average size of gallbladder (ca. 80 mm × 40 mm) and the surface of gallstone was granular with light yellow color as shown in Figure 4.16. When cross sectioned, it was easy to cut, producing glistening and waxy crystals.

Figure 4.16. The surface and cross sectional view of gallstone identified as cholesterol.

The positive TOF-SIMS spectrum of the sample prepared from the stone materials is shown in Figure 4.17a. The characteristic molecular ions were observed at *m/z* 401, 385, and 369. We assigned these peaks to cholesterol [28] (the molecular structure of cholesterol is shown in Figure 4.17a); we assigned these peaks correspond to $[MO\text{-}H]^+$, $[M\text{-}H]^+$, and $[M\text{-}OH]^+$, respectively. Identification and assignment of the latter two peaks is based on the cholesterol and lipid studies [117-120] with secondary ion mass spectrometry. Similar results have been reported using Ga^+ projectile for cholesterol sample [117]. The ion peak at *m/z* 401 was observed due to oxidation of the prepared sample before introduction into the vacuum system. To confirm this fact, we prepared two samples: one was immediately loaded in the analysis chamber and the second was kept for ageing in a transparent plastic bottle for three days.

The mass spectra of both samples are shown in Figure 4.17; the aged sample exhibits an increased intensity of $[MO\text{-}H]^+$ at *m/z* 401, at the same time, the intensity of $[M\text{-}OH]^+$ is reduced by the same factor. We did not observe any difference in the relative intensities of fragments in the *m/z* range of 0.5-100. The most abundant peaks in each C_n-group are identified at *m/z* 27, 43, 55, 69, 81 and 95, corresponding to $C_2H_3^+$, $C_3H_7^+$, $C_4H_7^+$, $C_5H_9^+$, $C_6H_9^+$, and $C_7H_{11}^+$, respectively. The peaks at 27 and 69 have also some contributions of Al^+ matrix ions and $^{69}Ga^+$ primary ions implanted into the sample.

TOF-SIMS negative ion spectrum is shown in Figure 4.18, the main peaks are observed at *m/z* 13, 16, 17, 24, 25, 36, 37, 38, 41, 43, 45, 46, and 49; these peaks correspond to CH^-, O^-, OH^-, C_2^-, C_2H^-, C_3^-, C_3H^-, $C_3H_2^-$, $C_3H_5^-$, $C_3H_7^-$, and C_4H^-, respectively. We did not observe heavy

negative molecular ions that might be due to the strong fragmentation of molecules under the higher-impact energy (ca. 19 keV) of the primary Ga^+ ion beam. On the other hand, in the positive mode the impact energy of primary ions was only 9 keV.

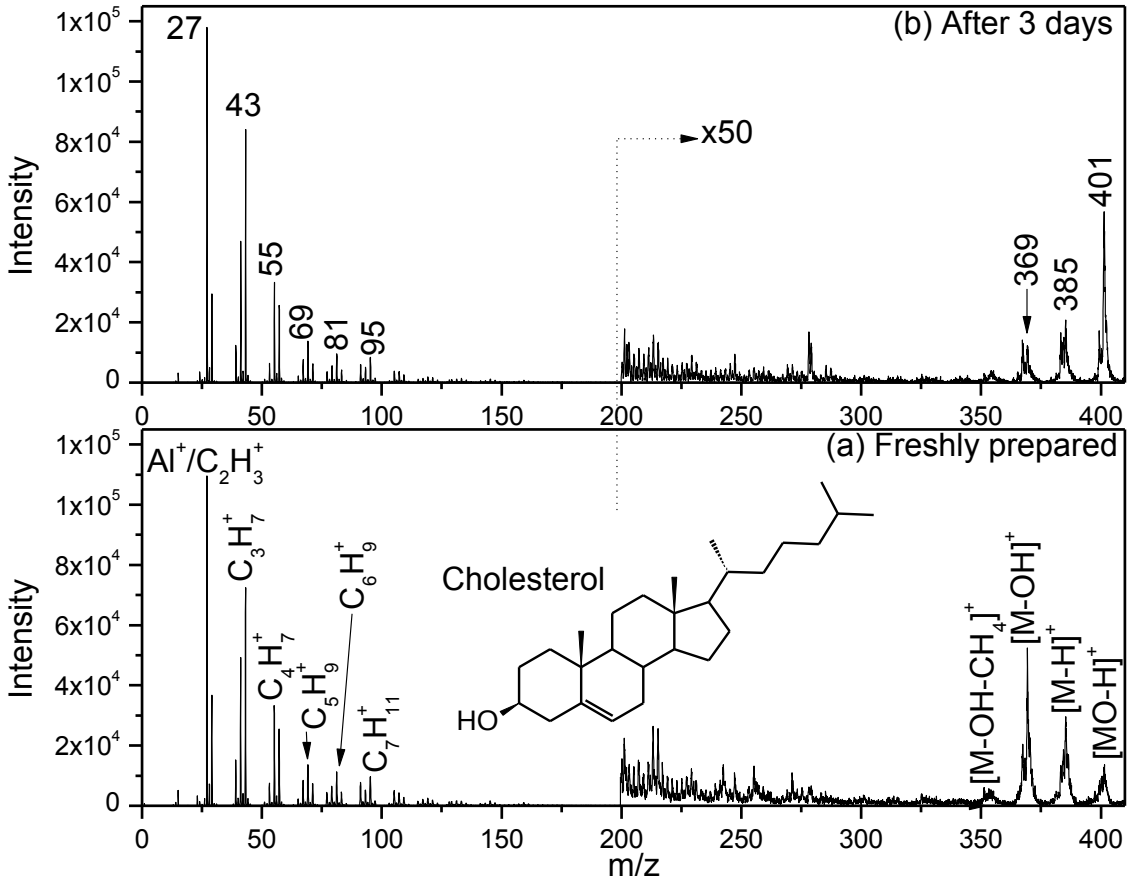

Figure 4.17. The positive TOF-SIMS mass spectra of gallstone: (a) freshly prepared sample and (b) after 3 days of ageing in ambient conditions [28].

The SIMS spectrum shown in Figure 4.18b is from sample of same stone acquired after Ga+ beam pre-sputtering (ca. 5×10^{13} ions/cm2). We observed the carbon cluster formation because of preferential sputtering of H from the sample matrix. The main carbon cluster were observed at *m/z* 24 (C_2^-), 36 (C_3^-), 48(C_4^-), and 72(C_6^-). The hydrogenated, oxide and hydroxyl carbon cluster were also identified. Interestingly, these clusters were not observed with nitrogen which confirms the absence of any nitrogen containing compound.

Chemical composition of gallstones is essential for dissolution therapy, however after the introduction of laparoscopic cholecystectomy for gallstone treatment, it is less important as to whether or not the main component of gallstone is cholesterol as it can be performed regardless of its composition. Moreover, gallstone composition information is still essential for understanding the pathogenesis and prevention of gallstones [116].

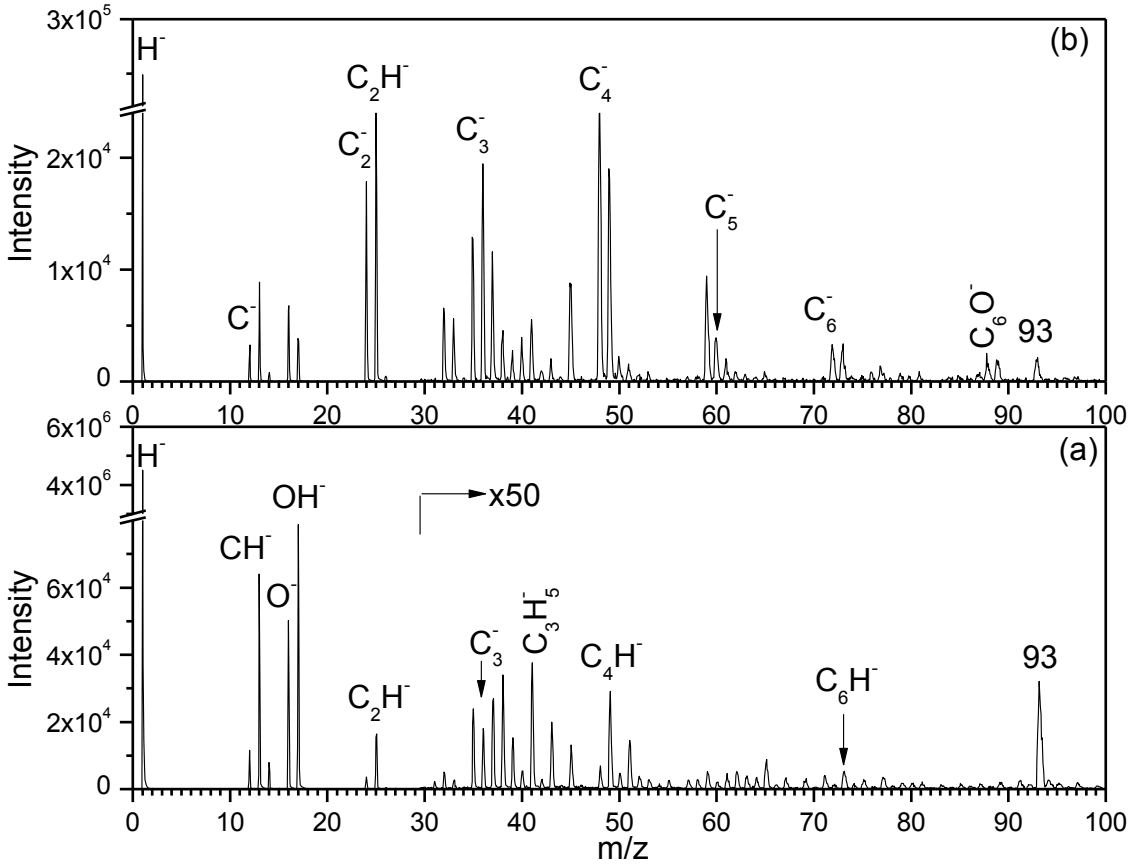

Figure 4.18. The negative TOF-SIMS mass spectrum of the freshly prepared gallstone sample on Al (a) and indium substrate (b).

The gallstones which contain more than 80% cholesterol are classified as pure cholesterol gallstones [116]. The cholesterol stones are also formed as a mixture with calcium carbonate ($CaCO_3$) and bilirubin ($C_{33}H_{36}N_4O_6$). In our study [28], we identified gallstone as pure cholesterol with quasi-molecular ion peaks of $[M\text{-}H]^+$ (*m/z* 385) and $[M\text{-}OH]^+$ (*m/z* 369). These characteristic ion peaks in the present study are in accordance with cholesterol containing specimens [120] and pure cholesterol test samples studied with a number of primary ion sources to check the efficiency of the state of art SIMS [43]. Cholesterol in the mixed composition stones should have at least calcium ions at *m/z* 40 corresponding to calcium carbonate and nitrogen containing cyanide ions CN^-, and CNO^- at *m/z* 26 and 42, corresponding to bilirubin, which are completely absent in both SIMS modes. These ions are readily observed with high sensitivity and are already reported in pure as well as mixed human stone samples [26, 27]. We also observed the ions corresponding to cholesterol oxide at *m/z* 401 $[MO\text{-}H]^+$ in the aged sample [28], which has not been reported so far. This fact demonstrates how quickly and readily one can identify the change in surface chemistry from SIMS data when compared to other stone analysis techniques.

5. TOF-SIMS analysis of calcium oxalate urinary stones

In this chapter we will discuss the compositional analysis of calcium oxalate stones; whewellite and weddellite. The results of stone sample in which the presence of calcium formate was identified in Ghumman et al. [27] will also be presented; calcium formate is a rare phase of naturally occurring calcium oxalates. Moreover, the binary stones of calcium oxalate and uric acid developed as core and shell respectively in stone of an individual and vice versa in another individual's stone will be presented. Finally we will summarize the results of nine stones (S1-S9) in which we identified calcium oxalate as major component while calcium phosphates as minor component.

5.1 Calcium oxalate stones

A majority of urinary stones are calcium stones with calcium oxalate (COX) and calcium phosphate (CaP) accounting for approximately 80% of total human urinary stones. The calcium oxalate stones are developed due to its super saturation in urine. The urine calcium oxalate super-saturation cause crystal nucleation, aggregation of these crystals result in the formation of stones in the renal system.

The calcium oxalates crystallize into three hydrates- calcium oxalate monohydrate ($CaC_2O_4.H_2O$), calcium oxalate dihydrate ($CaC_2O_4.(2+x)\ H_2O$) [121] where $x \leq 0.5$, and calcium oxalate trihydrate ($CaC_2O_4.3H_2O$) (*Deganello et al.* 1981), a less common form in pathological stone formation. The higher level of super-saturation leads to more compact, hard, and possibly monohydrate stones while at lower saturation dihydrate phase is expected [121].

The most frequent components are the calcium oxalate monohydrate and dihydrate known as whewellite and weddellite respectively in mineralogy. The occurrence frequency of whewellite is 78% and that of weddellite is 43%. A calcium oxalate trihydrate was described in

the literature [122], but the occurrence was not confirmed by other authors. Also the occurrence of a second form of calcium oxalate monohydrate has been observed [123]. The presence of another form of calcium oxalate as calcium formate ($CaH_2C_2O_4$) in urinary stone was also reported in our study [27].

Whewellite stones usually have a dark brown or black color; the lighter the color, the higher the content of organic material. The surface is often granular and stones are very hard.

Weddellite stones mostly have a loose structure with a gray-yellow color. Especially noteworthy are crystals of tetragonal-dipyramidal morphology. The crystals are sharp and in various orientations with the edges on the outer surface. The compact whewellite as core and the weddellite crystals on the surface of mixed stones of whewellite-weddellite are more often [124].

The calcium oxalate stones show a large variety of morphological and structural forms of appearance due to the existence of the two hydrates levels (whewellite and weddellite) and the transformation phenomenon of weddellite into whewellite [125, 126].

In this study, we analyzed 9 urinary stones (Table 5.1) having verity of morphological structure and colors in which calcium oxalate was identified as major component; here we will discuss some important results showing the potential of TOF-SIMS to recognize these stone components in pure (at least 95% calcium oxalate) and admixed stones. In this study we identified calcium oxalate as highly non-conductive when prepared as thick layer or pellet. So most of the samples were prepared on aluminum foil by rasping the powder produced from the urinary stones (cf. 3.6). The samples prepared by this method can be analyzed without charge neutralization which is generally achieved by flooding the low energy electrons for non-conductive specimens. For the samples prepared on indium such charge neutralization was achieved by electron flood gun.

Table 5.1. Experimental conditions and classification of stones identified as calcium oxalate

stone sample	presputtering with 5-15 $\times 10^{13}$ ions/cm^2	substrate used	Classification with TOF-SIMS
S1	Yes	Al	calcium oxalate
S2	Yes	Al	calcium oxalate
S3	*	Indium	calcium oxalate
S4	*	Indium	calcium oxalate
S5	Yes	Al	calcium oxalate (core)
S6	Yes	Al	calcium oxalate (shell)
S7	Yes	Al	calcium oxalate
S8	Yes	Al	calcium oxalate
S9	Yes	Al	calcium oxalate

**The positive ion mass spectra shown in Figure 5.4 were acquired without pre-sputtering while the data presented in Table 5.2 for the respective stone samples correspond to mass spectra acquired after presputtering used for other samples.*

5.1.1 TOF-SIMS analysis of whewellite and weddellite

Three kidney stones were received from two patients. Stone shown in Figure 5.1a was obtained from one patient and two stones shown in Figure 5.1b were obtained from other patient in a single episode. According to the literature information on morphology the predicted whewellite stone (with dark color, Figure 5.1a) was very hard and compact as compared to expected weddellite stones (Figure 5.1b). When analyzed with TOF-SIMS the composition was quite similar except the amount of glycerol and water contents.

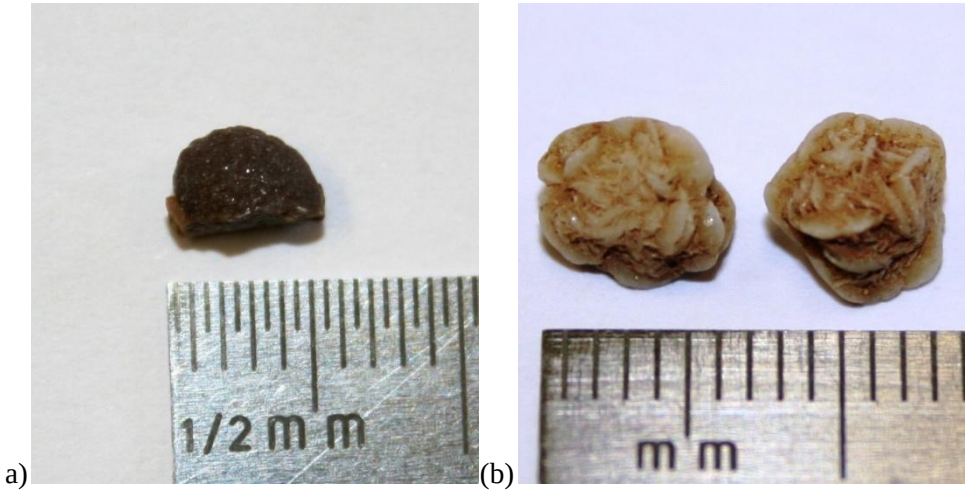

Figure 5.1: Typical morphology of (a) whewellite (S2) (calcium oxalate monohydrate) and (b) weddellite (calcium oxalate dihydrate) stones (S1).

The representative positive ion mass spectrum from the weddellite (calcium oxalate dihydrate) stone (S1) is shown in Figure 5.2 in the mass range of 0-185. The characteristic ions of calcium oxalate were observed at *m/z* 20, 40, 41, 44, 48, 56, 57, 80, 85, 96, 112, and 113 corresponding to Ca^{+2}, $^{40}Ca+$, CaH^+, $^{44}Ca^+$, C_4^+, CaO^+, $CaOH^+$, CaC_2H^+, $CaC_2H_2^+(+CaCN^+)$, Ca_2^+, $CaHCO_2^+$, Ca_2O^+, Ca2O2+, and $Ca_2O_2H^+$ respectively. Trace amount of uric acid is also evident from the uric acid protonated molecule at *m/z* 169 $[UA+H]^+$, and adduct ions at *m/z* 66, and 82 corresponding to $CaCN^+$, $CaCNO^+$. The ion peak of Al^+ at *m/z* 27 is from the aluminum substrate used. We also observed trace amount of sodium (Na^+) at *m/z* 23, potassium (K^+) at *m/z* 39, and calcium phosphate. The presence of calcium phosphate is evident from the ion peaks at *m/z* 31, 47, and 103 corresponding to P^+, PO^+, and $CaPO_2^+$. The core of the stone was relatively enriched of uric acid and calcium phosphate.

The positive ion mass spectrum of whewellite (calcium oxalate monohydrate) stone (S2) is shown in Figure 5.3. The all characteristic ions of calcium oxalate discussed above were observed. The difference which we identified between two stones is the presence of higher content of glycerol ($C_3H_8O_3$) in calcium oxalate monohydrate. The source of glycerol (i.e. lipids)

is already discussed in previous chapter. Identification of glycerol was made through its calcium adduct ion peaks observed at *m/z* 133 [Ca+Gly+H], 225 $[Ca+2Gly+H]^+$ and 317 $[Ca+3Gly+H]^+$.

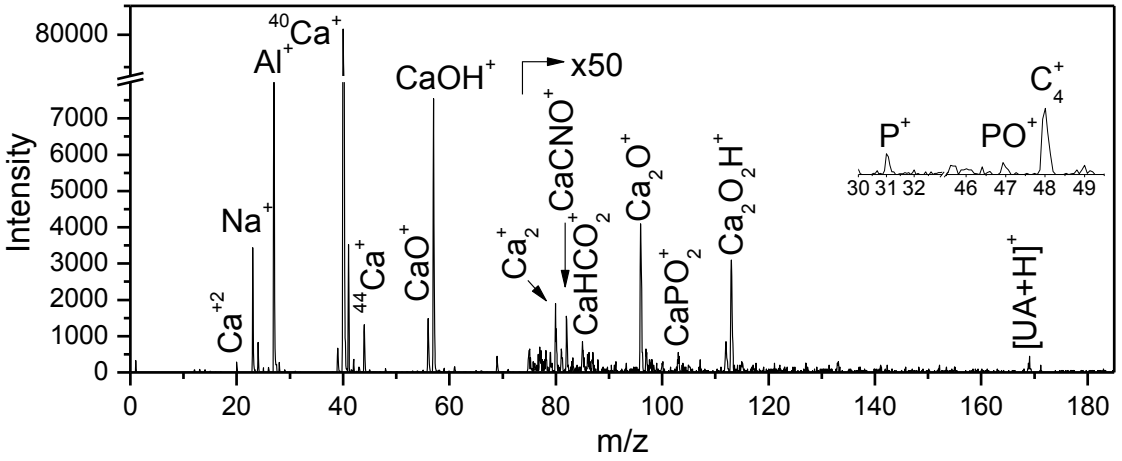

Figure 5.2: Positive ions mass spectrum of weddellite (S1) shown in Figure 5.1b.

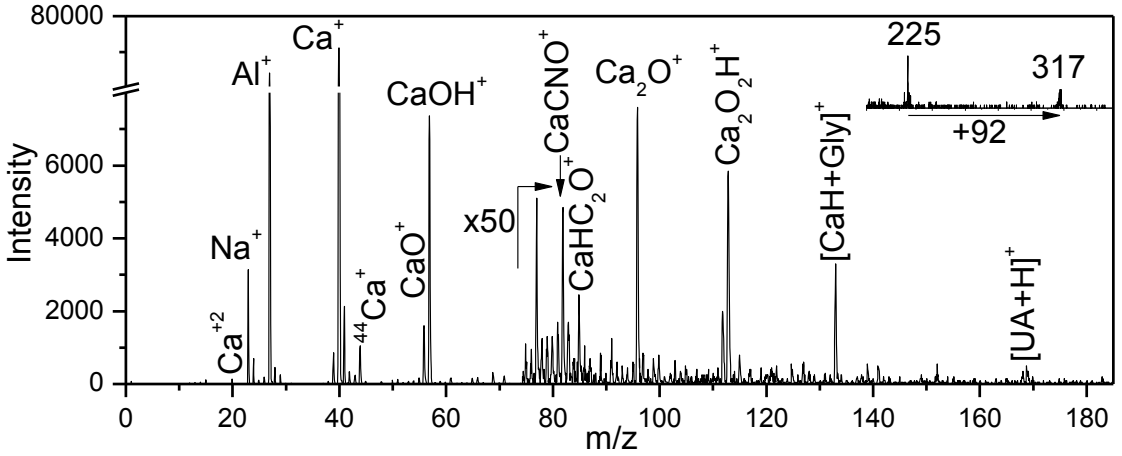

Figure 5.3: Positive ion mass spectrum of whewellite (calcium oxalate monohydrate) stone (S2).

As we discussed above, different phases of calcium oxalates mineralization incorporate different amounts of water. We did not observe water ion peak H_3O^+ (*m/z* 19) neither in the spectra shown in Figure 5.2 and Figure 5.3 nor in the spectra acquired without pre-sputtering (not shown). The only characteristic peaks representing water are $CaOH^+$, and $Ca_2O_2H^+$. The first is the most intense and hence could be used for phase identification along with principal elemental calcium (Ca^+) ion peak. The relative intensity of $CaOH^+$ strongly depends on the primary ion dose; higher primary ion dose give higher fragmentation resulting low relative intensity of $CaOH^+$. One should keep in mind that these experiments were conducted in same conditions. We sputtered both samples with primary ion dose of $5x10^{13}$ ions/cm^2 (which is ca. 5 times higher than the static limits) before the spectral acquisition to eliminate hydrocarbon contaminants especially the $C_4H_9^+$ interfering at *m/z* 57 corresponding to $CaOH^+$. The $CaOH^+$ signals of 8.55% for S1 and 13.78% for S2 of principal ion peak of calcium (Ca^+) were observed. We proposed the difference

in relative abundance of $CaOH^+$ in two samples is due to two phases of calcium oxalate, i.e. $CaC_2O_4.H_2O$ and $CaC_2O_4.2H_2O$. Each water molecule in the formula gives one OH group resulting 1:1 ratio in monohydrate and 1:2 ratio in dihydrate corresponding to Ca:OH in the molecular formula. Statistically 1:1 ratio for monohydrate gives maximum yield probability (0.50) for $CaOH^+$ when compared to probability of 0.43 corresponding to 1:2 ratios for dihydrate. According to statistical predictions, the higher relative abundance in S2 could be due to monohydrate phase and comparative lower value in S1 corresponds to dihydrate phase of calcium oxalate.

Another factor which might play role in higher ion yield of $CaOH^+$ in calcium oxalate monohydrate is the 25% of hydrogen of water do not make further bonding in the crystal structure. This gives an easier pathway for $CaOH^+$ emission when compared with dihydrate crystal where 100% water hydrogen makes further bonding in the crystal structure proposed in literature [121].

In our extensive experimental study to correlate $CaOH^+$ with experimental parameters, we observed increase in the $CaOH^+/Ca^+$ ratio from the surface prepared with bigger grain size of the powder particles as compared to very fine powder; we relate this fact to low amount of water loss in larger gain particles under UHV conditions, because they offer low surface area. In dynamic ion beam sputtering we observed increase in the $CaOH^+$ followed by decrease under prolonged sputtering. The gain is due to cleaning effect and formation of great amount of OH^- ions that bond with calcium and hence gain was observed followed by loss of water. In conclusion, phase identification is not straightforward, although it is possible through controlled experimental parameters.

The comparison between chemical compositions of two phases of calcium oxalate reveals marked similarities except the trace amount of other components identified in these samples. Results are in agreement with the associated chemical compositions of these stones with other techniques. The morphology of these stones correlates with the monohydrate [8] and dihydrate of calcium oxalate stones reported in literature [127]. TOF-SIMS being very sensitive gives structural information of trace contents of organic compounds which could be the nucleation substrates/promoter for these crystals. These results give us additional information about the water attachment with calcium in the crystal. The bonding of water with calcium is believed to be due to partial positive charge on calcium atoms, resulting in high intensity of $CaOH^+$ ion peak at *m/z* 57 which is the 2nd largest peak in the mass spectrum.

It might be interesting to mention here that some of the characterization techniques commonly used is not suitable to give the structural information about the H_2O molecule

associated attachment. Other techniques give only the water contents present which is normally complicated in admixed stones and do not give any information of admixed component.

5.1.2 Identification of calcium formate in calcium oxalate stone

In our study [27], we analyzed a human kidney stone (S3) containing calcium formate, $Ca(HCO_2)_2$, which is used in the food industry as a food additive, denoted by E238. To the best of our knowledge this calcium formate phase has not been previously reported as being present in a kidney calculus. We clearly identified $Ca(HCO_2)_2$ by the detection of protonated calcium formate molecules in the positive secondary ion spectra.

The sample S3 was analyzed for positive and negative mass spectra in the *m/z* range of 0-500; the results were compared with those of known calcium oxalate stone S4. The positive ion mass spectra of two urinary stones (S3 and S4) are shown in Figures. 5.4a and 5.4b, respectively and the negative ion mass spectra of respective stones are shown in Figure 5.5.

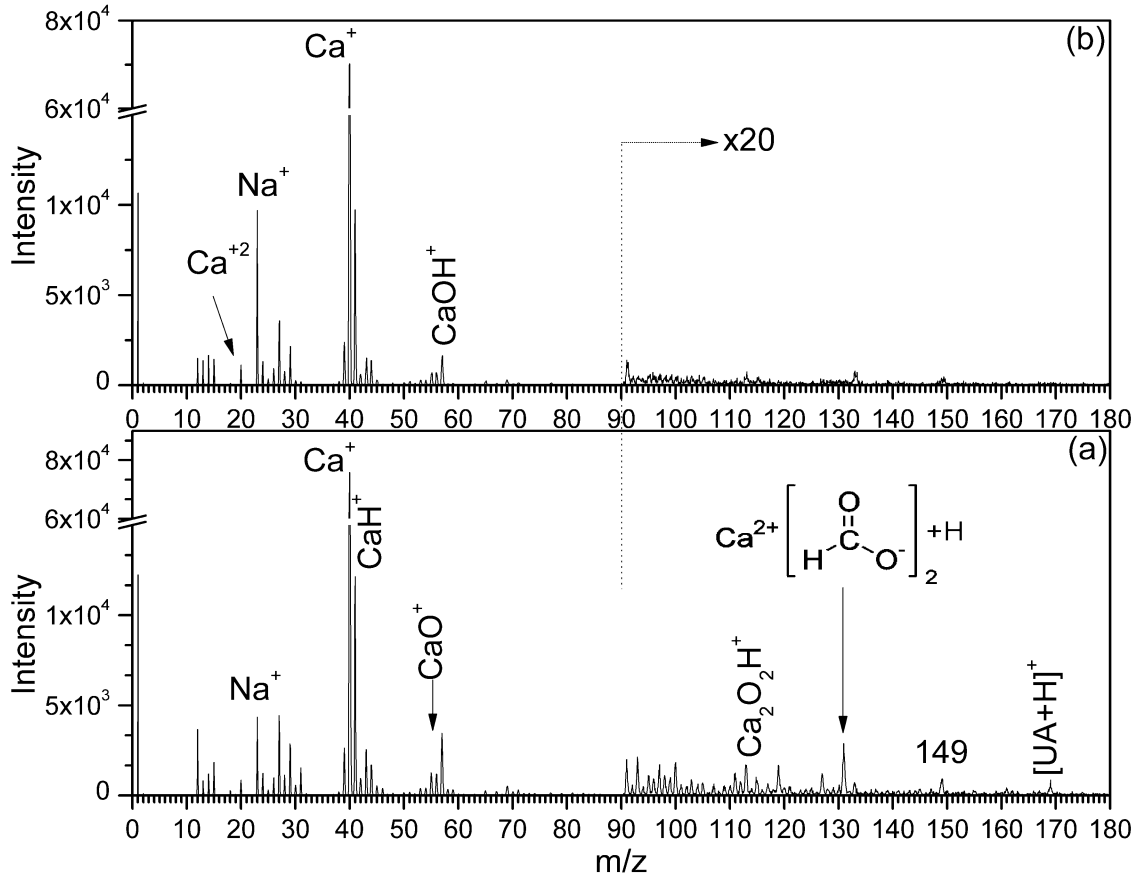

Figure 5.4. TOF-SIMS positive ion spectra of S3 (a) and S4 (b).

In positive ion mode (Figure 5.4), the major elemental component of these two stones is detected at *m/z* 40, Ca^+, along with other characteristic ions at *m/z* at 56 (CaO^+) and 57 ($CaOH^+$),

it might be interesting to mention here that a number of authors have mentioned these ions from calcium phosphates [29 reference therein]. In our study [26, 27, 29] we additionally reported doubly charged ion at *m/z* 20 (Ca^{+2}), dimmer calcium Ca_2^+ (*m/z* 80), oxide of dimmer calcium Ca_2O^+ (*m/z* 96), dimmer of calcium Oxide $Ca_2O_2^+$ (*m/z* 112), and the protonated dimmer at *m/z* 113 $[Ca_2O_2+H]^+$, the intensity of these peaks can be improved by pre-sputtering which is obvious for the spectra shown for S2 and S1 shown in Figure 5.2 and 5.3, respectively.

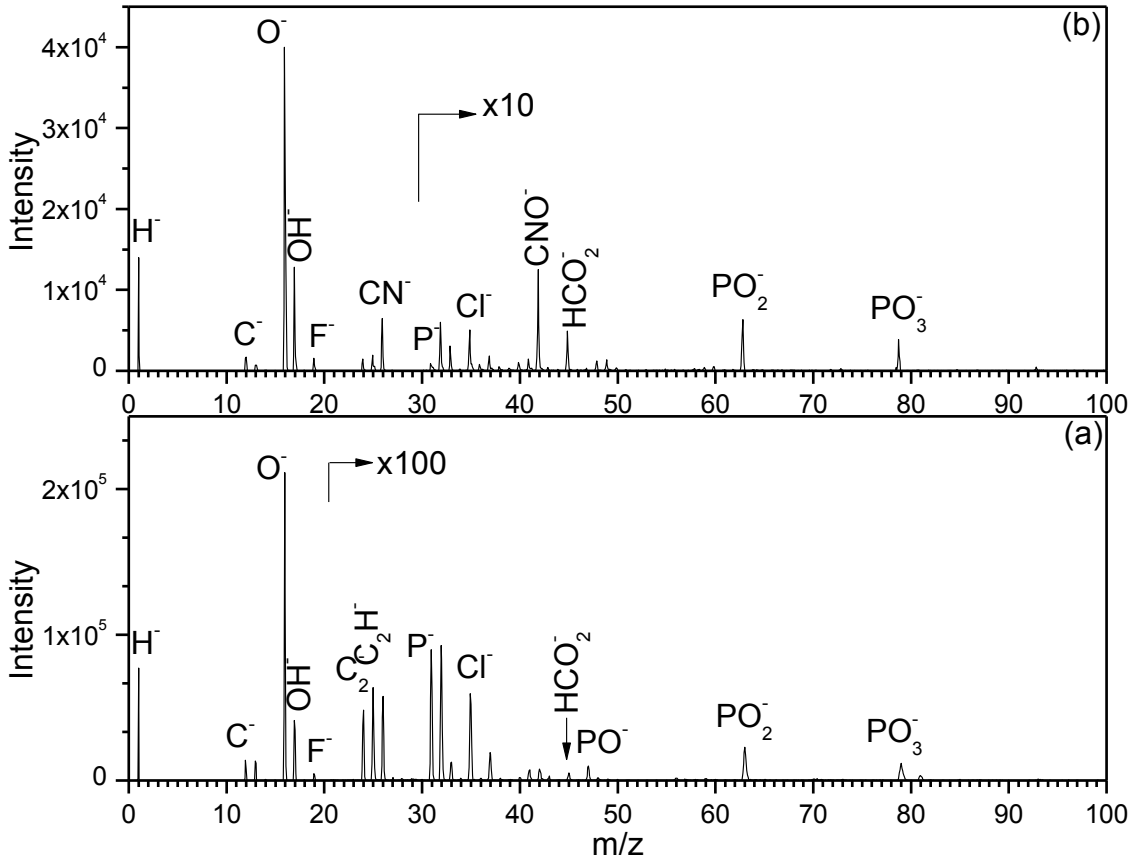

Figure 5.5. TOF-SIMS negative ion spectra of S3 (a) and S4 (b).

All these peaks are characteristic ion peaks of calcium oxalate already mentioned in above section. The two spectra look similar except for the presence of a peak at *m/z* 131 in Figure 5.4a; this is also the most intense peak above *m/z* 100. We considered this ion to be protonated calcium formate $[Ca(HCO_2)_2+H]^+$. All the peaks shown in Figure 5.4a, except for the protonated molecules at *m/z* 131, are similar to the characteristic peaks of calcium oxalate $Ca(CO_2)_2$ shown in Figure 5.4b. This indicates that the stone in S3 was calcified as calcium formate or, at least, induced in the presence of this component. Other minor components, which we found in this calculus, are uric acid, calcium phosphate, and glycerol. The presence of uric acid is evident from its protonated molecule $[M+H]^+$ at *m/z* 169 as discussed in uric acid stone analysis. The presence of glycerol is obvious from its characteristic ion peak at *m/z* 149, respectively. In both samples the ion characteristic of the calcium phosphate was present at *m/z* 103 ($CaPO_2^+$) although its intensity

was very low compared with that of the ion at *m/z* 96 (Ca_2O^+) detected in the spectra taken after pre-sputtering, common both to the CP family and to calcium oxalate (not shown here, the two spectra were quite similar to that shown in above section). The ratio of $(CaPO_2)^+/(Ca_2O)^+$ was found to be ca. 0.2 compared with the values of 0.5 to 4.5 obtained for the CP reference samples reported [29].

Recently, in our SIMS quantification study [29] we found that S3 and S4 contain 21.28±2.88 and 25.39±0.23 % assay composition of hydroxyapatite, respectively. The phase identification and quantification will be discussed in next chapter. In negative ion spectra (Figure 5.5) the presence of P^-, PO^-, PO_2^-, and PO_3^- ions for both samples confirms the presence of calcium phosphate as minor component. The presence of fluorine and chlorine is also evident from the elemental ion peaks of F^- (*m/z* 19) and Cl^- (*m/z* 35/37) in both samples.

5.1.3 Core and shell as complementary calcium oxalate and uric acid

We found at least two binary compositional renal stones of calcium oxalate and uric acid in which core and shell were developed as calcium oxalate and uric acid in one stone, and vice versa in other stone.

Four kidney stones (S5) of average size ca. 6 mm×6 mm with calcium oxalate core, shown in Figure 5.6 were obtained from a 73 years male patient in single episode. One can easily differentiate visually the core and shell through respective dark and light colors.

Figure 5.6: visual appearance of stones (S5) with dark brown core and light yellow shell.

The representative TOF-SIMS spectrum from the core of the stone (S5) with dark brown color is shown in Figure 5.7a. The major ion peaks (Ca^+, CaO^+, $CaOH^+$, Ca_2O^+, $Ca_2O_2H^+$) observed are identified and mentioned in the spectrum are representative of calcium oxalate . The relative intensity of $CaOH^+$ was 9.5% of the Ca^+ that is greater than the value obtained for S1 (8.55%), sample was also hard, comparable to S2 and the color is also dark. From all these observation, we can propose the core as being whewellite. We also observed the calcium adduct

ion peaks ($CaCN^+$, $CaCNO^+$) mentioned before corresponding to presence of trace amount of uric acid.

The representative TOF-SIMS spectrum from the light yellow shell is shown in Figure 5.7b in the *m/z* range 0-200, above *m/z* 100 the base peak corresponds to protonated uric acid molecules $[UA+H]^+$ at *m/z* 169. Other fragments of uric acid are also evident in the mass spectrum which is already discussed in detail in previous chapter. In this sample the main peak corresponding to glycerol at *m/z* 149 is also evident in reasonable intensity compared to uric acid protonated molecule.

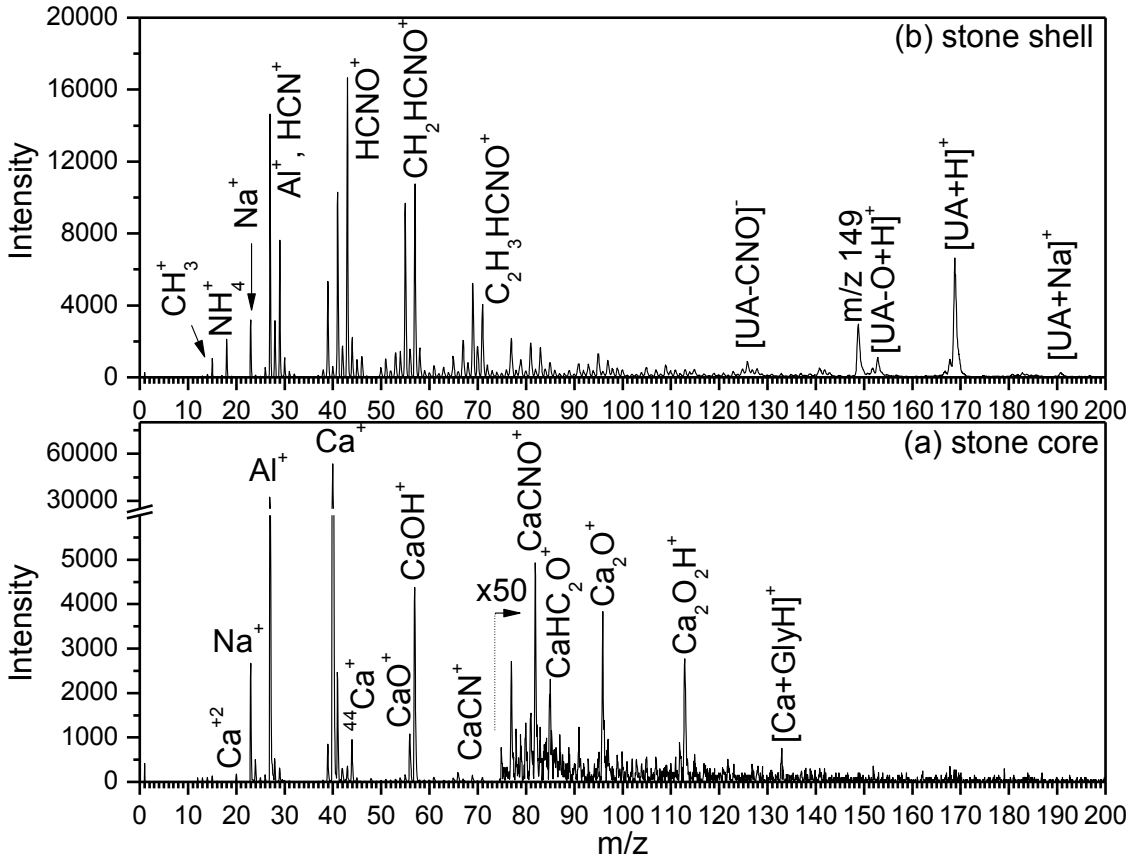

Figure 5.7: Positive TOF-SIMS spectra from (a) the core and (b) shell of stone S5

The set of mass spectra from the stone S6 (Figure 5.8) developed as calcium oxalate as shell on the uric acid core are shown in Figure 5.9. We can clearly see the complementary composition through the characteristic peaks mentioned in the two spectra corresponding to uric acid as core and shell as calcium oxalate.

The difference in the color is also evident; in multiple sampling we found more uric acid in inner layers of calcium oxalate shell with decreasing trend toward the surface of the stone. The clear rings in the inner layer of shell are believed to be uric acid and dark are of calcium oxalate as it is evident from the calcium oxalate spectrum representative of near surface area.

Furthermore, the relative intensity of $CaOH^+$ peak shown in Figure 5.9b is 11.76% of the base peak of elemental calcium, stone was also hard comparable to S2. The morphological observations and the SIMS analysis support to phase of mineralogy as whewellite.

Figure 5.8: visual appearance of stone (S6) with light yellow core and dark brown shell of layered texture.

In the core sample, the ion peak at 149 corresponding glycerol is greater than that of protonated uric acid $[UA+H]^+$. This relative intensity observed is also the greatest in uric acid samples analyzed so far with this technique. From this discussion one can conclude that core was mainly developed from glycerol by incorporation of uric acid crystals which are present even in healthy individuals.

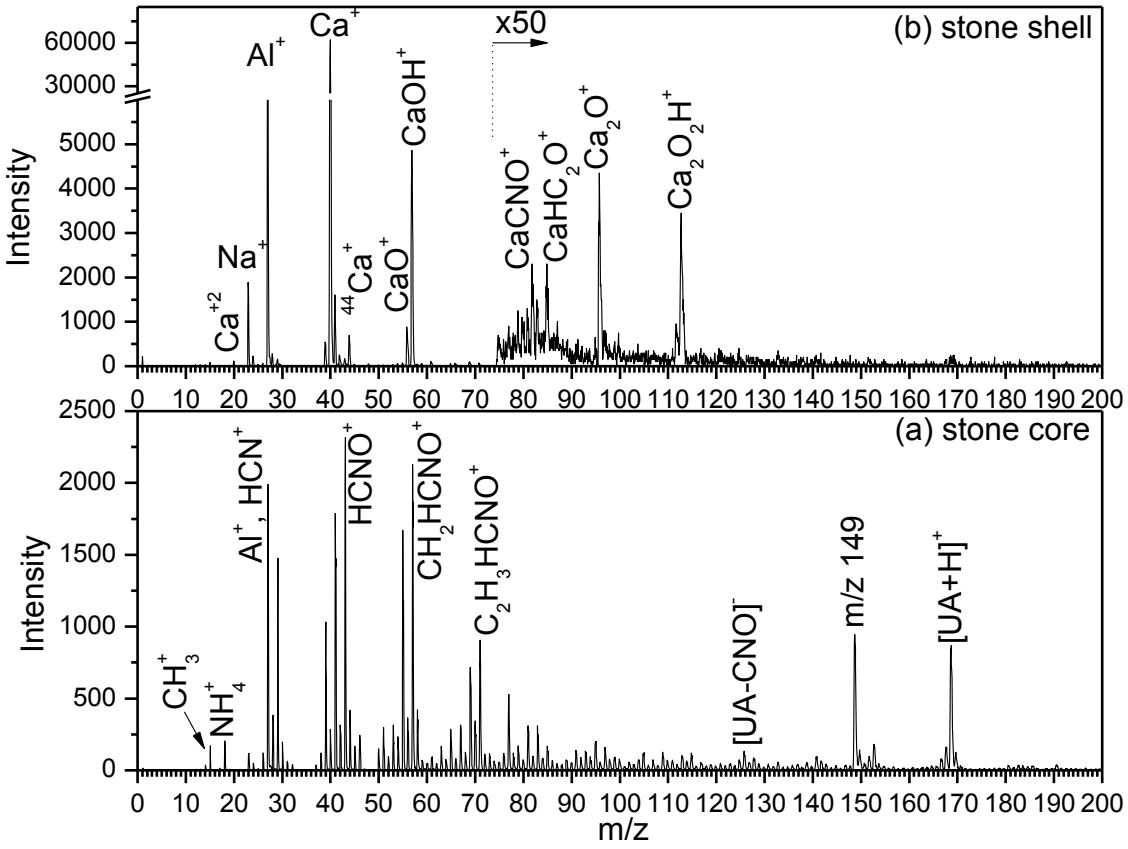

Figure 5.9: Positive TOF-SIMS spectra from (a) the core and (b) shell of stone S6

5.1.4 Compositional comparison of calcium oxalate stones with reference chemical

In this study we found at least nine binary human renal stones (S1-S9) with calcium oxalate as major component and calcium phosphate less than 50%. The amounts of calcium phosphate for six stones were published by the author in *Ghumman et al.* [29]. Table 5.2 and 5.3 show relative abundance of main characteristic peaks and the average intensity observed for these stones along with the reference calcium oxalate (Figure 5.2) reported in *Ghumman et al.* [29].

Table 5.2. Positive secondary ions measured for urinary stones (S1-S5).

Secondary ions		samples				
m/z	Species	S1	S2	S3	S4	S5
20	Ca^{2+}	0.103	0.161	0.252	0.427	0.231
23	Na^{+}	0.534	3.356	4.975	8.893	3.477
24	$Mg^{+}(C_2^{+})$	1.170	0.744	0.461	0.541	0.687
25	-	0.224	0.146	0.097	0.094	0.170
26	-	0.234	0.242	0.151	0.100	0.230
31	P^{+}	0.032	0.037	0.154	0.108	0.056
39	K^{+}	0.450	1.201	0.763	1.834	1.413
40	Ca^{+}	100	100	100	100	100
47	PO^{+}	0.015	0.008	0.045	0.044	0.056
48	$POH^{+}(C_4^{+})$	0.068	0.132	0.174	0.164	0.177
56	CaO^{+}	1.428	2.915	2.256	2.179	2.245
57	$CaOH^{+}$	8.890	13.78	12.914	10.608	9.537
80	Ca_2^{+}	0.043	0.071	0.049	0.061	0.072
96	Ca_2O^{+}	0.171	0.345	0.182	0.133	0.184
103	$CaPO_2^{+}$	0.014	0.021	0.040	0.048	0.032
112	$Ca_2O_2^{+}$	0.031	0.105	0.046	0.035	0.050
113	$Ca_2O_2H^{+}$	0.159	0.308	0.194	0.130	0.172
119	$CaPO_3^{+}$	0.009	0.014	0.025	0.013	0.017

The original mass spectrum of the reference calcium oxalate is shown in Figure 5.10. To have overall impression of these results, the change in the relative abundance of these species for the stones compared to that of reference calcium oxalate monohydrate was calculated by subtracting the intensity of reference calcium oxalate (Figure 5.2) from the average intensities of nine stones (S1-S9). This change in intensity is plotted in Figure 5.11.

We only observed negative change of -0.018 (-11.25%), in the ion species of C_4^{+} which corresponds to oxalate (C_2O_4). The decrease in the relative abundance of ion peak at $C_4^{+}(+POH^{+})$ is due to two factors; first the decrease in the calcium oxalate contents and second due to the overall increase in the Ca^{+} ion peak owing to calcium phosphate contents present in the stones. For all other species we observed relative enhancement in the intensities. The minimum change was observed for the water representing ion peak $CaOH^{+}$ which is only 4.98 % of the relative intensity for COX compared to increase of 46.43% for CaO^{+}. These results suggest that the

relative intensity of $CaOH^+$ could be a good candidate to recognize the presence of calcium oxalate at low concentration in binary mixture with calcium phosphate.

Table 5.3. Positive secondary ions measured for urinary stones (S1-S5), the average intensity of all nine samples (S1-S9), and calcium oxalate monohydrate (COX) reference chemical.

Secondary ions		samples					
m/z	Species	S6	S7	S8	S9	S1-S9	COX*
20	Ca^{2+}	0.147	0.141	0.190	0.263	0.213	0.203
23	Na^+	2.606	2.712	2.208	5.232	3.777	0.029
24	$Mg^+(C_2^+)$	0.326	0.105	0.180	0.379	0.510	0.147
25	-	0.086	0.027	0.094	0.105	0.116	0.030
26	-	0.113	0.102	0.101	0.152	0.158	0.046
31	P^+	0.017	0.013	0.069	0.066	0.061	0.002
39	K^+	1.140	1.461	0.629	0.961	1.095	0.037
40	Ca^+	100	100	100	100	100	100
47	PO^+	0.030	0.017	0.037	0.031	0.031	0.002
48	$POH^+(C_4^+)$	0.108	0.121	0.176	0.142	0.140	0.158
56	CaO^+	2.164	1.119	2.493	1.875	2.075	1.417
57	$CaOH^+$	11.763	7.717	11.455	6.549	10.357	9.865
80	Ca_2^+	0.068	0.045	0.095	0.061	0.063	0.046
96	Ca_2O^+	0.161	0.114	0.300	0.168	0.195	0.112
103	$CaPO_2^+$	0.015	0.004	0.029	0.055	0.029	0.002
112	$Ca_2O_2^+$	0.020	0.023	0.075	0.038	0.047	0.021
113	$Ca_2O_2H^+$	0.068	0.134	0.298	0.113	0.175	0.104
119	$CaPO_3^+$	0.007	0.007	0.016	0.012	0.013	0.002

**The relative abundance of the ion species reported in reference [29].*

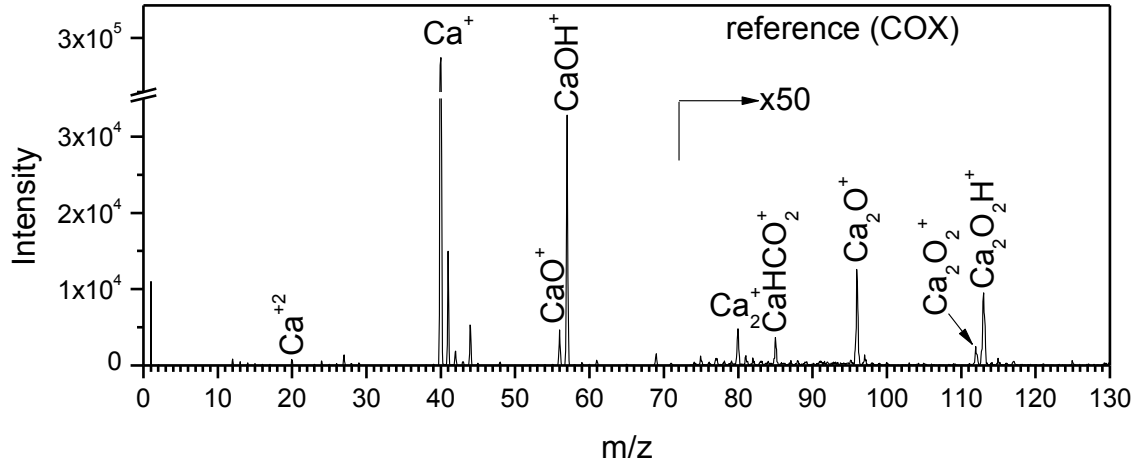

Figure 5.10. Positive ion mass spectrum of reference calcium oxalate.

The alkali and alkali earth metals were also observed in urinary stones which is evident by the observed positive change, although for some of them the change is insignificant e.g. presence of magnesium as compared to sodium (Na^+) and potassium (K^+). Furthermore, the presence of calcium phosphates in the real stones is also evident from the positive change observed for phosphate peaks (P^+, PO^+ , $CaPO_2^+$, $CaPO_3^+$) as shown in Figure 5.11. The quantification of calcium phosphate contents in these stones will be discussed in next chapter,

these measurements for six stones out of these nine stone is already reported [29]. The method of phase identification of calcium phosphates and their quantification [29] in calcium oxalate stones will be presented in next chapter.

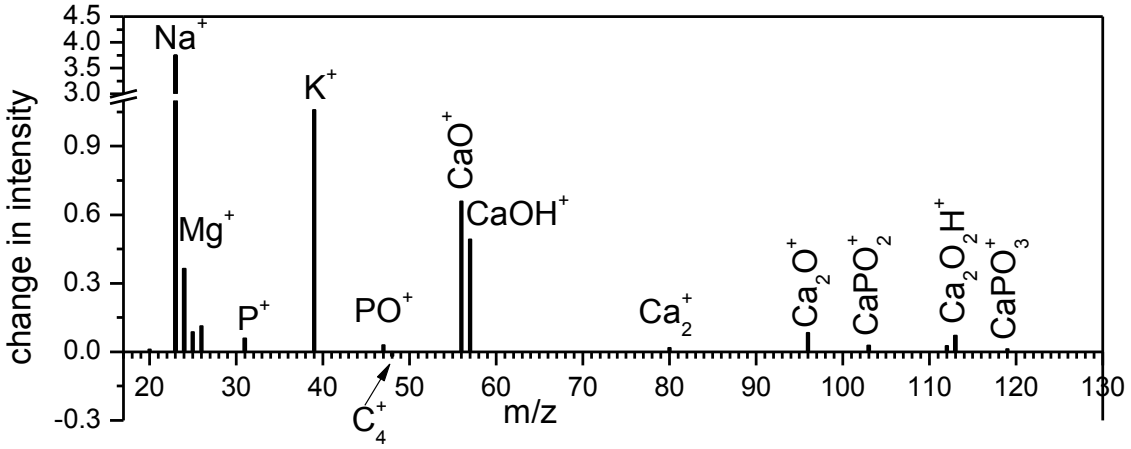

Figure 5.11. The change in the relative intensity of indicated species from the reference calcium oxalate chemical.

5.6 Doubly charged calcium ions yield enhancement

The ion species mentioned in Table 5.2 and 5.3 are singly charged ions except elemental calcium at *m/z* 20 which we often observed and reported in our studies. The formation of these ions is due to its low second ionization potential (EII=11.87eV) when compared with other elements especially alkali metals found in these samples (Table 5.4). In our experiment we found that the Ca^{+2}/Ca^{+} depends on the primary ion dose, higher the dose lower the relative intensity of doubly charged calcium as shown in Figure 5.12c. The data shown in Table 5.2 and 5.3 was produced with same experimental conditions keeping in mind ion beam damage effects.

Table 5.4. Ionization energy of few elements [National Physical Laboratory web site].

Element	1^{st} ionization energy (EI)	2^{nd} ionization energy (EII)
Li	5.39	75.60
Na	5.14	47.30
Mg	7.65	15.04
K	4.34	31.71
Ca	6.11	11.87
Cs	3.89	25.10

The observed Ca^{+2}/Ca^{+} is 4 times as bigger for S4 when compared with minimum 0.103% for S1. On comparison of Ca^{+2}/Ca^{+} ratios with the relative intensities of all other species shown in Table 5.2 and 5.3, we found linear correlation representing doubly charged calcium ions yield enhancement for the sodium (Figure 5.12a), sodium + potassium (not shown), and the peak ratio of $CaPO_2^{+}/Ca_2O^{+}$ (Figure 5.12b), where the ratio $CaPO_2^{+}/Ca_2O^{+}$ is the representative of amount of

calcium phosphate, higher the ratio bigger the amount of incorporated calcium phosphate, method of estimation of calcium phosphate will be discussed in next chapter.

From both these relations, we can conclude on the basis of *Pupyshev et al*. [128] study that presence of alkali metals and phosphate might decrease the total ionization potential (EI+EII) of the calcium present in matrix of the specimen or suppress the ionization of calcium neutrals while leaving the surface based on the electron tunneling model discussed in chapter#2. We will talk further on this issue in next chapter on the basis of amount of calcium contents in the matrix and other factors like amount of water etc where we observed more enhancements up to about 1.78%, which is 1.78 times higher than the reported value in *Pupyshev et al*. [128].

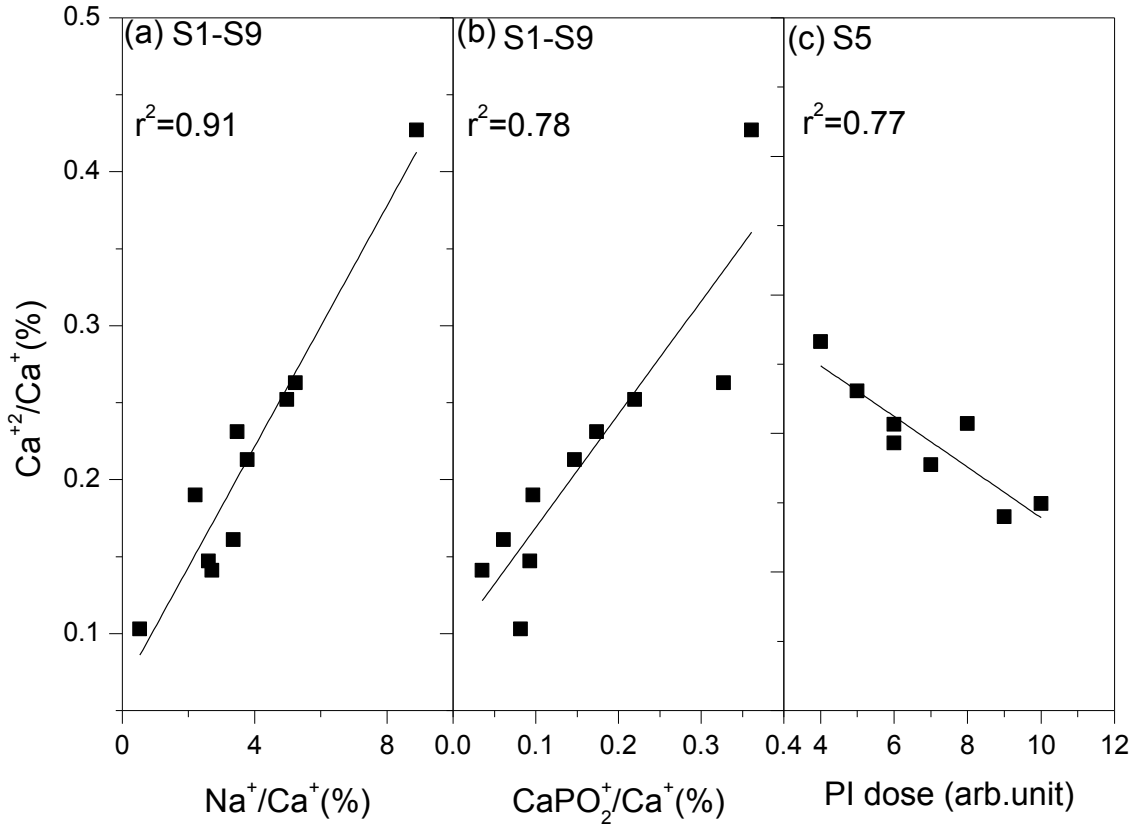

Figure 5.12. The relation of Ca^{+2}/Ca^{+} observed for (a) Na^{+}/Ca^{+}, (b) $CaPO_2^{+}/Ca^{+}$ observed for urinary stone samples (S1-S9), and average of all samples. Primary ion dose dependent (c) Ca^{+2}/Ca^{+} for single sample (S5).

6. TOF-SIMS analysis of calcium phosphate stones

In this chapter the results of calcium phosphates reference chemicals as well as human urinary stones will be presented. Based on the SIMS data, we proposed a new method for phase identification of reference calcium phosphates; hydroxyapatite, tri-calcium phosphate, dehydrated brushite, and calcium dihydrogen phosphate monohydrate. We will extend this model to recognize hydroxyapatite and brushite in mixed calcium oxalate stones and finally will use this method to quantify these components in real stone samples.

6.1 Calcium phosphate stones

The second major category of renal stones is calcium phosphate stones. Various calcium phosphate crystal phases occur in about one-third of stones; with apatite (apatite is a general term for calcium phosphate in which various anions, e.g. carbonate, fluoride, hydroxide, and chloride, are partially substituted) and brushite found most often admixed with calcium oxalates [129].

Apatite (or carbonate apatite) is a very frequent stone component with a 33% occurrence rate. Brushite does not appear frequently (1–2% occurrence rate), but its frequency has increased in the last years. The other calcium phosphates such as whitlockite and octacalcium phosphate are very rare [124].

Apatite stones are of white or gray color. The surface is mostly smooth, and the consistency ranges from solid to loose. Brushite stones are usually very hard. The color differs between white and gray. They often have a cauliflower-like surface [124].

In this study, we analyzed 6 kidney stones (Table 6.1) in which calcium phosphate was present as major component; here we will discuss some important results showing the potential of TOF-SIMS to recognize these stone components in pure and admixed stones. Furthermore, the

quantification of calcium oxalate and calcium phosphates identified in urinary stones S1-S9 (see chapter 5) will also be presented using new procedure proposed in the present study [29].

Table 6.1. Experimental conditions and classification of stones identified as calcium phosphates.

stone sample	presputtering with 5-15 $\times 10^{13}$ ions/cm^2	substrate used	Classification with TOF-SIMS
S10	Yes	Indium	brushite
S11	Yes	Indium	hydroxyapatite + struvite
S12	Yes	Indium	hydroxyapatite + calcium oxalate
S13	Yes	Indium	hydroxyapatite + calcium oxalate
S14	Yes	Al	hydroxyapatite + calcium oxalate
S15	Yes	Al	hydroxyapatite + calcium oxalate
S1-S9	see Table 5.1		

All reference samples presented in this chapter were prepared from the commercial chemical powders (Table 3.1) pressed on indium. The urinary stone samples were prepared on from their milled powder using indium and aluminum substrates according to two sample preparation techniques (cf. 3.6 and 3.7) for respective substrate.

6.1.1 TOF-SIMS analysis of brushite stone

This calculus (ca. 10mm×2.5mm in size) was sampled from a 76-year-old male patient with urolithiasis. The stone was very hard with a smooth surface of pale color.

The negative ion mass spectra for this sample (S10), and monetite reference chemical, are shown in Figure 6.1. The main peaks in these spectra appeared at *m/z* 31, 47, 63 and 79, corresponding to PO_n^+, where n=0-3. These ions confirm the presence of the phosphate; however, they cannot provide detailed compound information, as such ions are common for all calcium phosphate and struvite kidney stones. At the same time, the main ions representing oxalate are absent or very small compared to phosphate ions e.g. at *m/z* 45, 56, and 57 correspond to HCO_2^-, $C_2O_2^-$, and $HC_2O_2^-$ ions. The trace amount of nitrogen containing component is present in the stone sample that is most probably from uric acid, suggested by the presence of cyanide ion peak (CN^-, and CNO^-) although, no deprotonated ions were observed for uric acid. On the other hand, these peaks are absent or negligibly small for reference monetite (dehydrated brushite). To gain more structural and phase information, the positive ion spectra are crucial.

The positive ion mass spectrum shown in Figure 6.2a is of synthetic $CaHPO_4$ used as reference, while the top panel spectrum represents the kidney stone composition. In both spectra

the main ions are found at *m/z* 20, 31, 40, 47, 56, 57, 96,103, 119, 159 and 175. These peaks were identified as Ca^{+2}, P^+, Ca^+, PO^+, CaO^+, $CaOH^+$, Ca_2O^+, $CaPO_2^+$, $CaPO_3^+$, $Ca_2PO_3^+$ and $Ca_2PO_4^+$, respectively. The absence of Mg (most abundant isotope at *m/z* 24) confirms that the sample is neither struvite nor a mixture containing struvite; the analysis of this type of stones will be presented in next chapter. Calcium dihydrogen phosphate, hydroxyapatite and tri-calcium phosphate (discussed in next sections) exhibit the same ions; only differences in the ratio of intensities of some characteristic peaks help us to distinguish between the different phases. For monetite (or brushite), the $CaPO_2^+/Ca_2O^+$ ratio is high, while for HAP and whitlockite (tri-calcium phosphate) it is low or close to unity. The peak for the dimeric ion Ca_2^+ at *m/z* 80 is also small for monetite. The presence of water component in the stone sample is also obvious from the relatively large ratio of $CaOH^+/CaO^+$ compared to monetite, which is only the chemical difference between brushite and monetite. Thus, the comparison of the spectra of the kidney stone and the commercial reference compound clearly indicates that this kidney stone can be classified as brushite (calcium hydrogen phosphate dihydrate). Why it cannot be classified as any other phase of calcium phosphate, we have to go through the following sections.

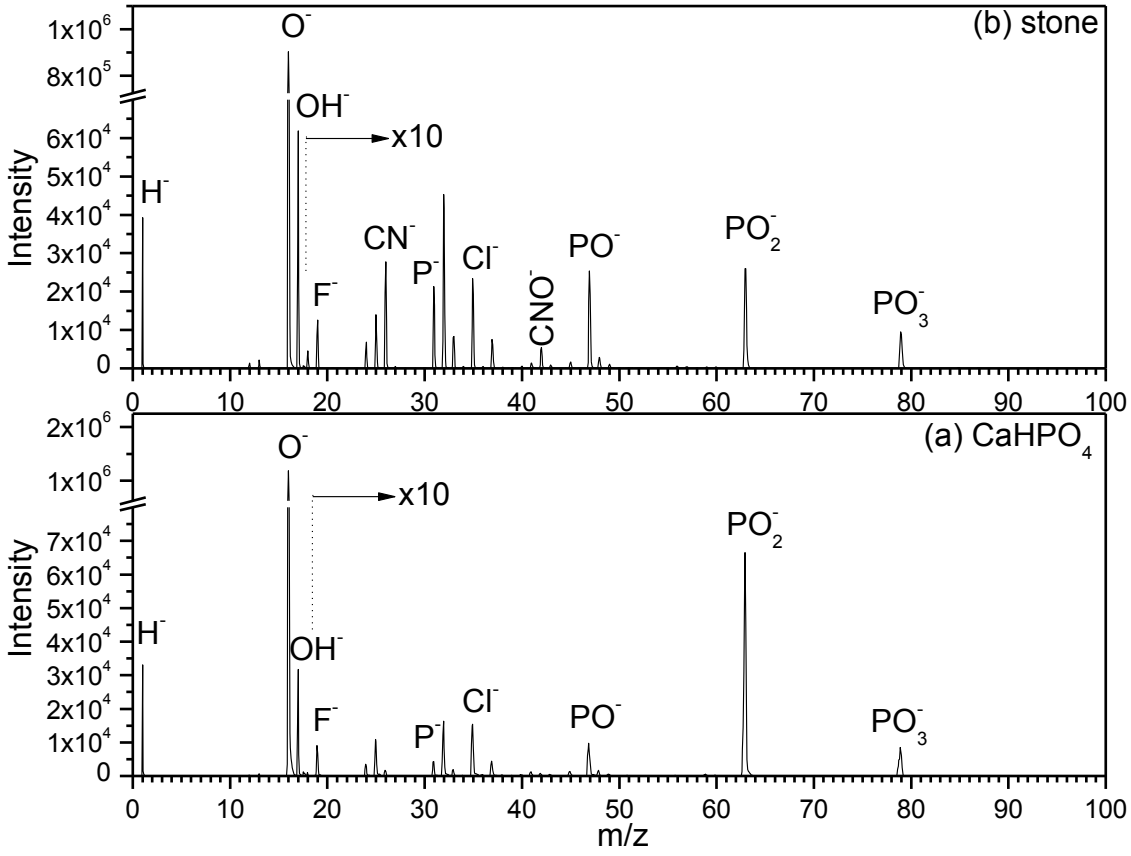

Figure 6.1. The re-examined [29] negative ion TOF-SIMS mass spectra of (a) reference monetite ($CaHPO_4$, dehydrated brushite) and (b) stone (S10) reported in reference [26].

In our study [26, 29], we observed that the $CaPO_2^+$ and Ca_2O^+ peaks are more pronounced and stable than other peaks, and they were deployed for phase identification in calcium phosphate compounds. Reproducibility is more easily achieved than with the negative ion peaks PO_2^- and PO_3^-, which were used by *Chusuei et al*. [34] for phase identification in various reference calcium phosphate powders under $(CsI)_nCs^+$ and C_{60}^+ cluster ion bombardment in static SIMS regime. Later other authors [35] also tried phase identification with monatomic Cs^+ as analytical primary ion sources but with less success. However, these studies are limited and insufficient for the study of real samples, such as kidney stones which are often admixed with other components like calcium oxalate and struvite; we will discuss in detail the phase identification of different calcium phosphates in next section.

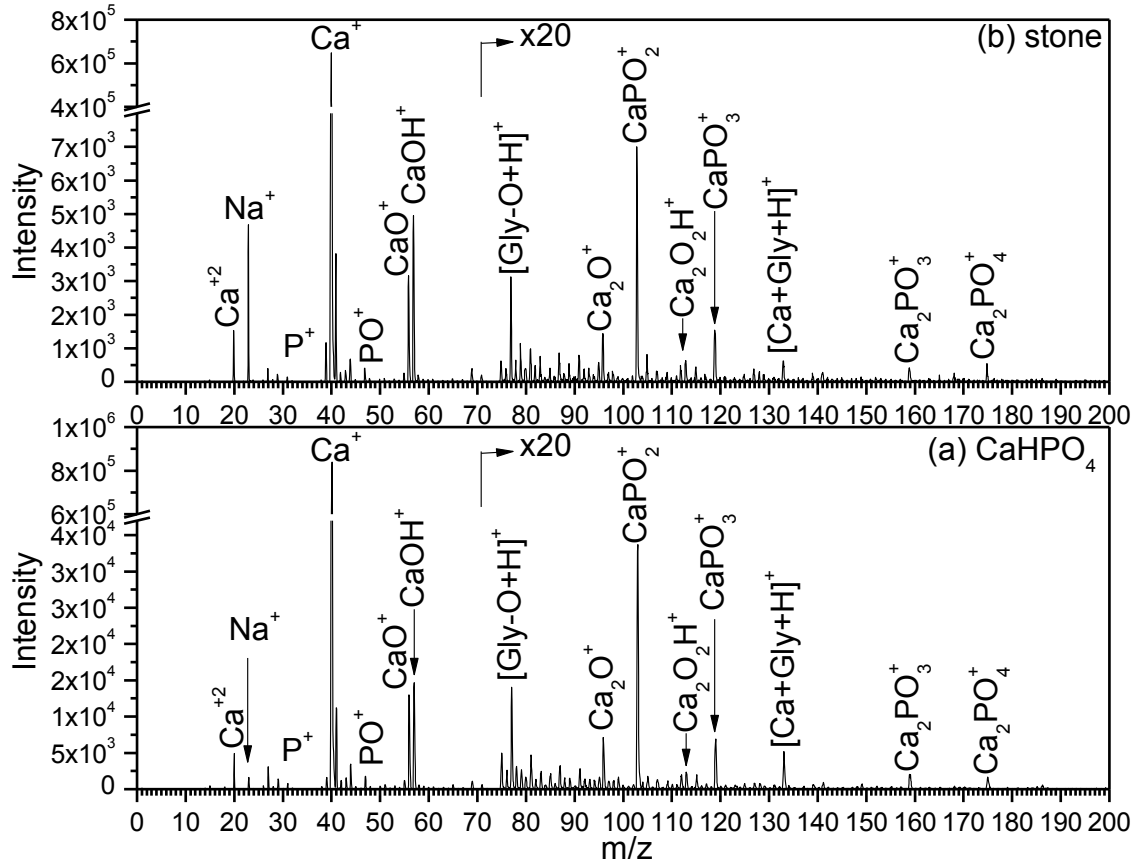

Figure 6.2. The re-examined [29] positive ion TOF-SIMS mass spectrum of (a) reference monetite ($CaHPO_4$) and (b) stone (S10) reported in reference [26].

6.1.2 TOF-SIMS analysis of hydroxyapatite stone

Apatite is the most frequent calcium phosphate component in the renal stones. In this study we found these stones often admixed with calcium oxalate, and struvite as major and minor component. The morphology of the stone characterized as apatite is shown in Figure 6.3.

The representative spectra of the stone (S11) and reference apatite are shown in Figure 6.4. The mass peaks at *m/z* 31, 47, 63, 79 are related to P^-, PO^-, PO_2^-, and PO_3^-, which we also observed in the case of brushite as discussed earlier. Fluorine (F^- *m/z* 19), chlorine (Cl^- *m/z* 35, 37), and nitrogen containing ion peaks of CN^-, CNO^- were also identified which are associated ions commonly observed for calcium phosphate and struvite, respectively. The ratio of ion peaks OH^+/O^+ was also 3 times higher than in the reference apatite which might be due to water containing component, such as struvite. However, complete identification was achieved through positive spectra.

Figure 6.3. The morphological appearance of apatite stone (S11), two different views of same stone.

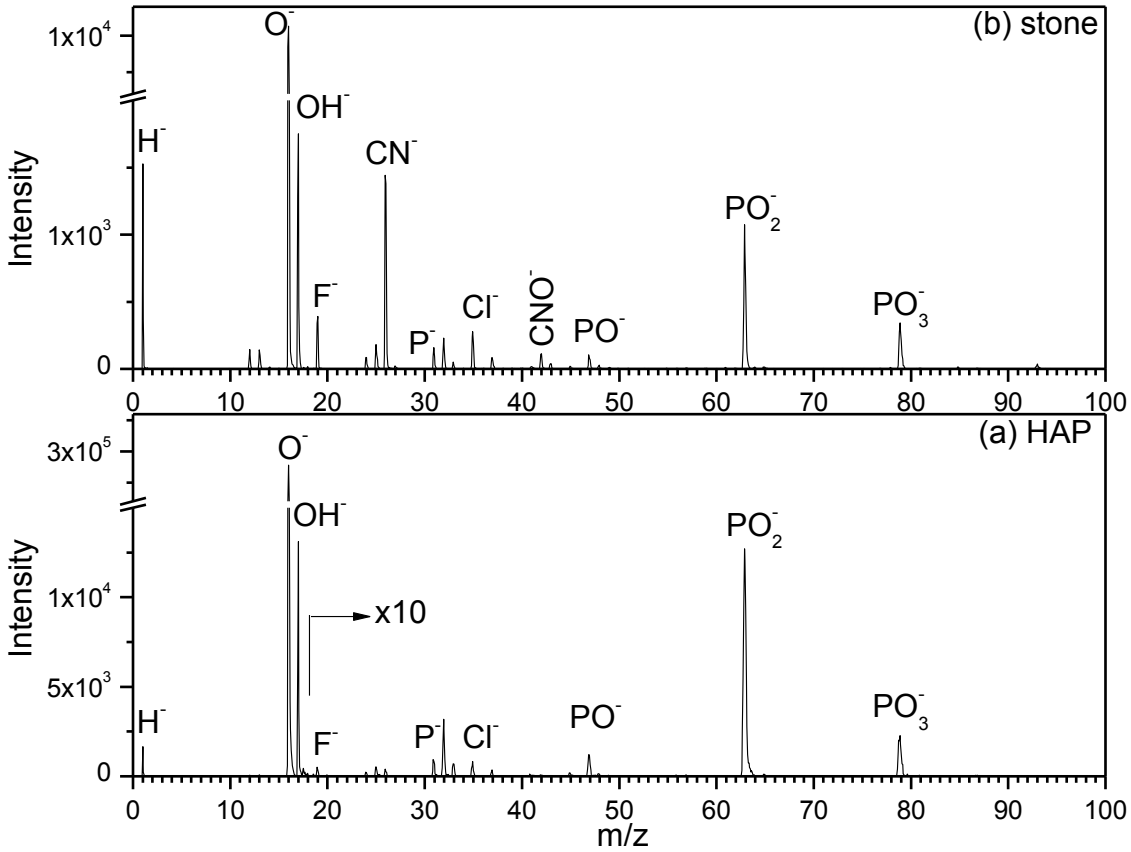

Figure 6.4. Negative TOF-SIMS spectra of (a) reference hydroxyapatite (HAP) and of (b) renal stone (S11).

The positive ion spectrum shown in Figure 6.5a is of a reference hydroxyapatite (HAP), while the top panel (Figure 6.5b) represents the kidney stone (S11) composition. In both spectra the main ions are found at *m/z* 20, 31, 40, 47, 56, 57, 80, 96,103, 119, 159 and 175 same as in the case of brushite and monetite discussed above. These peaks are identified as Ca^{+2}, P^+, Ca^+, PO^+, CaO^+, $CaOH^+$, Ca_2^+, Ca_2O^+, $CaPO_2^+$, $CaPO_3^+$, $Ca_2PO_3^+$ and $Ca_2PO_4^+$, respectively. The relative signal intensities of the stone (S11) is very close to the relative signal intensities of reference HAP. In both, stone and reference samples we observed $CaCl^+$ ion peaks at *m/z* 75/77 which is relatively strong especially in stone sample as compared to brushite stone (S10) due to strong association of chlorine with apatite, the higher relative abundance at *m/z* 77 is due to interfering

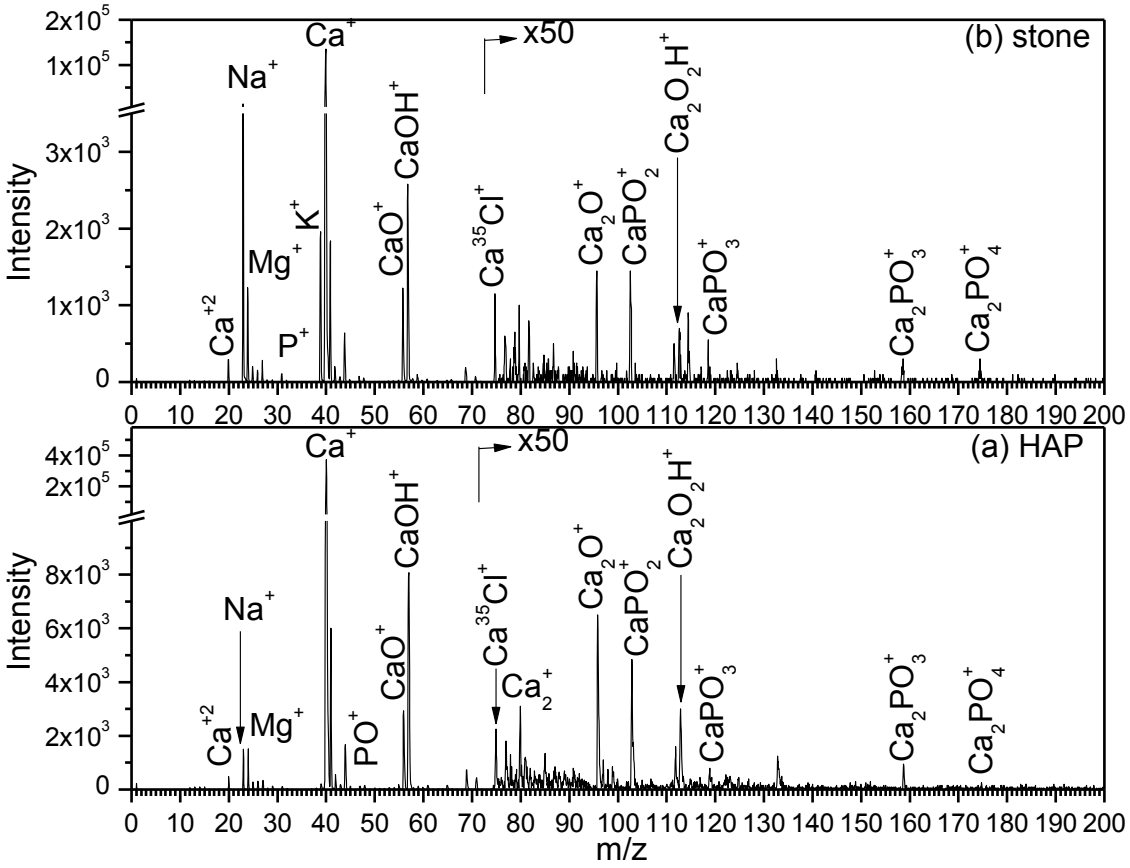

Figure 6.5. Positive TOF-SIMS spectra of (a) reference HAP and of (b) renal stone (S11)

hydrocarbon ion species. The presence of Mg (most abundant isotope at *m/z* 24) was also identified in reference as well as stone sample, in case of stone it is due to struvite component while in reference apatite is due to magnesium impurity (0.2%) . The major phase identification of the stone as being apatite was achieved through the ratio $CaPO_2^+/Ca_2O^+$ of 1.0 which is quite close to that 0.8 for HAP in the given spectra. In case of stone sample, higher $CaPO_2^+/Ca_2O^+$ is due two reasons;

(1) the relative low ion beam damage which is evident through the re-sputtered accumulative gallium signal intensity of 0.23% (stone) compared to 0.46% (HAP) of calcium ion peak,

(2) the presence of alkali (Na^+, K^+) and alkali earth (Mg^+) metals which are in reasonable amount. The presence of hydroxyl (OH) component in the stone sample is also obvious from the relatively large ratio of $CaOH^+/CaO^+$ compared to monetite (Fig 2a). In conclusion the kidney stone was identified as apatite.

6.1.3 TOF-SIMS analysis tri-calcium phosphate

We did not identify any Tri-calcium phosphate (TCP) as major stone component because this type of calcium phosphate is very rare; its occurrence frequency is as low as 0.03% as major component and 0.1% is its total occurrence rate [124]. However, we found TCP as mixture with struvite, with component occurrence frequency of 30%, and will be discussed later in next chapter concerning struvite analysis; here we will only present the results of reference TCP chemical.

The positive and negative mass spectra are shown in Figure 6.6. The negative ions spectra contain phosphate ions (P^-, PO^-, PO_2^-, and PO_3^-) which are already discussed previously in hydroxyapatite and brushite analysis. The abundance of relative intensities of these species are quite similar to that observed for hydroxyapatite and monetite but different to that of brushite. The peak ratio OH^-/O^- (0.04) is quite same as that of HAP (.05), although it is a bit smaller. The signal intensities of chlorine and fluorine are smaller than that of HAP. In conclusion, it is quite difficult in negative ion mode to differentiate between TCP and HAP because of their quite similar chemical compositions of $Ca_{0.6}(PO_4)_{0.4}$ and $Ca_{0.55}(PO_4)_{0.33}(OH)_{0.11}$ except absence and presence of hydroxyl (OH) group, whose effect is usually suppressed by the water adsorption, present even under UHV conditions. Others have also reported difficulty in the identification of these two calcium phosphates in the negative ion mode [130]. However, we have successfully identified the two phase of calcium phosphate in positive ion mode.

The positive ion spectrum of reference TCP is shown in Figure 6.6a. We observed almost twice the total ion yield compared to HAP under same experimental conditions. Almost three times lower the peak ratio $CaOH^+/Ca^+$, and two times great peak ratio of PO^+/POH^+ mainly because of absence of hydroxyl (OH) group. The most decisive identification was achieved through $CaPO_2^+/Ca_2O^+$ which is higher than HAP depending on the stoichiometric PO_4/Ca ratio,

higher the stoichiometric ratio leads to higher peak ratio of $CaPO_2^+/Ca_2O^+$, this trend we observed in general for all calcium phosphates even when mixed with calcium oxalate.

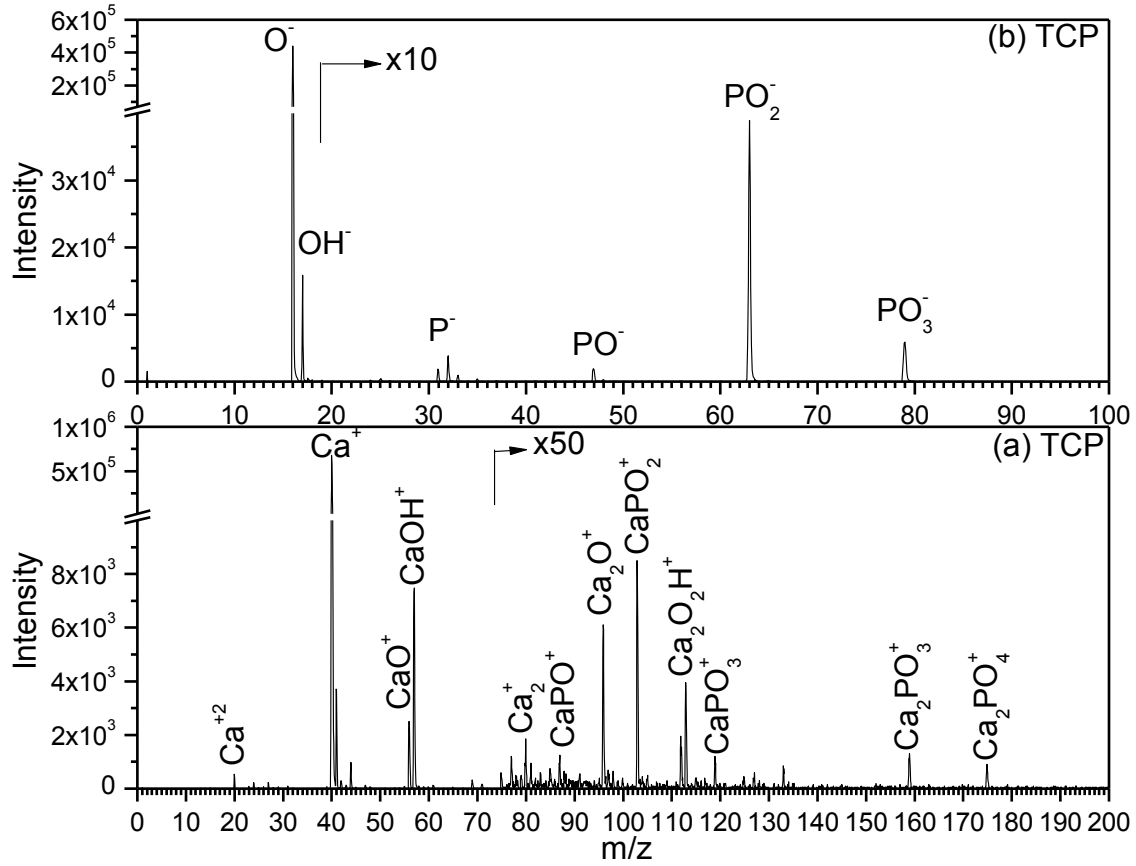

Figure 6.6. Positive (a) and negative ions (b) TOF-SIMS spectra of reference TCP $Ca_3(PO_4)_2$.

6.2 Phase identification of calcium phosphates

In the present study, chemical composition of 38 real human stones was measured and compared with the results obtained for the reference chemicals. We found 14 stones containing calcium oxalate (as major or minor component) with calcium phosphates, struvite, and uric acid. Here, we will discuss the phase identification of the synthetic calcium phosphates and their quantifications in twelve human calculi identified as calcium oxalate, calcium phosphates, and their mixtures.

The main positive secondary ions observed for calcium oxalate monohydrate (COX), hydroxyapatite (HAP), tri-calcium phosphate (TCP), dehydrated brushite (DB), and calcium dihydrogen phosphate monohydrate (CDHP) are listed in Table 6.2, the representative mass spectra of these reference chemicals are already discussed before except calcium dihydrogen phosphate monohydrate. The representative mass spectrum calcium dihydrogen phosphate

monohydrate is shown in the appendix B. The peak intensities were integrated within ±0.5 *m/z* and scaled to the intensity of $^{40}Ca^+$ peak. The sum of the peak intensities (in counts per second) for every sample studied is presented at the bottom of the Table 6.2.

Table 6.2: Positive secondary ions measured for calcium oxalate monohydrate (COX), hydroxyapatite (HAP), tri-calcium phosphate (TCP), dehydrated brushite (DB) and calcium di-hydrogen phosphate monohydrate (CDHP) reference chemicals.

Secondary ions		Reference sample				
m/z	Species	COX	HAP	TCP	DB	CDHP
20	Ca^{2+}	0.203	0.083	0.037	0.165	1.781
23	Na^+	0.029	0.221	0.009	0.077	0.226
24	$Mg^+(C_2^+)$	0.147	0.217	0.019	0.005	1.846
25	-	0.029	0.040	0.004	0.003	0.269
26	-	0.046	0.045	0.007	0.031	0.292
31	P^+	0.002	0.026	0.008	0.042	0.630
39	K^+	0.037	0.042	0.013	0.150	0.682
40	Ca^+	100	100	100	100	100
47	PO^+	0.001	0.037	0.016	0.113	2.487
48	$POH^+(C_4^+)$	0.158	0.038	0.010	0.029	0.270
56	CaO^+	1.417	0.906	0.367	0.946	2.304
57	$CaOH^+$	9.864	3.189	1.284	1.166	1.583
69	Ga^+	0.780	0.265	0.055	0.127	0.913
71	Ga^+	0.192	0.159	0.030	0.066	0.506
80	Ca_2^+	0.046	0.020	0.006	0.013	0.030
96	Ca_2O^+	0.111	0.051	0.023	0.032	0.025
103	$CaPO_2^+$	0.001	0.036	0.026	0.169	0.542
112	$Ca_2O_2^+$	0.021	0.012	0.006	0.011	0.012
113	$Ca_2O_2H^+$	0.103	0.026	0.014	0.016	0.012
115	In^+	0.007	0.003	0.001	0.015	0.050
119	$CaPO_3^+$	0.001	0.007	0.004	0.038	0.181
	Sum (cps)	649 ± 1	5171 ± 3	8705 ± 4	14073 ± 5	1367 ± 2

All the reference samples are characterized by the same peaks but with different relative intensities. For COX (without phosphate) the peak of *m/z* 48 can be mainly attributed to C_4^+ instead of POH^+. Common contaminations like different hydrocarbons, alkaline (Na^+, K^+), and alkaline-earth (Mg^+) metals were observed for all reference chemicals as well as for the real samples excepting Mg^+; hydrocarbons were completely removed by pre-sputtering (ion-beam

etching), whereas other species were only partially eliminated. The Ga^+ peaks in Table 6.2 were originated from the implanted primary ions after pre-sputtering. The high relative signal of gallium in CDHP, COX, and HAP is due to the low ion yield of $^{40}Ca^+$, and it might also be due to greater gallium dose used. However, in the real samples, the intensity of gallium was less than 0.75% of the principal calcium ion signal.

In the negative spectra, the presence of phosphate (PO_4) is usually justified via their fragments with *m/z* 31 (P^-), 47 (PO^-), 63 (PO_2^-), and 78 (PO_3^-), which are the characteristic peaks for all samples containing PO_4 in the stoichiometric compositions. The approach based upon the relative PO_3^-/PO_2^- peak intensities for phase identification in six reference calcium phosphates, including four samples studied in our work, was investigated [34, 35] with $(CsI)_nCs^+$, Cs^+, and C_{60}^+ as primary ions. The PO_3^-/PO_2^- ratio was found to be within the range from 0.51 to 2.6. In both these studies, the poor phase identification was reported for HAP and TCP, and the authors [34, 35] concluded that in case of the routine analysis of real samples with impurities, these phases might be undistinguishable. However, the DB and CDHP were easily distinguishable from each other and, from HAP and TCP. The standard deviation (*SD*) of the peak ratios for these four calcium phosphates is ca. 0.83 [35]. G. Schubert et al. [124] reported 78.9% of human calculi are of calcium oxalate (70%), calcium phosphates (1.5%) and their mixtures (7.4%). This scenario can be different depending upon the geographical origin of the sampling; the quantification of calcium phosphate can be quite complicated using negative SIMS mode for these complex samples. We used this mode only to confirm the presence of phosphate in the reference chemicals and real samples. In this mode, we have also identified the presence of Cl^- and F^- in all samples with and without pre-sputtering because of their high secondary ion yields.

In positive SIMS mode, the molecular ions (polyatomic ions), containing both electropositive and electronegative elements are observed allowing the quantification of stone components by selecting the most reliable characteristic peaks. We selected four molecular ion peaks with *m/z* 47 (PO^+), 48 (POH^+ ($+C_4^+$)), 96 (Ca_2O^+), and 103 ($CaPO_2^+$) for phase identification in CPs and for quantification of that component in binary stones. In our experimental study on the different CP powders, we observed that under the same experimental conditions the PO^+/POH^+ ratio is reproducible and ranges from ca. 0.9 for HAP to 9.0 for CDHP with SD ca. 3.74. The intensity of calcium oxide Ca^2O^+ depends on the elemental concentration in molecular formula of calcium phosphate that increases with the increase of Ca content. Also, the intensity of $CaPO_2^+$ increases with the increase of PO_4 concentration in the molecular formula. The other peak ratio $CaPO_2^+/Ca_2O^+$ ranges from ca. 0.7 to 21 with SD ca. 9.88 for CP group having the PO_4/Ca ratio in their molecular formulae of 0.6 (HAP), 0.67 (TCP), 1.0 (DB), and 2.0 (CDHP). The standard deviation achieved in our approach is much better than the earlier reported

phase identification studies.[34, 35] The experimental plots of PO^+/POH^+ and $CaPO_2^+/Ca_2O^+$ peak ratios for four reference calcium phosphates versus the stoichiometric PO_4/Ca ratio in their molecular formulae are shown in Figure 6.7. The large dynamic range (confidence interval) of these ratios guaranties reliable phase identification within CP group. In Figure 6.7, one can see that the stoichiometric PO_4/Ca ratio in HAP and TCP are rather close; the phase identification based upon only one pair of the peak ratio might be difficult if the experimental conditions were not well reproducible. For example, we observed that $CaPO_2^+/Ca_2O^+$ ratio considerably decreases after pre-sputtering because of the higher sputter yield of phosphate (9.71) as compared with calcium (7.47), whereas PO^+/POH^+ ratio increases because of efficient sputtering of hydrogen (36.09) (the sputter yields were measured upon 5 keV Ga^+ bombardment at an incident angle of 88º [131]). An error because of the difference in sputter yields can be minimized via the separate quantification using two ratios with subsequent averaging of the obtained results. For the stone samples, we mapped the two ratios in the respective graphs at average content of calcium phosphate giving minimum standard error (SE), calculated from the two ratios for COX with DB and HAP.

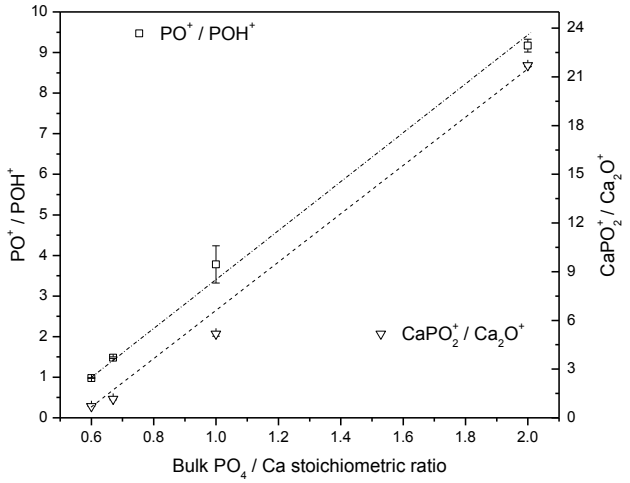

Figure 6.7. Secondary ion peak ratios of PO^+/POH^+ and $CaPO_2^+/Ca_2O^+$ measured for four calcium phosphate references versus their stoichiometric PO_4/Ca ratio.

Identification of pure calcium oxalate can be justified by the presence of Ca^+, CaO^+, Ca_2O^+, $Ca_2O_2^+$, and $Ca_2O_2H^+$ ions and, at the same time, by the absence of all phosphate containing ion peaks both in positive and negative mass spectra [26, 27, 29]. In our study, we found three pure (above 95%) COX with both the above mentioned peak ratios close to zero and one calcium phosphate with PO^+/POH^+ ratio of 4.50 and $CaPO_2^+/Ca_2O^+$ ratio of 4.77; this sample is distinguished as brushite (S10) according to the data shown in Figure 6.8(a) and (b). The dehydrated brushite exhibits these peak ratios of 3.84 and 5.14, respectively. In real human stones, we have not obtained these pair of peak ratios higher than in the sample (unique)

distinguished as brushite calculi. The peak ratios for CDHP (9.17 and 21.70) are much bigger than in the case of DB; one can say with certainty that the calcification of CDHP as human stone is negligible. The remaining eleven calculi are the mixture of calcium oxalate as major or minor component with calcium phosphates.

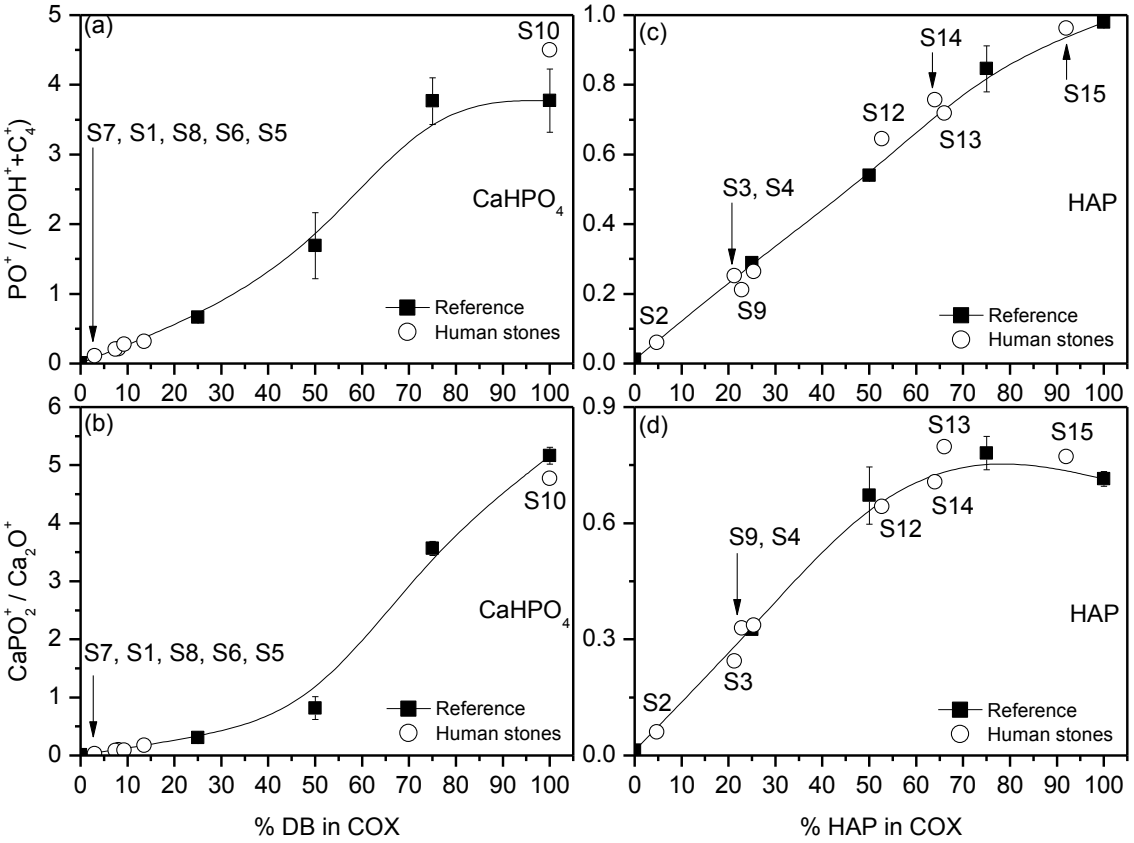

Figure 6.8. Secondary ion peak ratios of PO^+/POH^+ and $CaPO_2^+/Ca_2O^+$ measured for binary mixture of COX with DB [(a) and (b)] and HAP [(c) and (d)] versus their percentage in total mass. The pair of peaks ratios is also plotted for the real human calculi S1–S10, S12-S15 indicating by open circles, for renal stones cross reference with Ghumman et al. [29] look at Table 6.3.

Table 6.3. Names assigned to urinary stones in present work and reference [29]

Present work	S1	S2	S3	S4	S5	S6	S7	S8	S9	S10	S11	S12	S13	S14	S15
Reference [29]	S6	--	S8	S5	--	--	S7	S2	S4	S1	--	S3	--	--	--

Samples prepared of the reference binary mixture of calcium phosphates HAP and DB with COX mostly occurring in human stones were analyzed. The same two pair of the peaks, which were used for phase identification in pure references, was selected. The idea behind this selection was that when we mixed calcium phosphate with calcium oxalate, the calcium concentration increases as compared with PO_4 contents. Higher calcium concentration gives increased intensity of Ca_2O^+; also, the intensity of $CaPO_2^+$ decreases because of the overall

decrease in calcium phosphate concentration. The ratio of these peaks was calculated and plotted in Figure 6.8 as a function of percentage mass concentration. In the case of DB, the increasing trend for both pair of the peak ratios is obvious although not in linear manner. For HAP, the peak ratio $PO^+/POH^+(+C_4^+)$ increases from 0 (COX) to ca. 0.97 (HAP) as a function of HAP concentration, whereas for lower concentration, the $CaPO_2^+/Ca_2O^+$ ratio increases and saturates at 75% and then decreased for 100% HAP.

We incline to attribute such behavior to an increase in the ion yield of Ca_2O^+ as compared with $Ca_2O_2^+$+$Ca_2O_2H^+$ in pure HAP (Figure 6.5a). For 25% COX concentration, the intensity of $Ca_2O_2^+$+ $Ca_2O_2H^+$ exhibits the greatest gain as against Ca_2O^+ intensity as shown in Figure 6.9. For various HAP concentrations in COX, the pair of peak ratios is within the range from 0 to 1, whereas for DB mixture, the peak ratios increase from 0 to 5. The real human stones, giving these peak ratios above 1.0, are distinguished as brushite mixture, whereas it is rather difficult to do for the peak ratios less than 1.0. However, the identification and quantification of calcium phosphate are feasible by considering the total ion yield of all characteristic peaks including the intensity of doubly charged calcium positive ions at *m/z* 20. The relative different ion yield observed for doubly charged calcium will be discussed in next section.

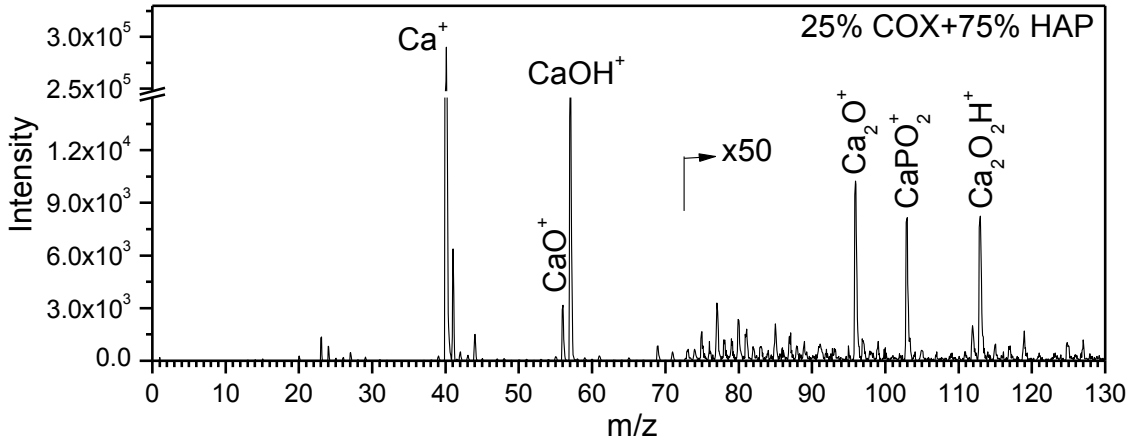

Figure 6.9. Positive TOF-SIMS spectrum of reference binary mixture of COX (25%) and HAP (75%).

For thirteen real stones, these ratios were found <1.0. One can see that the human calculi designated in Figure 6.8 as S1, S5-S8, and S10 best match with dehydrate brushite for both peak ratios with the estimated percentage of mass concentration (*mean value*±SE) ca. 7.43±0.80, 13.53±1.11, 9.26±1.71, 2.99±1.11, 8.07±0.21, and 100±0.00, respectively. The S2–S4, S9, and S12-S15 samples are more likely the mixture of HAP and COX with the estimated percentage of ca. 4.71±0.62, 21.28±2.88, 25.39±0.23, 22.83±2.24, 52.69±3.09, 66±1.50, 64±1.50, and 92±2.50 respectively. Here, it might be interesting to mention that the stones identified as mixture with HAP have Na^+ ion signals ranging from 20% (S12) to 3.3% (S2) of principal ion peak of calcium

while identified as mixture with brushite have less than 3.5%. The signals of K^+ and Mg^+ in all stone were less than 4.5% (S12) and 1.8% of the Ca^+, respectively. The S11 is not included in the graph due to presence of ca. 15% stoichiometric struvite component with ca. 84% hydroxyapatite which will be discussed in next chapter.

6.2.1 Matrix dependent ion yield observed for doubly charged calcium (Ca^{+2})

In this study, we only observed doubly charged specie of calcium in accountable relative intensity. In previous chapter we correlated the relative ion yield of the doubly charged calcium with the presence of matrix species present in the sample. Here we found different relative intensity of Ca^{+2} for reference calcium phosphates as shown in Table 6.2. The physical relation which we found is the % atomic contents of calcium in the matrix. The Ca^{+2} increases (mainly due to presence of P and O) with decreasing % calcium atomic concentration in the analyte sample as shown in Figure 6.10. The maximum relative intensity (Ca^{+2}/Ca^+) measured in this study is 1.78 % for calcium dihydrogen phosphate monohydrate ($Ca(H_2PO_4)_2 \cdot H_2O$) this value is 1.78 times higher than the reported value in *Pupyshev et al*. using inductively coupled plasma discharge technique [128].

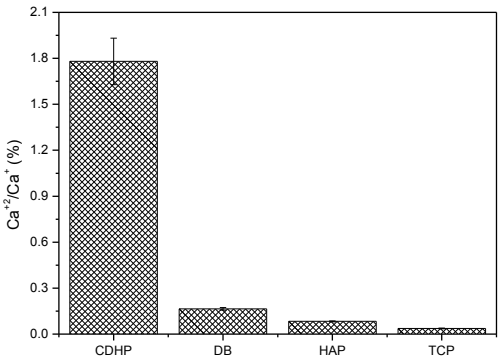

Figure 6.10. The relative ion yield of doubly charged ion (Ca^{+2}) for different synthetic calcium phosphates.

In the present study, we observed increase in the calcium containing polyatomic ion signals (especially $CaPO_2^+$) with the increase in the doubly charged calcium (Ca^{+2}) for different synthetic calcium phosphates, which became the basis of the new proposed method for the phase identification of different calcium phosphates [29]. Hence, the relative intensity of doubly charged calcium could be another candidate for the phase identification of calcium phosphates.

7. TOF-SIMS analysis of struvite stones

In this chapter, we will present the results of 13 struvite stones by comparing the results with that of reference chemicals where required. We found these stones as pure (more than ca. 95% struvite), mixture with urates, calcium phosphates, TCP and HAP. We proposed the phase identification of these phosphates by comparing with that of reference chemical mixtures. We also quantified their contents in struvite stones by using the relative sensitive factors (RSFs) calculated for the reference chemical mixtures. We did not find any struvite stone containing calcium oxalate as major or minor component. From the relative abundance found for Na^+ and K^+ in these stones. We found Na^+ association with calcium phosphate and that of K^+ with struvite; we also confirmed same associations of these elements in a single sample by using micro-analysis TOF-SIMS imaging mode.

7.1 Struvite stones

Struvite, another mineral entirely constituting some of the stones analyzed, it is a low stability mineral that is easily altered by volatile loss, mainly H_2O, but also N_2 [132]. Struvite may transform to newberyite as a result of NH_4 volatilization [133]. Heating struvite at temperatures as low as 50 °C can cause irreversible transformations. Struvite was first discovered by a Swedish geologist named Ulex in 1845 after studying bat guano. He named it after his friend and mentor, the nineteenth century Russian diplomat and naturalist Baron von Struve (1772–1851). Struvite, a crystalline substance, is composed of magnesium ammonium phosphate hexahydrate ($MgNH_4PO_4{\cdot}6H_2O$). Von Struve had published one of the earliest scholarly geological works in 1807 entitled “Mineralogical Memoirs”.

Struvite urinary stones have also been referred to as “infection stones” and “triple phosphate” stones. Early chemical analyses of these stones demonstrated the presence of calcium, magnesium, ammonium, and phosphate, a total of three cations and one anion. Carbonate ions

were also commonly identified; they were assumed to be associated with calcium as calcium carbonate ($CaCO_3$). Other terms for these calculi include magnesium ammonium phosphate ($MgNH_4PO_4 \cdot 6H_2O$), calcium carbophosphate, carbonate apatite $Ca_{10}(PO_4)_6(OH,CO_3)$, and urease —an enzyme that catalyzes the hydrolysis of urea into carbon dioxide and ammonia due to presence of urea splitting bacteria. Modern crystallographic analyses have shown that human "struvite" stones are a mixture of struvite ($MgNH_4PO_4 \cdot 6H_2O$) and carbonate-apatite $Ca_{10}(PO_4)_6(OH,CO_3)$. In some stones, struvite may be more abundant, whereas in other stones apatite may predominate. Evidence links the formation of struvite and carbonate-apatite stones to urinary infection.

Struvite often forms with apatite mixed stones in the form of big staghorn stones. The color is mostly white to light gray. In most cases, they have a loose consistency. Struvite stones are easily recognizable due to their large size and coral form. Despite their porosity, these stones were among the heaviest samples (average weight 155mg) [129].

The results of 13 stones listed in Table 7.1 will be presented in this chapter. The samples were prepared on indium and aluminum substrates according to two sample preparation techniques discussed in chapter 3 for respective substrate.

Table 7.1. Experimental conditions and classification of stones identified as struvite

stone sample	presputtering with 3-5 $\times 10^{13}$ ions/cm^2	substrate used	Classification with TOF-SIMS
STRU1	*	Indium	Struvite + **TCP**
STRU2a	Yes	Indium	Struvite + iodine
STRU2b	*	Indium	Struvite + urates
STRU3W	Yes	Indium	Struvite +**TCP**
STRU3B	Yes	Indium	Struvite +HAP
STRU4	Yes	Al	Struvite + HAP
STRU5	Yes	Indium	Struvite + HAP
STRU6	Yes	Al	Struvite (core)+ K urate (shell)
STRU7	Yes	Indium	Struvite + HAP
STRU8	Yes	Indium	Struvite+ **TCP**
STRU9	Yes	Indium	Struvite +HAP
ǂSTRU10	Yes	Al	Struvite + HAP
STRU11	Yes	Indium	Struvite + HAP
STRU12	Yes	Al	Struvite + HAP
STRU13	Yes	Indium	Struvite

Star (*) indicated that spectra shown in Figures 7.3 and 7.5b were acquired without presputtering while used for quantification in Table 7.3 were acquired after presputtering. The symbol (ǂ) indicates dog stone.

The presputtering ion dose of ca. 3-5 $\times 10^{13}$ ions/cm^2 was used for the mass spectra used for the quantification to remove the trace amount of hydrocarbons present on the surface and to stimulate the ion emission of inorganic components. For each sample we also acquired mass spectra without presputtering to confirm the presence/absence of any organic component in stone composition. Potassium and sodium urate components were identified more often in struvite stones.

7.2 TOF-SIMS analysis of Struvite stones

We analyzed pure struvite stones as shown in Figure 7.1, were having very well defined shape and color from transparent to white. The white color especially of stone surface is due to surface dehydration even at room temperature. We found these stones with high degassing when moved in UHV for analysis that is believed due to 49% volatile composition comprising 6 water molecules and an ammonia in stoichiometric molecular formula.

Figure 7.1: The visual appearance of struvite stones (STRU1).

The TOF-SIMS negative ion spectrum of this stone along with reference struvite is shown in Figure 7.2. The typical ions observed for the stone (STRU1) and reference struvite are the same that were also observed for calcium phosphates which are P^-, PO^-, PO_2^-, and PO_3^- at the respective m/z of 31, 47, 63, and 79 respectively. The relative abundance (%) of these species (Table 7.2) are quite similar for the stone and reference struvite but quite different when compared with calcium phosphates e.g. HAP. It is quite easy to confirm the presence of phosphate through negative ion spectrum but it does not give any information about the electropositive species present in the specimen.

Table 7.2: relative abundance (%) of phosphate ions for reference chemicals and real stone samples.				
Ion species	stone(STRU1)	reference struvite	reference HAP	HAP stone(S11)
P-	1.21	0.37	3.82	6.66
PO-	1.97	0.73	5.91	5.41
PO2-	52.89	57.96	75.18	62.91
PO3-	43.91	40.93	15.07	24.99

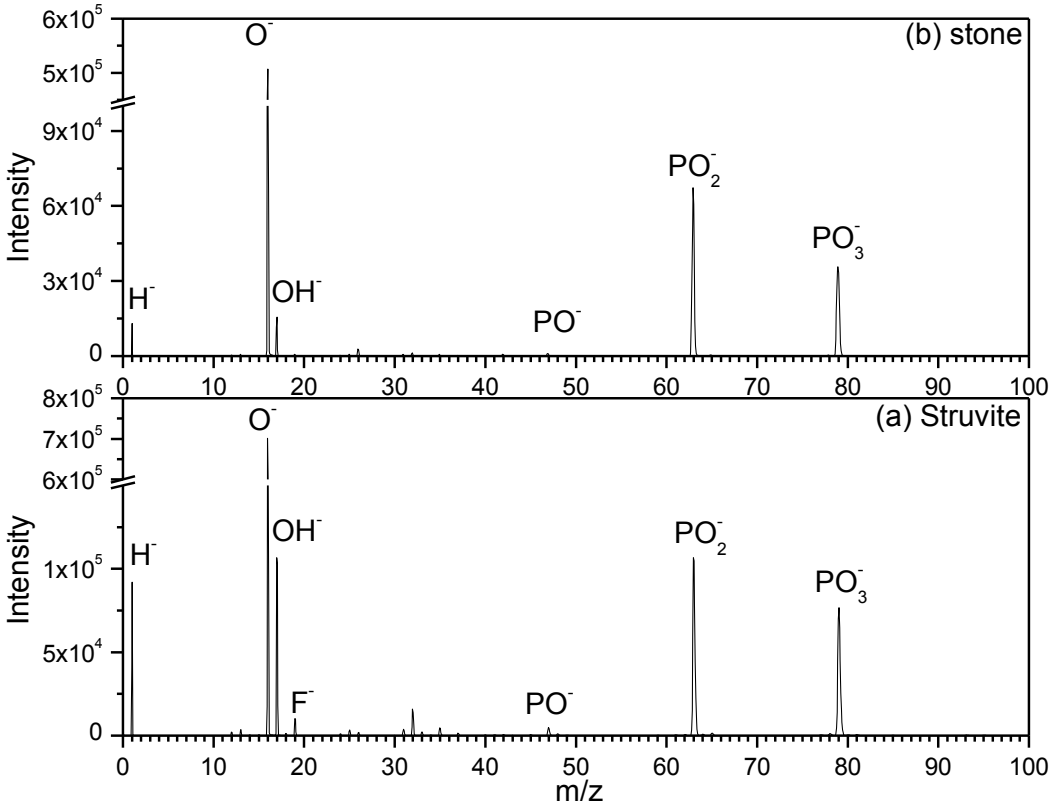

Figure 7.2. Negative TOF-SIMS spectra of reference struvite (a) and of renal stone (STRU1) (b) shown in Figure 7.1.

The positive ion TOF-SIMS spectra of the stone and reference sample are shown in Figure 7.3. The characteristic ions observed for the stone and sample are NH^+, NH_3^+, and NH_4^+ at m/z 15, 17,and 18 respectively, corresponding to ammonia present in the stoichiometric formula. The presence of magnesium is obvious form its elemental ion peaks of Mg^+ at m/z 24/25/26 and interfering hydrated ion of MgH^+ at m/z 25/26/27, water and phosphate associated ions of $MgOH^+$ and $MgPO_2^+$ are also observed at m/z 41and 87, respectively. The ion peak of $MgPO_2^+$ is not very clear due to interfering organic peaks, we clearly observed it in the mass spectrum acquired after presputtering (not shown here) which we will see later in this chapter in other sample. In the stone sample we observed potassium K^+ (14.6% of $^{24}Mg^+$ in Ga^+ sputtered spectrum) interference signal with $C_3H_3^+$ at m/z 39 relatively larger than sodium intensity signal of Na^+ (2.1% of $^{24}Mg^+$ in Ga^+ sputtered spectrum) at m/z 23. It is interesting to note here that we did not observed

potassium greater than sodium in calcium oxalate, calcium phosphates and of their admixed compositional stones. We also observed calcium phosphate ion peaks in the stone sample and confirmed their presence in Ga^+ sputtered spectrum (not shown) but the amount of this component is less than 1%. The quantification of Calcium phosphate (CaP) in admixed struvite will be discussed later.

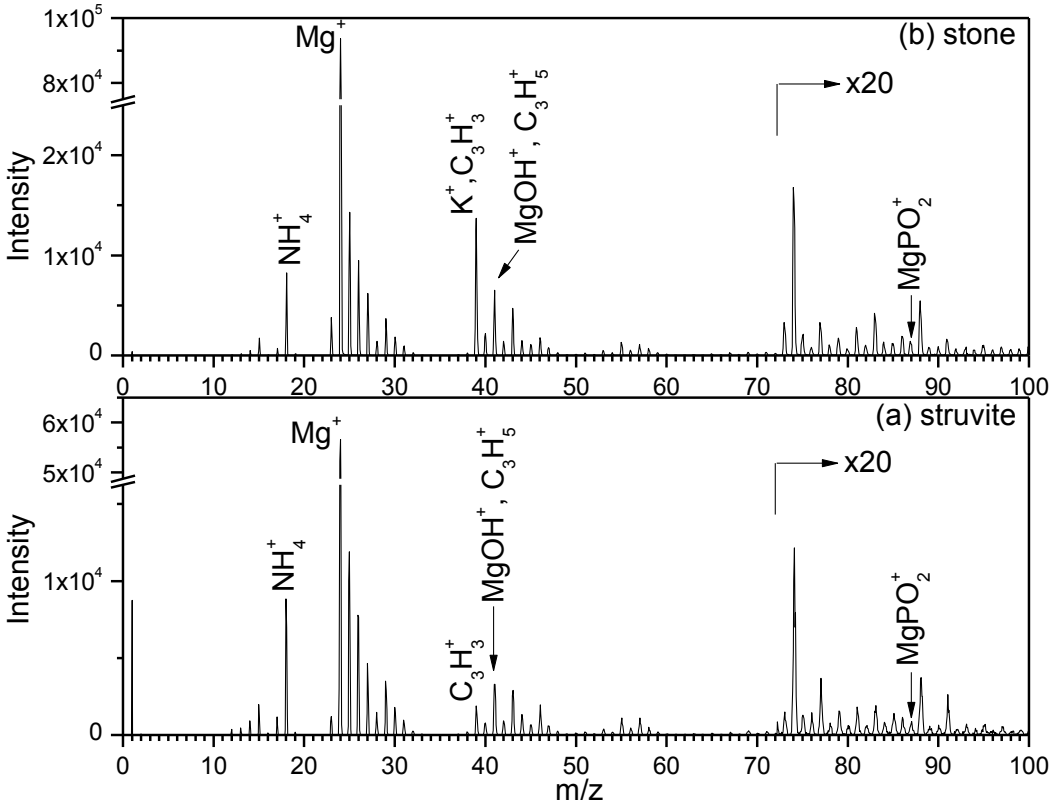

Figure7.3: Positive TOF-SIMS spectra of reference struvite (a) and of renal stone (STRU1) (b) shown in Figure 7.1

7.3 TOF-SIMS analysis of struvite stones mixed with urates

In our study, we found struvite containing stones, mixed with other urinary components such as calcium phosphate and uric acid. we also observed potassium and sodium urates in struvite stones. Here we will present the chemical analysis of two stones (STRU2a and STRU2b) belonging to a three-year-old patient hospitalized with a diagnosis of nephro- and bladder lithiasis. This patient underwent two surgical procedures: the removal of the right kidney and ureter, and the removal of stones from the bladder. However, one stone (STRU2a) was spontaneously expelled; it was ca. 6mm × 4mm in size, soft, with a rough surface of yellow color. Other stone (STRU2b) was removed by surgery in second episode; it was larger than the previous one (ca. 12mm × 10mm) but exhibited the similar visual characteristics.

Figure 7.4 shows the negative TOF-SIMS spectra of these renal stones. The main ions that were detected in the reference chemical, shown in Figure 7.2a (PO_n^-, where n=0-3), were also observed for these stones (Figures 7.4a and 7.4b), additionally CN^- and CNO^- ions were also present. For STRU2a, the presence of low intensity I^- and I_2^- ions (Figure 7.4(a)) is related to the medical history of the patient. These ions are not characteristic for kidney calculi and they were not detected for the other samples. This patient had actually undergone X-ray examination before surgery to remove the kidney stone and iodine staining had been used for enhanced visualization of the stone.

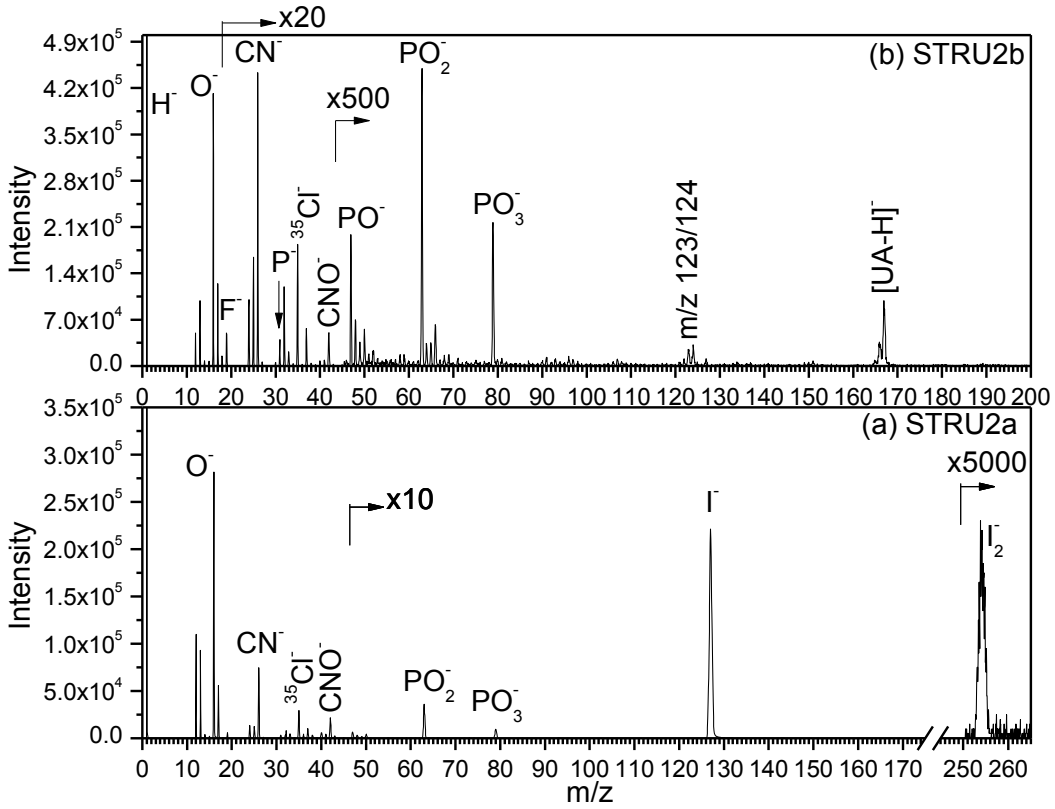

Figure 7.4. Negative ion spectra of STRU2a (a) and STRU2b (b)

For STRU2b, in addition to the CN^- and CNO^- ions, the deprotonated uric acid molecule at m/z 167 and the corresponding fragment ion at m/z 124 $[M–H–HCNO]^-$ were also detected (Figure 7.4(b)). These ions confirmed the presence of uric acid in the sample. For STRU2a, however, the recognition of uric acid just by the presence of CN^- and CNO^- ions is ambiguous.

The positive ion spectra of these stones shown in Figures 7.5 and 7.6 help to elucidate this point. The presence of Mg^+ at m/z 24 along with the phosphate ions detected in the negative ion mode (Figure 7.4) indicates that the kidney stones are mainly composed of struvite. For STRU2a (Figure 5a), the dominant peak in the low mass range is Na^+, mainly resulting from the iodine staining compound. For both kidney stones the ions at m/z 40, 56 and 57 correspond to Ca^+, CaO^+ and $CaOH^+$, which originated from calcium phosphate although it is only a minor component. The

ion peaks at m/z 169, 184 and 191 assigned to $C_5H_4N_4O_3H^+$, $NH_2C_5H_4N_4O_3^+$ and $NaC_5H_4N_4O_3^+$ ions, respectively, confirm the presence of uric acid in STRU2b. For this sample the presence of KH_2PO_4 resulted in peaks at m/z 39, 104 and 120, which are K^+, $KH_2PO_2^+$ and $KH_2PO_3^+$, respectively. This compound is not a kidney calculi component but it is an antiurolithic agent used as urinary acidifier. This component is unique for this stone; we have not detected its presence in any other stone analyzed in the present study.

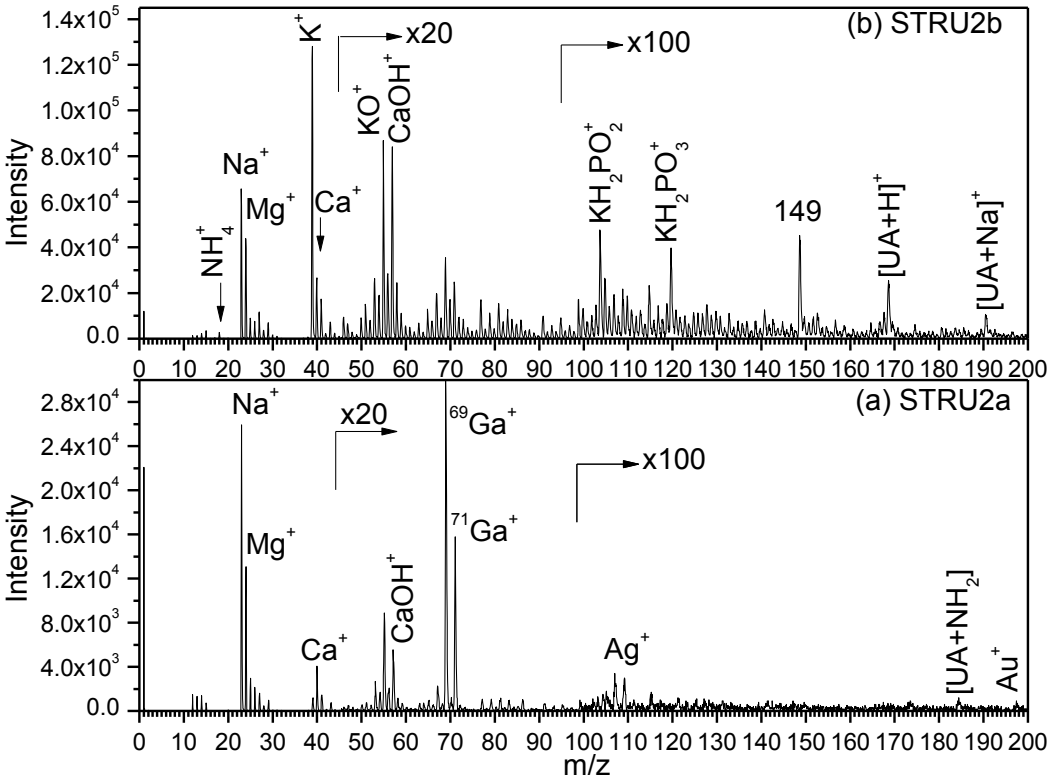

Figure 7.5. Positive ion spectra of STRU2a (a) and STRU2b (re-analyzed) (b)[26].

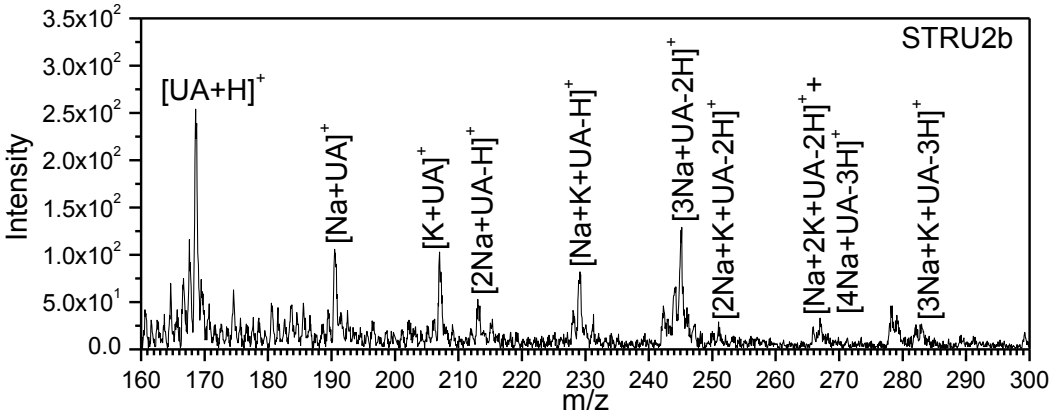

Figure 7.6: continuation of Figure 7.5b.

We also observed the sodium and potassium urate characteristic peaks (Figure 7.6) in the STRU2b proposed at m/z 207, 213, 229, 245, 251, 267 and 283 corresponding to $[K+UA]^+$,

$[2Na+UA-H]^+$, $[Na+K+UA-H]^+$, $[3Na+UA-2H]^+$, $[2Na+K+UA-2H]^+$, $[Na+2K+UA-2H]^+$+ $[4Na+UA-3H]^+$, and $[3Na+K+UA-3H]^+$, respectively.[27, 96], The intensities of these peaks are smaller than the uric acid protonated molecules $[UA+H]^+$ at m/z 169, while vice versa in the reported studies, which confirm the presence of uric acid along with its urates.

7.4 TOF-SIMS analysis of struvite stone containing calcium phosphate

We have already discussed that struvite is identified from the presence of NH_4 ion at m/z 18, Mg, and presence of P^+, PO^+, POH^+ ion in the positive spectrum, but it might be difficult to say about the calcium phosphate in the mixture with struvite just from the elemental Ca+ ion peak at m/z 40. This ion could be from the calcium phosphate or calcium oxalate. We did systematic study on admixed struvite with calcium oxalate and calcium phosphates reference chemicals. This study will also be helpful to clearly identify which component it is and semi-quantitative idea of its contents.

As negative mass spectrum will not be too much informative except to confirm the phosphate's presence which might be due to struvite, calcium phosphate, or due to presence of both components. However, positive spectrum is much informative and could be used to identify both components.

Here we will present the results of a stone (STRU3) in which we found tri-calcium phosphate, hydroxyapatite and struvite in the in a single stone shown in Figure 7.7. Quantification was also achieved and revealed it as struvite (>98%) with major component. The two positive ion spectra (Figure8) from the stone shown in Figure 7 are representative of white and brown parts of stone. The spectra shown were acquired under same experimental conditions after short Ga^+ sputtering with similar dosage.

Figure 7.7: stone STRU3 showing layers of struvite (white slab) with calcium phosphate (brown) developed on it top.

In the spectrum obtained from the white part of the STRU3, shown in Figure 7.8a, the major ion peak were observed at m/z 24, 31, 47, 48 and 87 are identified as Mg^+, P^+, PO^+ ,POH^+, and $MgPO_2^+$ along with the presence of their isotopic ions. We also observed the NH^+, NH_3^+, and the more intense peak of NH_4^+ in the spectrum acquired without any pre-sputtering corresponding to ammonium which is stoichiometric component of struvite. Hence, these results, without any doubt show the presence of struvite.

Presence of calcium phosphate was confirmed from the ion peaks of Ca^+, CaO^+, $CaOH^+$, Ca_2O^+, $CaPO_2^+$, and $Ca_2O_2H^+$. From the peak ratio $CaPO_2^+/Ca_2O^+$ (1.96), and the ratio $CaOH^+/CaO^+$ (1.5) we identified it as tri-calcium phosphate, amounting 1.05%. The quantification was achieved by using the relative sensitivity factor RSF (Ca^+/Mg^+) obtained for the reference mixture of struvite and TCP corresponding to relative atomic concentration of 0.237 for Ca/Mg in the resulting mixture (Table 7.3).

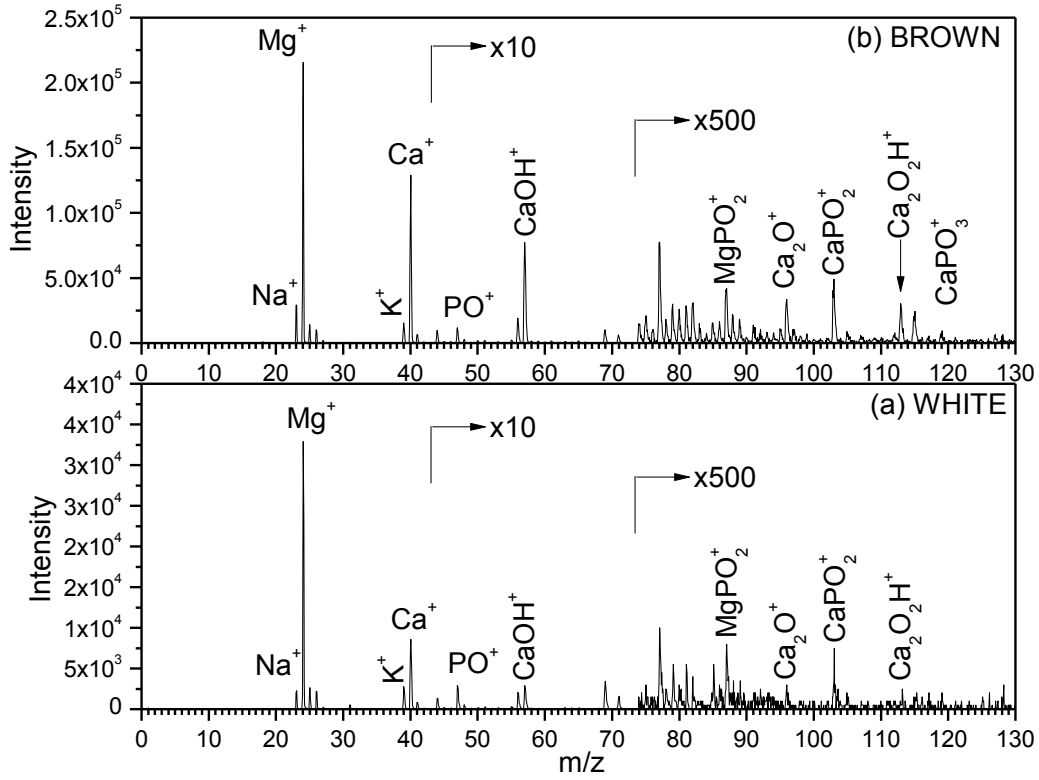

Figure 7.8: The positive ions spectra from the stone STRU3 corresponding to (a) white and (b) brown parts.

Similar ion peaks were observed for the brown part of the stone STRU3 as shown in Figure 7.8b; visually this part is quite different. The presence of struvite and calcium phosphate is obvious from the similarity of the two spectra, but the relative abundances of calcium phosphate peaks are quite different, although $Ca^{+/}Mg^+$ ratio has not great difference. The ratio $CaPO_2^+/Ca_2O^+$ (1.44) smaller than 1.96 (identified as TCP) and the $CaOH^+/CaO^+$ (4.6) is 3 times bigger than 1.5

corresponding to spectrum from white part. The higher ratio of $CaOH^+/CaO^+$ gives the presence of OH group in the calcium phosphate which is only characteristic of hydroxyapatite. Furthermore, lower value of ratio $CaPO_2^+/Ca_2O^+$ compared to TCP is due to low PO_4/Ca ratio in the stoichiometric formula of hydroxyapatite. Hence, brown part of the stone was composed of struvite and HAP with molecular stoichiometric contents of 96.83% and 3.17%, respectively. The presence of two phases of calcium phosphate, although in trace amount indicate the change in physiological conditions during the stone development. We observed higher signal intensity of sodium (8.31% of Ca^+Mg) in sample with HAP compared to 5.12% in the TCP containing sample. The potassium signals were 9.52% and 8.71% in respective samples. In our previous study we reported sodium in the range of 5-20% while potassium signal was 0-4.5% of principal ion peak of calcium for binary stones of calcium oxalate and HAP [29].

Here for the present sample, we confirmed the absence of calcium oxalate and brushite on the basis of ratio $CaPO_2^+/Ca_2O^+$ using new method of phase identification and quantification proposed for calcium phosphates in struvite samples which will be discussed in following section.

7.5 Phase identification of calcium phosphate in struvite

The positive TOF-SIMS spectrum of a mixture containing reference synthetic chemicals of calcium oxalate and struvite in equal weight proportions (resulting $Mg_{0.37}Ca_{0.63}$ concentration) is shown in Figure 7.9a. The main ions of both components are present with negligible adduct ion signal of $CaPO_2^+$ (m/z 103), so in case of binary stone of calcium oxalate/struvite we expect peak ratio of $CaPO_2^+/Ca_2O^+$ close to zero. But in the present study author always found the ratio $CaPO_2^+/Ca_2O^+$ greater than unity for the stones with presence of struvite component. From these facts, we can conclude that struvite stones are not developed with calcium oxalate as major or minor component, however, exceptions are always present. The presence of $CaPO_2^+$ peak could then only be due to presence of calcium phosphates i.e. brushite, HAP, and TCP etc.

The positive spectrum from the reference chemical mixture of $CaHPO_4$ (dehydrated brushite) and struvite is shown in Figure 7.9b, with the presence of all calcium/magnesium elemental and polyatomic ion peaks for both admixed components discussed before, and are indicated in the spectrum. The presence of struvite is obvious from the Mg^+, $MgPO_2^+$, and very small peak of NH_4^+ (m/z 18), the low signal of later peak is due to Ga^+ sputtering used before the spectral acquisition. The polyatomic calcium phosphate ion peak of $CaPO_2^+$ is apparent with really good intensity as compared to Ca_2O^+, the ratio $CaPO_2^{+/}$ Ca_2O^+ (4.93) obtained from this spectrum is very close to literature value of 5.14 for reference $CaHPO_4$ [29]. We revealed from these results that the phase identification of $CaHPO_4$ remains conserved even it is present in the

mixture with struvite. Again it might be interesting to mention that we did not found the ratio of $CaPO_2^+$/ Ca_2O^+ greater than 2.25 for real samples (STRU1-STRU12). We always found this value from 1.0-2.25 which is obvious in Table 7.3, giving brushite occurrence frequency of 0 in struvite stones.

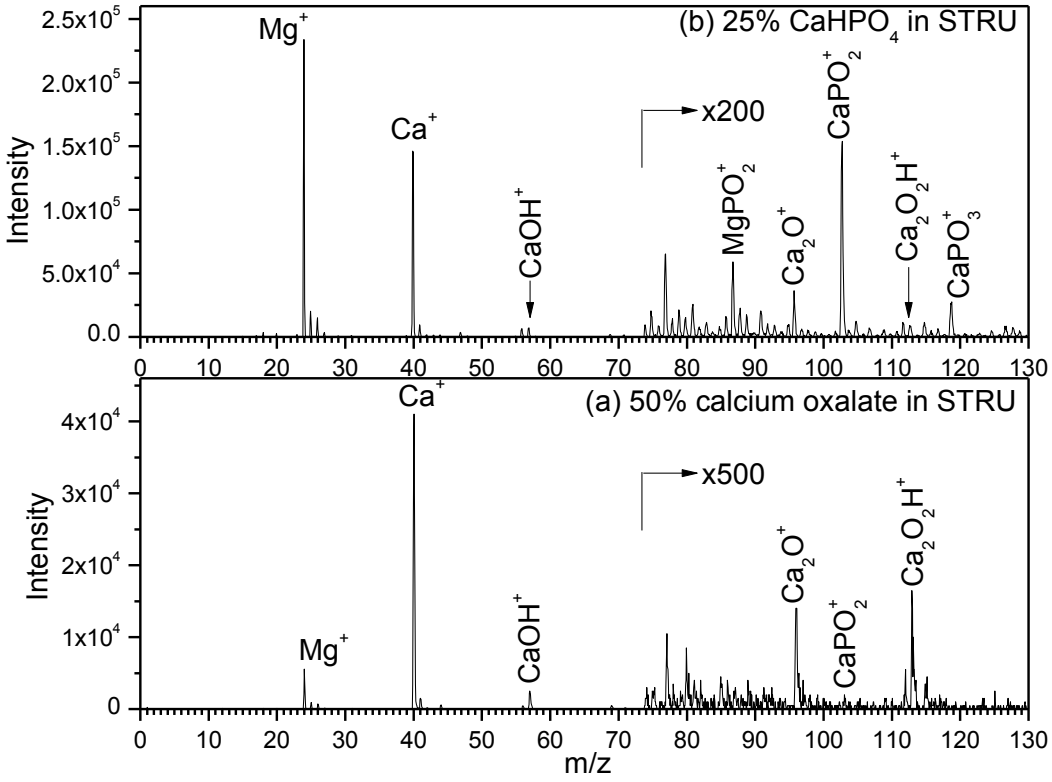

Figure 7.9: The positive SIMS spectra of (a) struvite (50%) and calcium oxalate (50%), and (b) struvite (75%) and monetite (dehydrated brushite) (25%).

The presence of HAP in struvite stones is well known from the literature and its identification with other techniques is frequently reported but the association of TCP with struvite is not often reported by other techniques. These two phases of CaPs are quite similar and a number of authors reported $Ca_3(PO_4)_2$ (TCP) as HAP. In our study, the stones giving $CaPO_2^+$/ Ca_2O^+ ratio from 1.0-1.5 we considered them as HAP with second component as struvite, while the stones giving this value from 1.5 to 2.25 are considered as TCP and struvite as shown in Table 7.3.

The enhancement in the ratio $CaPO_2^+/Ca_2O^+$ (2.01) is observed for the mixture as compared to 1.13 for the reported reference TCP powder. This $CaPO_2^+$ signal enhancement is not due to adduct ions (we already confirmed by mixing COX with struvite, discussed above) but can be attributed the enhancement to the relative increase in the doubly charged calcium Ca^{+2} compared to that of singly charged Ca^+ giving relative Ca^{+2}/Ca^+ abundance of 0.23% which is

6.29 time higher than the reported value of 0.04%, resulting an increase in the molecular ion peaks, in this case the intensity of $CaPO_2^+$ and hence the ratio $CaPO_2^+/Ca_2O^+$.

Table 7.3: Relative peak intensities of calcium phosphates (TCP and HAP) and their compositional contents in struvite stones.

sample	$CaPO_2^+/Ca_2O^+$	CaP	% CaP	$Na^+/(Ca^+ + Mg^+)$	$K^+/(Ca^+ + Mg^+)$	PO^+/POH^+
STRU1	2.00	TCP	0.20	3.76	10.41	5.47
STRU2b	1.07	HAP	5.69	42.98	265.22	1.50
STRU3W	1.96	TCP	1.05	4.42	8.032	6.05
STRU3B	1.29	HAP	3.17	7.36	5.44	4.26
STRU4	1.00	HAP	14.25	33.14	19.14	1.25
STRU5	1.04	HAP	23.76	25.16	6.25	1.51
STRU6	1.39	HAP	14.92	51.26	122.69	1.43
STRU7	1.15	HAP	38.86	76.64	2.17	1.04
STRU8	2.25	TCP	0.21	11.93	27.18	5.70
STRU9	1.10	HAP	3.71	11.42	8.90	3.24
STRU10	1.40	HAP	6.95	45.30	53.55	3.61
STRU11	1.05	HAP	84.89	6.66	1.53	1.19
STRU12	1.22	HAP	31.21	24.56	4.56	1.39
STRU13	--	--	N/A	3.03	35.96	5.17
TCP 7.3%	2.01	TCP	7.32	0.85	0.83	2.60
HAP 33%	1.25	HAP	32.32	0.67	0.28	0.89

Note: the values given in the table are based on the calculations from single spectrum data of each sample acquired with similar experimental conditions.

Similar increase is expected for HAP in struvite mixture and hence the ratio $CaPO_2^+/Ca_2O^+$ (0.70) for the reference chemical because of the matrix effect. The average value of Ca^{+2}/Ca+ (0.36%) observed for the stones characterized as HAP mixture (STRU2b, STRU3B, STRU4-STRU7, STRU9-STRU12) is 4.34 times higher than that of reference HAP of 0.083% reported in *Ghumman et.al*. [29]. For these samples, we also decreased the Ga^+ pre-sputtering dosage to ½ of the dose we generally used in our previous study, this decrease improved the molecular ion yield and hence to differentiate very close stoichiometric calcium phosphates with PO_4/Ca of 0.6 and 0.67 corresponding to HAP and TCP respectively. These two calcium phosphates are indistinguishable from each other through the ratio $CaPO_2^+/Ca_2O^+$, if TCP is relatively more pre-sputtered, resulting decrease in the PO_4/Ca close to 0.6 which corresponds to of HAP due to higher preferential sputtering rate of phosphorous as compared to calcium.

The 12 stones (STRU1-STRU13 excluding STRU10 dog stone) out of total 36 stones lie in the category of calcium phosphates and struvite with occurrence frequency of 33% (sample

collection was not random). The phase identification of calcium phosphates were carried out by the method proposed above. We found TCP component in 3 stones (occurrence frequency of 25%) and HAP in 10 stones (75%) including one stone (STRU3) in which both components were identified as given in the Table 7.3. We also found struvite with sodium urate, potassium urate and ammonium urate resulting total struvite component occurrence frequency of ca. 35%.

If we look at the stone (STRU3) shown in Figure 7.7, dissimilarity is obvious in the two parts (white and brown). This is point of scientific curiosity ―the amount of calcium phosphate present in the two parts. Does the brown part contain HAP as major component? Answer is no as we see in the Table 7.3 it is only 3.17% relative to 96.83% of struvite. Although, SIMS is not truly quantitative but we answered the above question, as well as deduced some important findings relating to the matrix effect, association of Na^+ and K^+ with HAP and struvite components respectively.

7.6 Relative sensitivity factor and quantification of calcium phosphate in struvite

It is well known that quantification in SIMS cannot be performed directly from the signal intensities of the ions of interest. The same concentration of different elements present in a sample may not give similar signals but differing in order of magnitude [36], depending on the nature of elements to be analyzed (ion yield), the chemical composition of the matrix (matrix effects), the nature of primary ions, and instrumental parameters (current density, pre-sputtering, transmission of mass spectrometer, detector efficiency, etc). Such quantification problems are usually overcome using by measuring the relative sensitivity factors (RSFs) of the elements in similar matrix. This is defined [134] by

$$RSF_{A/B} = (I_A/I_B) / (C_A/C_B) \quad (7.1)$$

Where ´*I*´ is the experimental secondary ion intensity, *C* is the atomic concentration of element A and that of B present in the sample.

As a matter of subject, we are interested in the measurement of RSF for Ca relative to Mg; these are the two principal elements of calcium phosphate and struvite, respectively. Mass spectra were obtained for the binary mixture of the reference chemicals of struvite with cacium oxalate, monetite ($CaHPO_4$), TCP ($Ca_3(PO_4)_2$) and HAP. The relative atomic concentrations of C_{Ca}/C_{Mg} in these mixtures were 1.679, 0.601, 1.804, 0.237, 2.373, and 2.442 as shown in Table 7.4. We measured RSF (Ca^+/Mg^+) for these 6 reference matrixes using C_{Ca}/C_{Mg} values in eq. (7.1) along with the experimental accumulative intensities of Ca^+ and Mg^+, values are given in the

Table 7.4. We observed surprising big change in the RSF value (9.52±11.57, *mean* ± *standard deviation*) for CaHPO4 (monetite) mixtures at two different concentrations while for TCP mixture the RSF value (10.77±0.09) of Ca^{+}/Mg^{+} is independent of the relative concentration which is obvious from the low *standard deviation* value, similar low *standard deviation* is expected for HAP because of close resemblance with TCP.

Table 7.4. Relative sensitivity factors (RSF) of Ca^{+} and Ca^{+2} relative to Mg+ for produced mixtures of known composition.

Matrix (assay composition %)	atomic ratio (Ca/Mg)	RSF(Ca^{+2}/Mg^{+})	RSF(Ca^{+}/Mg^{+})
Struvite and COX (50, 50%)	1.679	0.00825	6.939
Struvite and monetite (25, 50%)	0.601	0.01170	1.336
Struvite and monetite (50, 50%)	1.804	0.07406	17.709
Struvite and TCP(90, 10%)	0.237	0.02526	10.843
Struvite and TCP (50, 50%)	2.373	0.04536	10.707
Struvite and HAP (50%, 50%)	2.442	0.01171	4.316
$Ca_3(PO_4)_2$	37.79	0.00697	1.596
$Ca(H_2PO_4)_2.H_2O$	45.83	0.01807	1.014

The lowest RSF found for Ca/Mg concentration of 0.601 in $CaHPO_4$ mixture gives maximum $Ca^{+}{}_2/Ca^{+}$ (0.87%) resulting maximum molecular ions with other electronegative species present in mixture suppressing the sensitivity of elemental calcium ion signal. We confirmed this fact by taking the sum of molecular peaks of CaO^{+}, $CaOH^{+}$, $Ca_2{}^{+}$, Ca_2O^{+}, and $CaPO_2{}^{+}$ for the two compositions, the calculated total abundance of these peaks relative to elemental Ca^{+} intensity are 9.8% (0.601, Ca/Mg) and 3.4% (1.804, Ca/Mg).

In addition to above 6 struvite mixtures we also considered reference calcium phosphates with known Mg impurities in TCP ($Ca_3(PO4)_2$, PRC) and calcium di-hydrogen phosphate monohydrate (Panreac), we found RSFs (Ca^{+}/Mg^{+}) of 1.596 and 1.014 respectively. Again here we can attribute low RSF value of 1.014 for calcium dihydrogen phosphate compared to 1.596 for TCP to relative abundance of 1.78% and 0.43% for doubly charged calcium Ca^{+2}/Ca^{+}.

In conclusion matrix effect on Relative sensitivity factor was clearly observed for Ca^{+}, Ca^{+2} relative to Mg^{+} in calcium phosphate and struvite mixture as well as in reference calcium phosphates with known impurity concentrations of magnesium.

As in our study we clearly identified the phase of calcium phosphate as TCP and HAP, so we used the RSF value of 10.77 measured for two ´ TCP/struvite mixtures´ for quantification of TCP and 4.316 for HAP in the real samples using the following rearranged equation (7.2) in combination with eq. (7.3) as follows

$$C_{Ca} / C_{Mg} = (I_{Ca}^{+}/I_{Mg}^{+}) / RSF_{Ca}^{+}{}_{/Mg}^{+} \quad (7.2)$$

$$C_{Ca} + C_{Mg} = 1 \quad (7.3)$$

Where, 'I_{Ca}^{+}' and 'I_{Mg}^{+}' are the experimental secondary ion intensities of calcium and magnesium, and 'C_{Ca}' and 'C_{Mg}' are the atomic concentrations of calcium and magnesium. The atomic concentrations were then converted to % assay composition by dividing the calcium atomic composition by 3 for TCP and with 5 for HAP. We obtained these compositions from 0.20% to 20.19% for the two phosphates as shown in Table 7.3.

The measured compositions of calcium phosphate especially for HAP in different stones strongly correlate with the peak ratios of PO+/POH+ shown in Table 7.3. This ratio decreases as the amount of calcium phosphate (HAP) increases and vice versa in struvite as shown in Figure 7.10, reference struvite gives maximum ratio for these peaks. We proposed the decrease in the ratio for HAP because of polar interactions between OH^{-} and phosphate (P^{+5}), giving the ion signal of POH^{+} more intense compared to TCP, hence resulting decrease is observed. On the other hand TCP do not contains hydroxyl (OH) group, so theoretically POH^{+} is not expected, although experimentally these ions were observed due to water/hydrogen adsorbed contaminations and resulting less decrease in PO^{+}/POH^{+} for TCP in struvite observed as shown in Figure 7.10 for three stone samples. These ratios are within the standard error bar observed for the reference struvite giving this ratio 6.28± 0.98 (*mean± standard error*). The higher ratio of PO^{+}/POH^{+} in struvite compared to calcium phosphates gives week water/phosphate binding energy, hence easy outgassing of water at higher rate which we observed for struvite samples when transferred in UHV chamber.

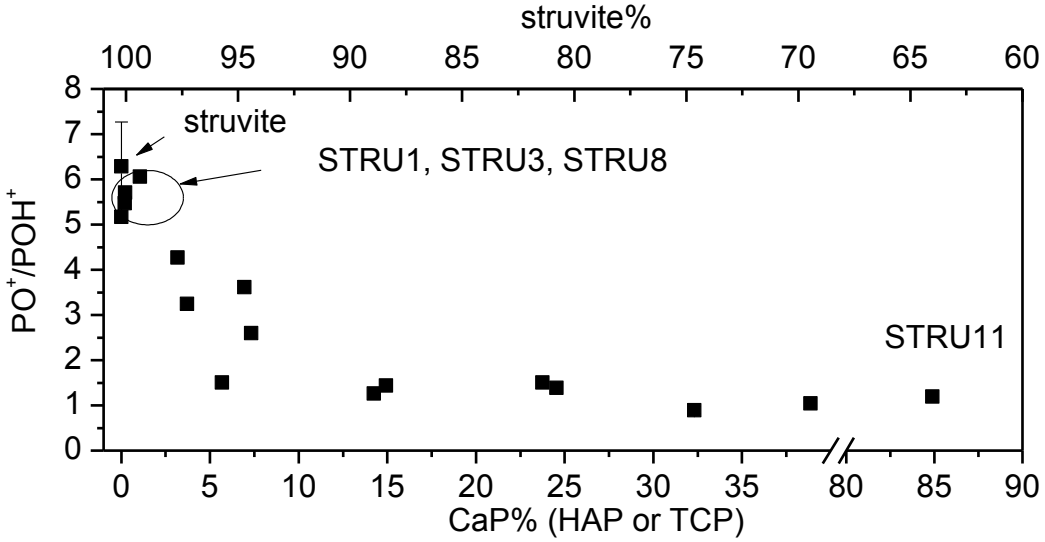

Figure 7.10: the ratios of PO^{+}/POH^{+} as function of calcium phosphate in struvite stones and that of reference struvite.

7.7 Sodium and potassium association with calcium phosphate and struvite components

In the urinary stone analysis the alkali metal like sodium and potassium are not addressed with most of the analysis techniques especially in association with calcium phosphate and struvite stones. Presence of these elements might give (relate) the physiological conditions under which stones are developed. In our study [29], we found up to 20% sodium contents in association with HAP as minor component in calcium oxalates stones while potassium was less than 4.5% of principal calcium ion (Ca^+) signal. Here in struvite stones we observed these contents up to 76.6% and 265.2 %, respectively as shown in Figure 7.11, calculations are based on eq. (7.4).

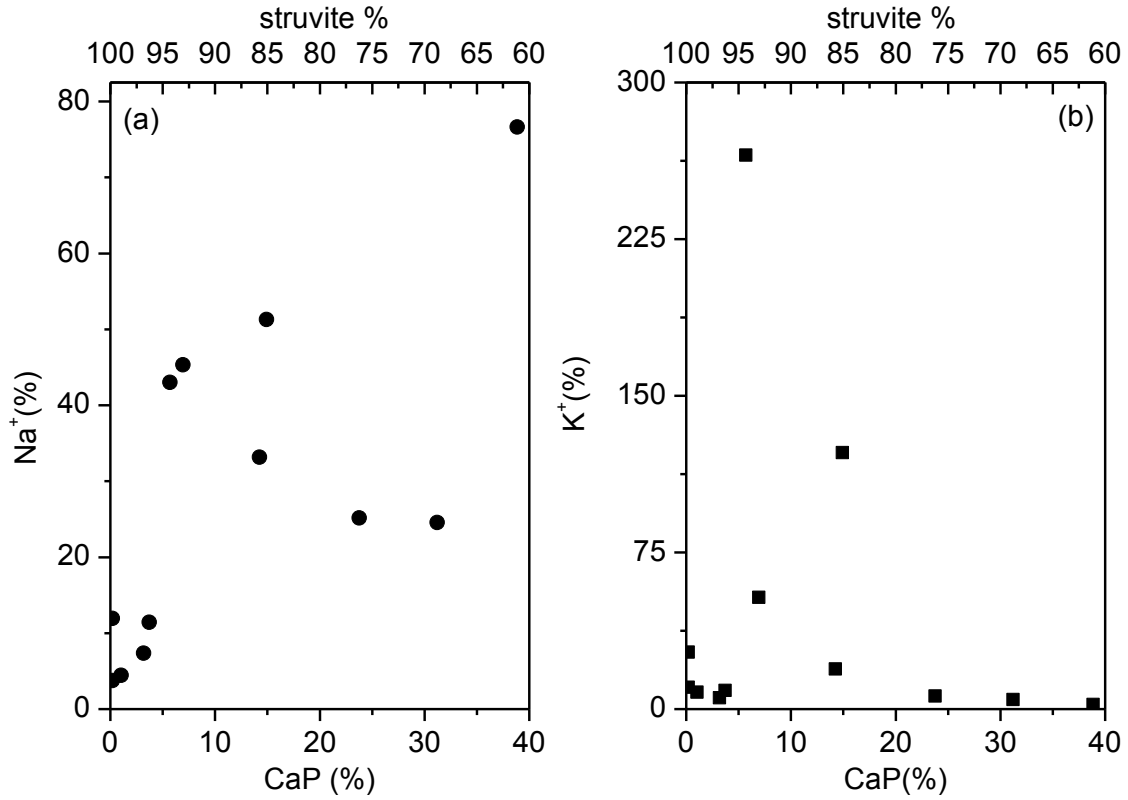

Figure 7.11. The relative abundance found for Na^+ (left) and K^+(right) in real stones at respective concentrations of calcium phosphate and struvite components.

$$i_m = (100 \times I_m) / (\sum(I_{Ca}{}^+, I_{Mg}{}^+) \quad (7.4)$$

Where ´*i*´ and ´*I*´ are the resulting % abundance and the experimental secondary ion intensities, the subscript ´m´ denoted Na^+ and K^+ in respective measurement. These intensities are plotted against the relative concentration of calcium and struvite components for the real stones (STRU1-STRU12) as shown in Figure 7.11. We observed increasing trend for Na^+ with increasing amount of calcium phosphate and vice versa for struvite component. While, for potassium we observed decrease in the K^+ with increasing amount of calcium phosphate and vice

versa for struvite component. From these results we concluded that sodium incorporation in the stones is mainly with calcium phosphates especially HAP, and potassium with struvite components.

These are the general findings from the statistical data. Now, question arises, do we observe this association within a single stone? Answer is yes, we observed this effect in single stone by using micro-analysis in TOF-SIMS imaging mode.

The TOF-SIMS imaging analysis was carried out on a sample from the brown part of the stone (STRU3) shown in Figure 7.7. The major ions observed were Na^+, Mg^+, K^+, and Ca^+, the identification of the stone has already discussed. Using the RSF ($Ca+/Mg^+$), quantification of these elements was achieved for each pixel. The image shown in Figure 7.12 is spatial atomic (relative %) distribution of calcium and magnesium calculated at each pixel from an area of 750×750 µm2 (128×128). The maximum calcium concentration of 55% (19.64% HAP) was observed. However, such high concentrations were observed only at few pixels, for majority of points this value was less than 7.5 % (ca. 1.5% HAP).

(a) 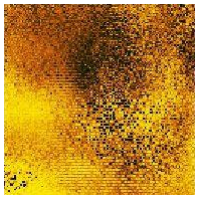 (b)  (c) 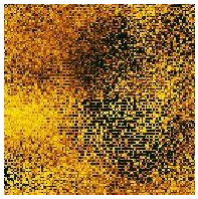 (d) 

Figure 7.12. Calcium spatial distribution (a), magnesium distribution (b), Na+(%) distribution (c), and K+(%) distribution (d).

The distribution of Na^+ and K^+ calculated using eq. (7.4) is also shown in Figure 7.12(c and d). As we predicted statistically the association of Na^+ with HAP and K^+ with struvite is obvious from these images. These relative abundances were plotted against the relative calcium, we confirmed similar increasing trend of Na^+ with increasing amount of calcium (Figure 7.13a), as that for statistically large number of stones (STRU1-STRU12) shown in Figure 7.11a. We also confirmed the decreasing amount of K^+ incorporation with increasing calcium concentration shown in Figure 7.13b and 7.11b and vice versa against the amount of struvite.

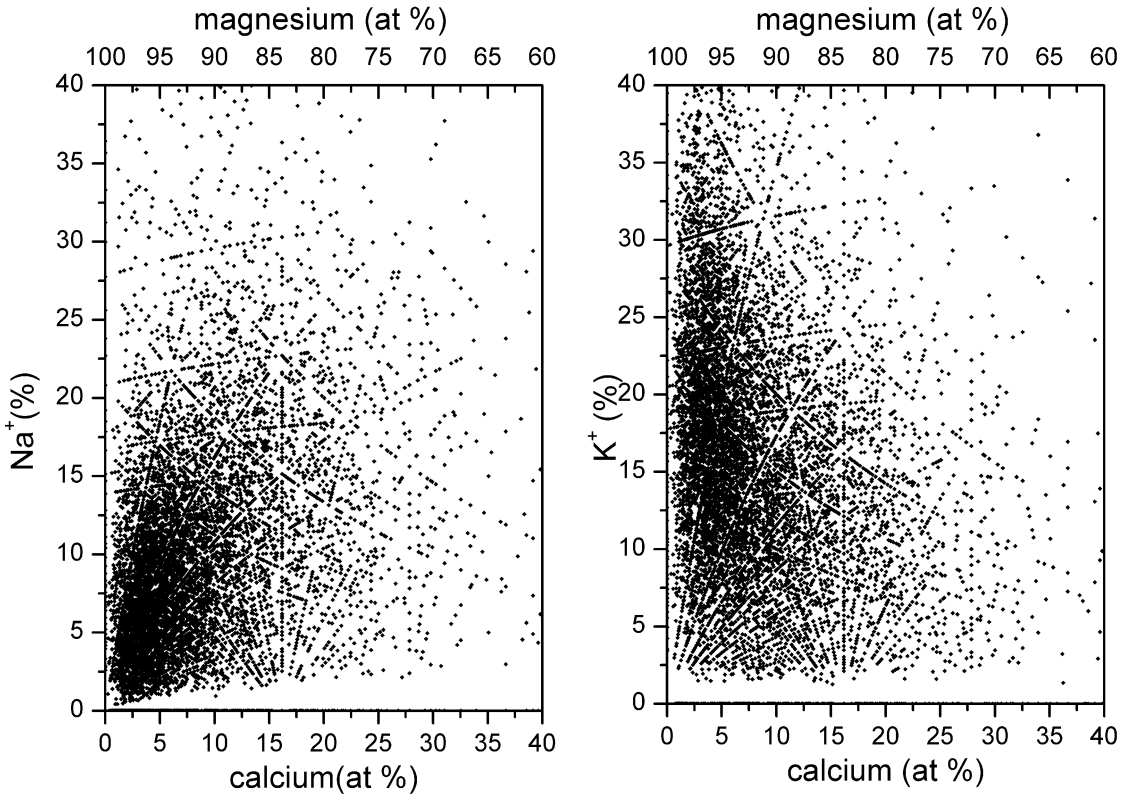

Figure 7.13: Relative intensities of % Na^+ (a), and % K^+ (b) observed at respective calcium concentration in the images shown in Figure 7.12.

8. CONCLUSIONS

A detailed experimental study on organic and inorganic calculi, especially human urinary stones was carried out using a TOF-SIMS VG Ionex IX23L upgraded by our surface science group (CeFITec, UNL). The goal was to examine the applicability of TOF-SIMS with our newly developed data acquisition and control system for systematic research.

Urinary calculi formation is a common illness distinguished by insoluble stones developing in the urinary tract. These stones are composed of many different compounds (e.g. uric acid, sodium/potassium urates, cystine, arginine, calcium oxalates, calcium phosphates, struvite) and are structurally distinct, but there is one common property among them that is the insolubility of the compound. Analysis of these stones is very significant because by knowing the true composition of calculus, a physician can effectively advise a patient to take preventive measures so that future similar occurrences can be avoided.

In the present study we analyzed 38 stones (36 stones from human including one gallstone and 2 stones from dog); the chemical compositions of 35 human urinary stones as major and minor components are listed in Table 1. The representative positive ion mass spectra of 5 main classes (uric acid (17%), cystine (2.8%), calcium oxalate (25.7%), hydroxyapatite (14.3%), and struvite (34.3%)) of urinary stones are shown in Figure 8.1. It should be noted that samples were not randomly selected.

This work clearly demonstrates the capability of TOF-SIMS to identify chemical composition of real urinary stones. The technique confidently indicates the presence of organic compounds in pure/mixed samples; for uric acid (mw 168), cystine (mw 240) and arginine (mw 174) all containing amino ($-NH_2$) group give deprotonated $[M-H]^-$ and protonated molecules $[M+H]^+$ of the respective component [26, 28] which are widely separated in a mass spectrum according to their molecular masses as shown in Figure 8.1. The presence of these components in

admixed stones with struvite or other organic component (e.g. presence of glycerol in uric acid stones) do not hamper on their identifications which is well known in FTIR analysis. These organic components are also readily identified in calcium oxalate and calcium phosphate stones in S-SIMS mode.

Using TOF-SIMS, we have identified cholesterol (containing OH group) gallstone through molecular ion peaks of $[M\text{-}OH]^+$ (cf. 2.1.3.7) representing its molecular structure. The present study also demonstrates the ability to distinguish cysteine from cystine, which is a common amino acid composed of two molecules of cysteine in oxidized form, although elemental composition of both are the same [28].

Sodium/potassium urates are readily identified from the uric acid by the presence of intense signals sodiated and potasiated uric acid molecules compared to protonated uric acid molecules [26, 27]. In the urate stones of an individual, incorporation of a vitamin B6 metabolite was also identified [27], demonstrating that TOF-SIMS in static mode is a reliable technique for the multi-component analysis of urinary stones with unknown components.

The calcium oxalate stones which are considered to be the most frequent urinary stones are successfully identified with state-of-art SIMS by the presence of elemental calcium ion peak (Ca^+), and the ion peak representative of water attachment with calcium in crystal structure at m/z 57 ($CaOH^+$). In one of the urinary stone we identified the presence of calcium formate, Ca(HCO2)2, which is used in the food industry as a food additive, denoted by E238. To the best of our knowledge this calcium oxalate phase has not been previously reported as being present in urinary calculus. We clearly identified Ca(HCO2)2 by the detection of protonated calcium formate in the positive secondary ion spectrum [27].

In our study we found calcium oxalate stones admixed with uric acid. We clearly identified the location of uric acid and calcium oxalate components in the binary stones of two individuals (cf. 5.1.2). These stones were developed as core and shell in one and vice versa in other, the layered growth might be representative of the change in the physiological condition occurred during the stone development. Uric acid was observed only in trace amount for the rest of calcium oxalate stones identified in the present study.

Calcium oxalate stones accounting for only 25.7% of total 35 stones as major component are often admixed with calcium phosphates; most of the ion peaks without phosphate component are common for calcium oxalate and calcium phosphates (e.g. Ca^+, CaO^+, $CaOH^+$). It might be interesting to state that in limited number of SIMS studies on calcium phosphates [32, 33, 35] authors had identified calcium phosphates only by these mentioned ions. In our extensive

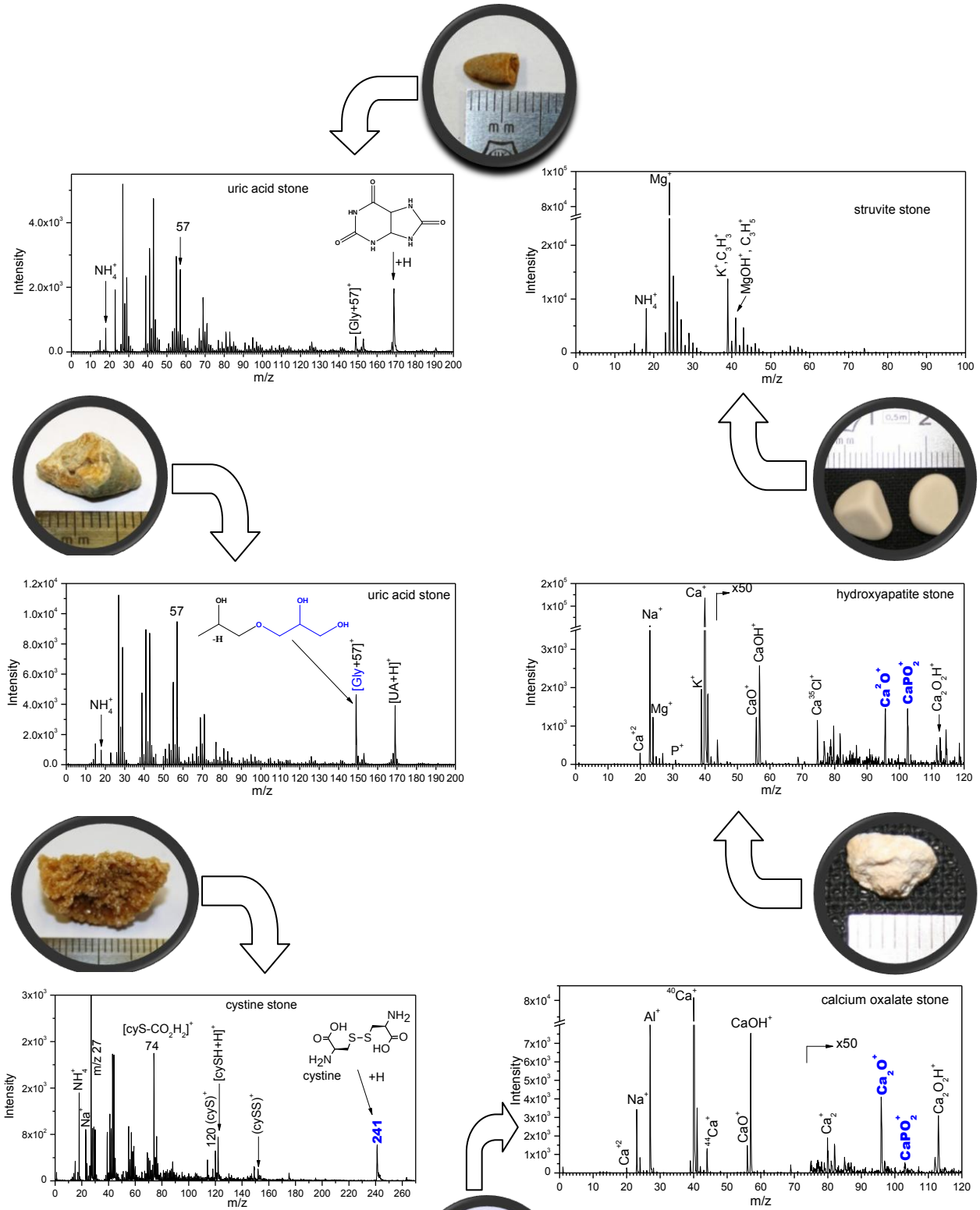

Figure 8.1a. The mass spectra of uric acid, uric acid containing glycerol, and cystine stones (top to bottom in respective order).

Figure 8.1b. The mass spectra of calcium oxalate, hydroxyapatite (containing 15% struvite), and struvite stones (from bottom to top in respective order)

experimental study we revealed that under pre-sputtering one can stimulate other ion species containing calcium and phosphate components (e.g. $CaPO_2^+$) present in the stoichiometric formulae which were used for the phase identification of calcium phosphates, to recognize the presence of calcium oxalate (fortunately no/negligible adduct $CaPO_2^+$ were observed) and for their quantifications [29].

Using our mentioned experimental findings, reliable phase identification of four biologically important calcium phosphates (Table 3.1 and cf. 6.2) was achieved in the positive TOF-SIMS mode on basis of the peak ratios of PO^+/POH^+ and $CaPO_2^+/Ca_2O^+$ by taking into account the major stoichiometric elements both electropositive and electronegative. The *standard deviation* of ca. 3.74 and 9.88 for the two ratios in our study is much better than the SD of ca. 0.8 achieved by *Lu et al*. [35] for the four biological important calcium phosphates. In natural urinary stones, pure calcium oxalate was distinguished from calcium phosphates with confidence via the presence of its characteristic ion peaks and, at the same time, with low-intense phosphate containing peaks (e.g. PO^+, $CaPO_2^+$ etc.). We also quantified the calcium phosphate as low as 3% in real human stones containing calcium oxalate as major or minor component. In these admixed calcium oxalate and calcium phosphate stones we found association of Na^+ with the presence of hydroxyapatite while K^+ and Mg^+ were negligibly small.

Struvite ($NH_4MgPO_4.6H_2O$) stones, also known as infection stones due to their association with urea-splitting bacteria were confidently identified by the presence of its major characteristic peaks of NH_4^+, Mg^+, P+, PO+, $MgPO_2^+$, P^-, PO^-, PO_2^-, PO_3^-. We also observed uric acid by it protonated molecules, sodium/potassium urates by alkalized uric acid ions (cf. 7.3). The presence of apatite ($Ca_{10}(PO_4)_6(OH,CO_3)$) and tri-calcium phosphate $Ca_3(PO_4)_2$ were recognized by the ion peak ratio $CaPO_2^+/Ca_2O^+$ in admixed struvite stones. It might be interesting to mention that we did not identified calcium oxalate and brushite in admixed struvite stone, furthermore, the SIMS has capability of identifying these components. The revelation of phase identification of calcium phosphates in admixed struvite is greatly discussed in chapter 7 (cf. 7.5). In present study, these stones have highest occurrence frequency of 34.3% as major component.

In struvite admixed stones the association of Na^+ with the presence of hydroxyapatite and K^+ with struvite component was revealed in statistically large number of stones as well as in micro analysis of single stone using TOF-SIMS imaging mode (shown in Figures 7.11-7.13).

Trace elements related to the medical history of patients were also identified with TOF-SIMS. For instance, the presence of iodine due to iodine staining was revealed in STRU2a (cf. 7.3); sodium/potassium urates admixed struvite stone.

Table 8.1. human urinary stones identified as major and minor components

Sr#	Sample	Major	Minor (%)
1.	UA1	uric acid	glycerol
2.	UA2	uric acid	glycerol
3.	UA3	uric acid	glycerol
4.	UA4	uric acid	glycerol
5.	UA5	uric acid	glycerol
6.	UA6	uric acid	glycerol
7.	Urate1	sodium urate	potassium urate
8.	S1	calcium oxalate	brushite(7.43)
9.	S2	calcium oxalate	hydroxyapatite (4.71)
10.	S3	calcium oxalate	hydroxyapatite (21.28)
11.	S4	calcium oxalate	hydroxyapatite (25.39)
12.	S5	calcium oxalate	brushite (13.53)
13.	S6	calcium oxalate	brushite (9.26)
14.	S7	calcium oxalate	brushite (2.99)
15.	S8	calcium oxalate	brushite (8.07)
16.	S9	calcium oxalate	hydroxyapatite (22.83)
17.	S10	brushite	--
18.	S11	hydroxyapatite	struvite (15.11)
19.	S12	hydroxyapatite	calcium oxalate (47.31)
20.	S13	hydroxyapatite	calcium oxalate (33.85)
21.	S14	hydroxyapatite	calcium oxalate (35.85)
22.	S15	hydroxyapatite	calcium oxalate (7.50)
23.	STRU1	struvite	
24.	STRU2b	struvite	(Na, K) Urates
25.	STRU3B	struvite	
26.	STRU4	struvite	
27.	STRU5	struvite	
28.	STRU6	Struvite (core)	K-urate (shell)
29.	STRU7	struvite	
30.	STRU8	struvite	
31.	STRU9	struvite	
32.	STRU11	struvite	
33.	STRU12	struvite	
34.	STRU13	struvite	
35.	cystine1	cystine	arginine + glycerol

The present study shows that TOF-SIMS is equally employed for all kind of stones, including cholesterol gallstones. Using TOF-SIMS, we have clearly identified organic calculi through their molecular ion peaks representing the molecular structures of these components. This study also demonstrates the ability to distinguish cysteine from cystine, which is a common amino acid composed of two molecules of cysteine in oxidized form, although elemental composition of both are the same.

The inorganic urinary stones were identified by their elemental and polyatomic ion peaks. We clearly quantified the calcium phosphates in admixed stones with calcium oxalate and struvite along with their phase identifications that might be of a great interest for medical, the bio-implant research communities (phase identification of calcium phosphates) and geological research community (struvite and calcium phosphates).

Moreover, the upgraded TOF-SIMS VG Ionex IX23LS has proved to be reliable and adequate for future use in routine and research analyses. The limitation of the previous (original) control and data acquisition system has been overcome resulting in a user-friendly and still powerful SIMS facility. The invention of new tip wetting methodology for the primary ion gun will also lowers dependency on service support (we could not found) which we greatly felt for such a unique assembly of ion source.

9. Appendix A

9.1 The constructive-SIMS analysis of reference glycerol

The sample of reference glycerol was prepared on Al foil by rasping the two foils face to face and then dropping and spreading the drop of liquid glycerol on the foil with fine scratches. Sample was analyzed with gallium ion beam by digital raster scanning over an area of ca. 750 µm × 750 µm (128 × 128 pixels). To produce C-SIMS spectrum as shown in Figure 9.1, two mass spectra were collected from the same raster area as proposed by the author in constructive SIMS (cf. 2.2.3). The two mass spectra are shown in Figure 9.2 and 9.3. Constructive factor F_x was obtained by dividing intensity of each peak of the first spectrum with the respective peak of second spectrum. The intensity of C-SIMS mass spectrum was generated by using the following constructive intensity equation (9.1).

$$Intensity = I_{exp} \times F_x \tag{9.1}$$

As we clearly see the enhancement in the molecular ion peak of $[M\text{-}OH]^+$ at m/z 75 as well as other bigger molecular ion peaks at 149, 168, 189 and 363 corresponding to adduct ions of $[2M\text{-}H_3O_2]^+$, $[2M\text{-}OH]^+$, $[2M+Na\text{-}H_2O]^+$ and $[3M+Na\text{-}H_3O_2]^+$. The intensity of protonated glycerol $[M+H]^+$ and its cluster ion $[3M\text{-}3H]^+$ are weak. It might be interesting to remind again that in negative ions mode we observed foremost series of glycerol ion peaks at m/z 93 $[M+H]^-$, 185$[2M\text{-}H]^-$ and 277$[3M\text{-}2H]^-$ [28] with relatively good intensities compared to the intensity of $[M+H]^+$ shown here in positive mode.

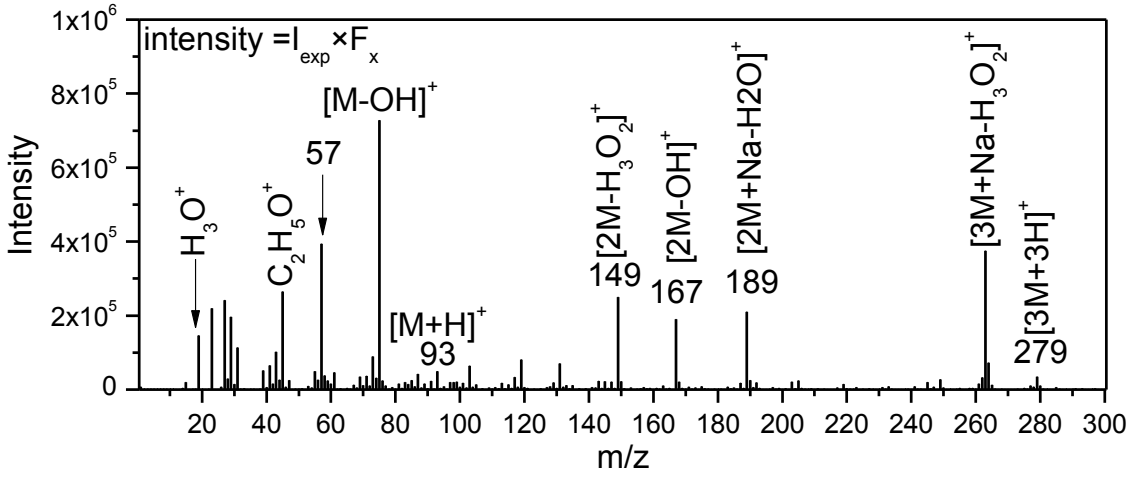

Figure 9.1. The constructive SIMS (C-SIMS) spectrum generated by multiplying the intensity of each peak in the mass spectrum shown in Figure 9.2 with respective constructive factor F_x.

The smaller fragment ions observed are m/z 19, 45, and 57 correspond to H_3O+, $C_2H_5O^+$ and $C_3H_5O^+$, respectively.

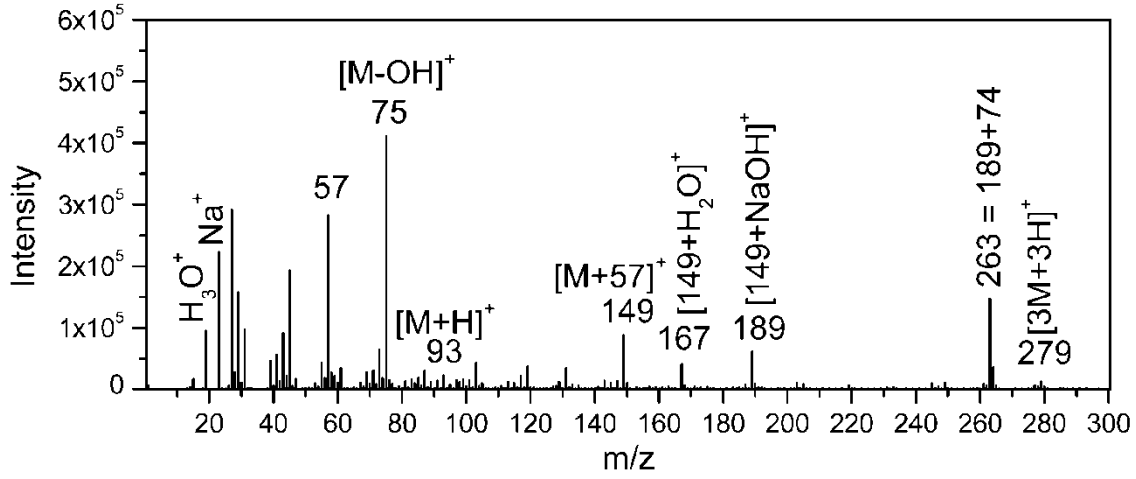

Figure 9.2. TOF-SIMS spectrum from glycerol sample acquired using Ga^+ as primary ions with impact energy of 9 keV and data acquisition time of 5 minutes.

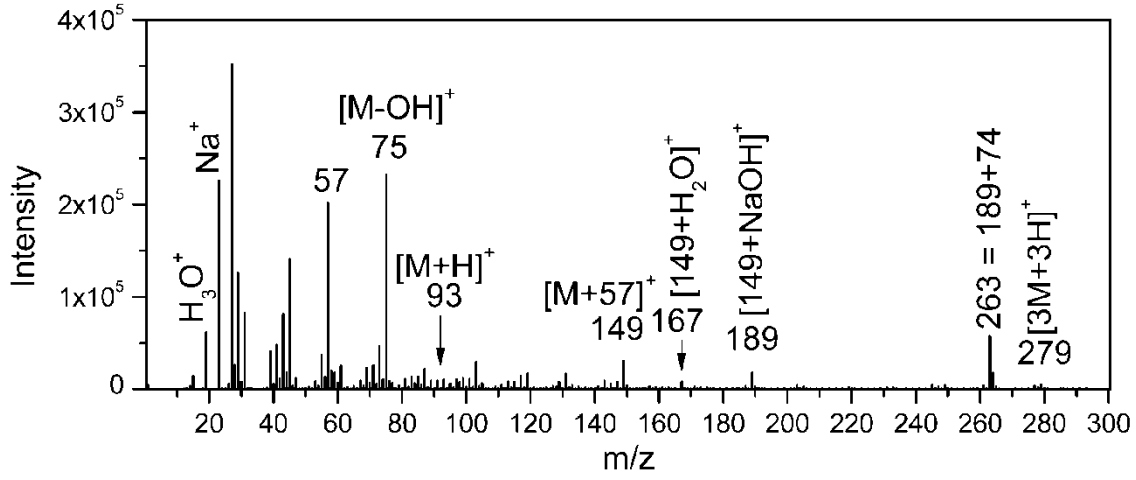

Figure 9.3. Follow-up TOF-SIMS spectrum from glycerol sample acquired using Ga^+ as primary ions with impact energy of 9 keV and data acquisition time of 5 minutes.

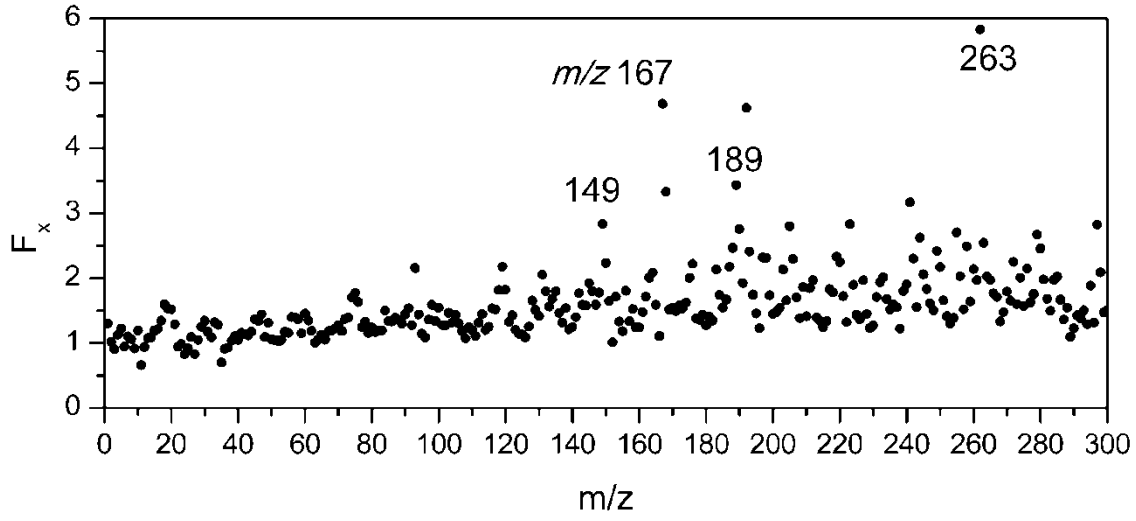

Figure 9.4. Ratio of positive ion intensities from spectra shown above acquired form glycerol on Al substrate with impact energy of 9 keV Ga^+.

10. Appendix B

10.1 The TOF-SIMS analysis of synthetic $Ca(H_2PO_4)_2.H_2O$

The sample of synthetic calcium dihydrogen phosphate $Ca(H_2PO_4)_2.H_2O$ was prepared by pressing the sprinkled powder on indium foil. Sample was analyzed with gallium ion beam by digital raster scanning over an area of ca. 750 µm × 750 µm (128 × 128 pixels). The TOF-SIMS mass spectra were collected from the sample without pre-sputtering (Figure 1a) and after short pre-sputtering (Figure 10.1b). We clearly see the ion peaks of organic contaminants in the mass

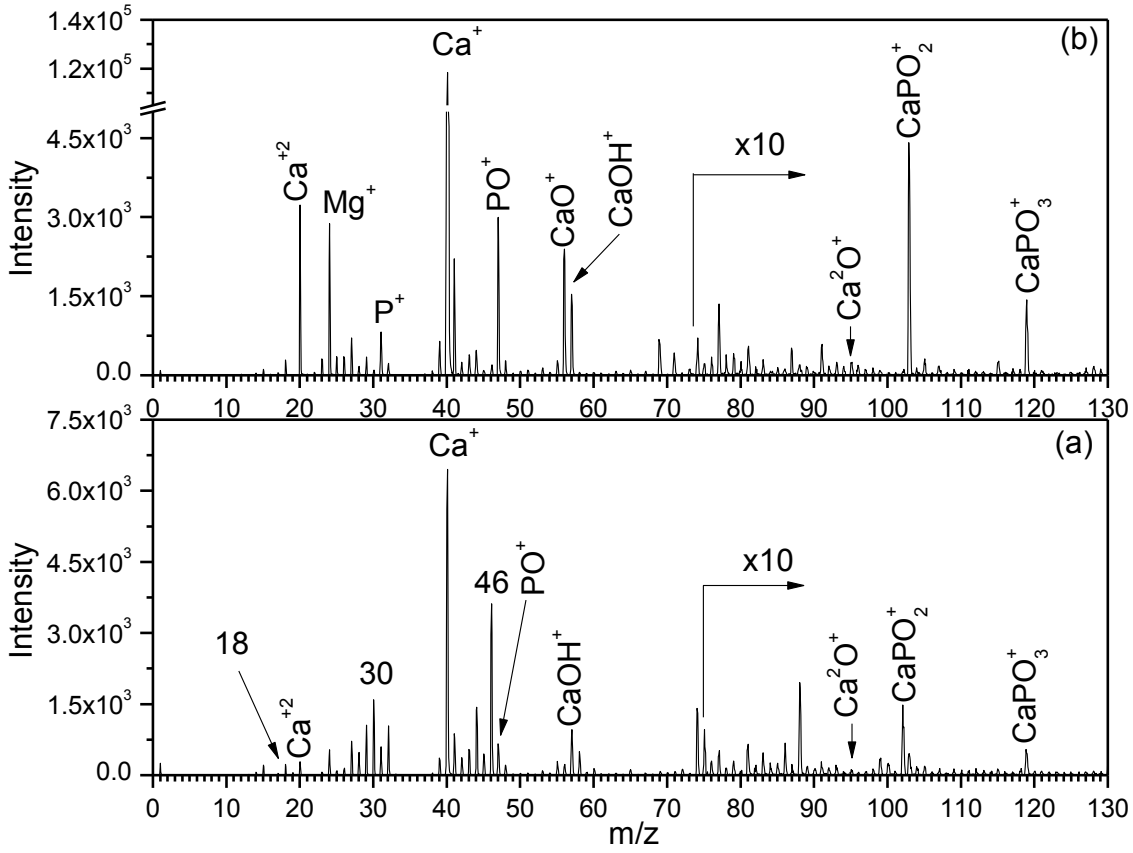

Figure 10.1. Positive ions TOF-SIMS spectra of synthetic $Ca(H_2PO_4)_2.H_2O$ (a) without any pre-sputtering and (b) after sputtering with Ga^+ ion beam in continuous mode with ion dose of ca. 5-15×10^{13} ions/cm^2.

spectrum without pre-sputtering, which could be problem in the phase identification of calcium phosphate. The main contaminant ion peaks observed at m/z 18, 30, and 46 (Figure 10.1a) can be assigned to NH_4^+, NO^+ and NO_2^+, respectively [135] which might be due to ammonium nitrate present as contamination, we did not observed this series of ion peaks in other reference calcium phosphates.

The spectrum after pre-sputtering is mainly representative of calcium phosphate stoichiometric elemental and polyatomic ion peaks. The relative intensities of these peaks are used for the phase identification of these biological important calcium phosphates [29]. We achieved the greatest

value of ion peaks ratios of 9.17 and 21.70 for PO^{+}/POH^{+} and $Ca_2O^{+/}CaPO_2^{+}$ respectively, which is clearly evident in a representative mass spectrum shown in Figure 10.1b. It might also be interesting to state that the Ca^{+2}/Ca^{+} (1.75 %) is also highest for this phase compared other three phases of calcium phosphates discussed in chapter 6 (cf. 6.2.1), the intensity of Ca^{+2} is higher than $CaOH^{+}$ and CaO^{+} peaks. On the other hand these peaks are the second and third most intense peaks in the case of hydroxyapatite and tri-calcium phosphate.

11. References

1. T.L. Colliver, C.L. Brummel, M.L. Pacholski, F.D. Swanek, A.G. Ewing, N. Winograd. Atomic and Molecular Imaging at the Single-Cell Level with TOF-SIMS. *Anal. Chem.* **1997**, 69, 2225.
2. P. Sjovall , J. Lausmaa ,H. Nygren ,L. Carlsson, P. Malmberg. Imaging of membrane lipids in single cells by imprint-imaging time-of-flight secondary ion mass spectrometry. *Anal. Chem.* **2003**, 75, 3429.
3. T. Lundgren, L.G. Persson, E.U. Engstrom, J. Chabala, R. Levi-Setti, J.G. Noren. A secondary ion mass spectroscopic study of the elemental composition pattern in rat incisor dental enamel during different stages of ameloblast differentiation. *Arch. Oral Biol.* **1998**, 43, 841.
4. M.B. Gawande, P.S. Branco, K. Parghi, J.J. Shrikhande, R.K. Pandey, C.A.A. Ghumman, N. Bundaleski, O.M.N.D. Teodoro, R.V. Jayaram; Synthesis and characterization of versatile MgO–ZrO2 mixed metal oxide nanoparticles and their applications. *Catal. Sci. Technol.,* **2011**, 1, 1653.
5. M.B. Gawande, A.Velhinho, I. D. Nogueira, C.A.A. Ghumman, O.M.N.D.Teodoro, P.S. Branco; facile synthesis of cysteine-ferrite magnetic nanoparticles for application in multicomponent reactions - A sustainable protocol. *Royal Society of Chemistry* **2012**, 2, 6144
6. M.B. Gawande, A. Rathi, I.D. Nogueira, C.A.A. Ghumman, N. Bundaleski, O.M.N.D. Teodoro, P.S. Branco. A Reusable and Recyclable Ferrite-Co Magnetic Nanocatalyst for Oxidation of Alcohols to Carbonyl Compounds. *ChemPlusChem* **2012**, 77, 865.
7. M.B. Gawande, A.K. Rathi, P.S. Branco, I.D. Nogueira, A. Velhinho, J.J. Shrikhande, U.U. Indulkar, R.V. Jayaram. C.A.A. Ghumman, N.Bundaleski, O.M.N.D. Teodoro; Regio- and Chemoselective Reduction of Nitroarenes and Carbonyl Compounds over Recyclable Magnetic Ferrite_Nickel Nanoparticles (Fe_3O_4-Ni) by Using Glycerol as a Hydrogen Source. *Chem. Eur. J.* **2012**, 18, 12628.
8. C.A.A. Ghumman, A.M.C. Moutinho, A. Santos, O.M.N.D. Teodoro, A. Tolstogouzov. An upgraded TOF-SIMS VG Ionex IX23LS: study on the negative secondary ion emission of III-V compound semiconductors with prior neutral cesium deposition. *Applied Surface Science* **2012**, 258, 2490.
9. V. Romero, H. Akpinar, D.G. Assimos. Kidney stones: a global picture of prevalence, incidence, and associated risk factors. *Rev. Urol.* **2010**, 12, 86.
10. O.F. Miller, C.J. Kane. Time to stone passage for observed ureteral calculi: a guide for patient education. *J. Urol.* **1999**, 162, 688.
11. K.M. Kim, H.B. Alpaugh, F.B. Johnson. X-ray microanalysis of urinary stones, a comparison with other methods. Scan. Electron Microsc. **1985**, 3, 1239.
12. V.A. Finkielstein, D.S. Goldfarb. Strategies for preventing calcium oxalate stones. *CMAJ*. **2006**, 174, 1407.
13. M.S. Parmar. Kidney stones. *BMJ*. **2004**, 328(7453), 1420.

14. I.A. Hashim, T.H. Zawawi. Wet vs. dry chemical analysis of renal stones. *Ir. J. Med. Sci*. **1999**, 168(2), 114.
15. E.V. Wilson, M.J. Bushiri, V.K. Vaidyan. Characterization and FTIR spectral studies of human urinary stones from Southern India. *Spectrochim. Acta, Part A* **2010**, 77, 442.
16. K. Sekkoum, A. Cheriti, S. Taleb, N. Belboukhari. FTIR spectroscopic study of human urinary stones from El Bayadh district (Algeria). *Arabian J. Chem*. **2011**. DOI: 10.1016/j.arabjc.2011.10.010
17. L.M. Ng, R. Simmons. Infrared spectroscopy. *Anal. Chem*. *1999*, 71(12), 343R.
18. V. Uvarov, I. Popov, N. Shapur, T. Abdin, O.N. Gofrit, D. Pode, M. Duvdevani. X-ray diffraction and SEM study of kidney stones in Israel: quantitative analysis, crystallite size determination, and statistical characterization. *Environ. Geochem. Health* **2011**, 33(6), 613.
19. G. Rebentisch, W. Berg, W. Pirlich, D. Hommann. Assessment and maintenance of the quality of urolith analyses in a comparison of methods. 4th International Ring Test to check quality. *Int. Urol. Nephrol.* **1988**, 20(1), 35.
20. X. Fang, S.R. Ahmad, M. Mayo, S. Iqbal. Elemental analysis of urinary calculi by laser induced plasma spectroscopy. *Lasers Med. Sci*. **2005**, 20(3-4), 132.
21. J.-M. Ouyang. Identification of Urinary Stone Components by X-Ray Photoelectron Spectroscopy *Spectrosc. Lett*. **200**4, 37(6), 633.
22. R.L. Frost, M.L. Weier, K.L. Erickson. Thermal decomposition of struvite. *Therm. Anal. Cal*. **2004**, 76, 1025.
23. J. Siritapetawee, W. Pattanasiriwisawa. An attempt at kidney stone analysis with the application of synchrotron radiation. *J. Synchrotron Radiat*. **2008**, 15, 158.
24. C.A. Zarse, J.A. McAteer, A.J. Sommer, S.C. Kim, E.K. Hatt, J.E. Lingeman, A.P. Evan, J.C. Williams Jr. Nondestructive analysis of urinary calculi using micro computed tomography. *BMC Urol*. **2004**, 4, 15.
25. E. Huri, I. Tatar, C. Germiyanoglu, T. Karakan, H.H. Çelik, O. Ersoy. Evaluation of urinary stones ex vivo with micro-computed tomography: preliminary results of an investigational technique. *Urol. J*. **2011**, 8(3), 185.
26. C.A.A. Ghumman, O.M. T. Carreira, A.M. C.Moutinho, A. Tolstogouzov, V. Vassilenko, O.M.N.D. Teodoro. Identification of human calculi with time-of-flight secondary ion mass spectrometry. *Rapid Commun. Mass Spectrom*. **2010**, 24, 185.
27. C.A.A. Ghumman, A.M.C. Moutinho, A. Tolstogouzov, O.M.N.D. Teodoro. Time-of-flight secondary ion mass spectrometric identification of calcium formate $Ca(HCO_2)_2$ and metabolite of vitamin B6 in human stones. *Rapid Commun. Mass Spectrom.* **2011**, 25, 997.
28. C.A.A. Ghumman, A.M.C. Moutinho, A. Santos, A. Tolstogouzov, O.M.N.D. Teodoro. TOF-SIMS study of cystine and cholesterol stones. *J. Mass. Spectrom*. **2012**, 47, 547.
29. C.A.A. Ghumman, A.M.C. Moutinho, A. Santos, A. Tolstogouzov, O.M.N.D. Teodoro. TOF-SIMS VG Ionex IX23LS: upgrade and application for the urinary stones analysis. *Surface and Interface Analysis*, **2013**, 45,532.

30. H.-G. Tiselius, L. Larsson. Calcium phosphate: an important crystal phase in patients with recurrent calcium stone formation? *Urol. Res*. **1993**, 21(3), 175.
31. J.H. Parks, E.M. Worcester, F.L. Coe, A.P. Evan, J.E. Lingeman. Clinical implications of abundant calcium phosphate in routinely analyzed kidney stones. *Kidney Int*. **2004**, 66(2), 777.
32. G. Spoto, E. Ciliberto, G.C. Allen, A new synthetic route to hydroxyapatite coatings. *J. Mater. Chem*. **1994**, 4, 1849.
33. G.C. Allen, E. Ciliberto, I. Fragalà, G. Spoto. Surface and bulk study of calcium phosphate bioceramics obtained by Metal Organic Chemical Vapor Deposition. *Nucl. Instrum. Methods Phys. Res. B* **1996**, 116, 457.
34. C.C. Chusuei, D.W. Goodman. Calcium Phosphate Phase Identification Using XPS and Time-of-Flight Cluster SIMS. *Anal. Chem*. **1999**, 71, 149.
35. H.B. Lu, C.T. Campbell, D.J. Graham, B.D. Ratner. Surface Characterization of Hydroxyapatite and Related Calcium Phosphates by XPS and TOF-SIMS. *Anal. Chem*. **200**0, 72, 2886.
36. J.C. Vickerman, D. Briggs: *TOF-SIMS surface analysis by mass spectrometry*. Surface Spectra/IM Publications **2001**.
37. P. Sigmund. Theory of Sputtering. Sputtering Yield of Amorphous and Polycrystalline Targets. *Physical Reviews* **1969**, 184, 383.
38. J.P. Biersack, W. Eckstein. Sputtering studies with the Monte Carlo program TRIM.SP. *Appl. Phys.* **1984**, A 34, 73.
39. R.A. Baragiola. Sputtering: survey of observations and derived principles, *Phil. Trans. R. Soc. Lond. A* **2004**, 362, 29.
40. J.B. Malherbe, Sputtering of compound semiconductor surfaces. 1. Ion–solid interactions and sputtering yields. *Crit. Rev. Solid State Mater. Sci.* **1994**, 19, 55.
41. W. Sicthermann and A. Benninghoven. *Int. J. Mass spectrum. Ion proc*. **1991**, *107*, 351
42. I. Yamada, J. Matsuo, N. Toyoda, A. Kirkpatrick. Materials processing by gas cluster ion beams. *Mater. Sci. Eng. R* **2001**, 34, 231.
43. S. Rabbani, A.M. Barber, J.S. Fletcher, N.P. Lockyer, and J.C. Vickerman. TOF-SIMS with Argon Gas Cluster Ion Beams: A Comparison with C_{60}^+. *Anal. Che*m**. 2011**, 83, 3793.
44. M.L. Yu. Charged and excited states of sputtered atoms. In: R. Behrisch, K. Wittmaack (Eds.): *Sputtering by particle bombardment III.* Springer **1991**.
45. M.L. Yu, N.D. Lang: Mechanisms of atomic ion emission during sputtering. *Nucl. Instrum. Methods* **1986**, B14, 403.
46. J.W. Gadzuk. DYNAMICS (vol.3) *Fundamental Atomic-Scale Issues/Processes Pertinent to Dynamics at Surfaces***,** Elsevier, Burlington, MA, **2008**.
47. N.D. Lang and J.K. Nørskov. The Theory of Ionization Probability in Sputtering. *Phys. Scr*. **1983**, T6, 15
48. M.L. Yu: Anomalous coverage dependence of secondary-ion emission from overlayers. *Phys. Rev.B* **1983**, 29 (4), 2311.

49. H. Gnaser. Ion-yield and work function changes during transient cesium concentration. In: G. Gillen, R. Lareau, J. Bennett, F. A. Stevie (Eds.): *Secondary ion mass spectrometry XI*, Wiley **1998**.
50. G. Slodzian, Some problems encountered in secondary ion emission applied to elementary analysis. *Surf. Sci.* **1975**, 48, 161.
51. P. Williams. The sputtering process and sputtered ion emission. *Surf. Sci.* **1979**, 90, 588.
52. H. Gnase. *Low-energy ion irradiation of solid surfaces*. Springer tracts in modern physics, Springer **1999**.
53. C. Tian and W. Vandervors. Effects of oxygen flooding on sputtering and ionization processes during ion bombardment. *J. Vac. Sci. Technol. A* **1997**, 15, 452
54. H.A. Storms, K.F. Brown, J.D. Stein. Evaluation of a cesium positive ion source for secondary ion mass spectrometry. *Anal. Chem.* **1977**, 49, 13, 2023.
55. M.A. Ray, J.E. Baxter, C.M. Loxton, J.E. Greene. Quantitative analysis and depth profiling of rare gases in solids by secondary-ion mass spectrometry: Detection of $(CsR)^+$ molecular ions (R = rare gas). *J. Vac. Sci. Technol. A* **1988**, 6, 1, 44.
56. Y. Gao: A new secondary ion mass spectrometry technique for III-V semiconductor compounds using the molecular ions CsM^+. *J. Appl. Phys.* **1988**, 64, 7, 3760.
57. C.W. Magee, W.L. Harrington, E.M. Botnick. On the use of CsX^+ cluster ions for major element depth profiling in secondary ion mass spectrometry. *Intern. J. Mass Spectrom. Ion Proc.* **1990**, 103, 45.
58. I.S. Gilmore, M.P. Seah. Static SIMS: towards unfragmented mass spectra - The G-SIMS Procedure, *Appl. Surf. Sci*. **2000**,161, 465. G-SIMS of crystallisable organics, *Appl. Surf. Sci.* **2003**, 203-204, 551. Organic molecule characterisation – G-SIMS, *Appl. Surf. Sci*. **2004**, 231-232, 224.
59. M.A. Neto, E.L. Silva, C.A. Ghumman, O.M. Teodoro, A.J.S. Fernandes, F.J. Oliveira, R.F. Silva. Composition profiles and adhesion evaluation of conductive diamond coatings on dielectric ceramics. *Thin Solid Films* **2012**, 520, 5260.
60. R. Said, C.A.A. Ghumman, O.M.N.D. Teodoro, W. Ahmed, A. Abuazza, and J. Gracio. Effects of Bias Voltage on Diamond Like Carbon Coatings Deposited Using Titanium Isopropoxide (TIPOT) and Acetylene/Argon Mixtures onto Various Substrate Materials. *J. Nanosci. Nanotechnol*. **2010**, 10, 2552.
61. R. Said, N. Ali, C.A.A. Ghumman, O.M.N.D. Teodoro, and W. Ahmed. Characterisation of DLC films deposited using Titanium Isopropoxide (TIPOT) at different flow rates. *J. Nanosci. Nanotechnol.* **2009**, 9, 4298.
62. V.F. Neto, R. Vaz, N. Ali, M.S.A. Oliveira, J. Grácio, C.A.A. Ghumman, O.M.N.D. Teodoro. Carbon diffusion into steel during diamond chemical vapour deposition. *Int. J. Nanomanufacturing*. **2008**, 2/ 3, 192.
63. V.F. Neto, R. Vaz, T. Shokuhfar, C.A.A. Ghumman, O.M.N.D. Teodoro, N. Ali, M.S.A. Oliveira, J. Grácio. Diffusion of critical elements in steel during thermal treatments in a diamond chemical vapour deposition atmosphere. Defect and Diffusion Forum **2006**, 258-260, 270.

64. B.T. Chait, K.G. Standing: A time-of-flight mass spectrometer for measurement of secondary ion mass spectra. *Int. J. Mass Spectrom. Ion Proc.***1981**, 40, 185.
65. A. Benninghoven, B. Hagenhoff, E. Niehuis. Surface MS: Probing real-world samples. *Anal. Chem.***1993**, 65, 630A.
66. A. Benninghoven. Chemical analysis of inorganic and organic surfaces and thin films by static time-of-flight secondary ion mass spectrometry (TOF-SIMS). *Angew. Chem. Int. Ed. Engl.***1994** 33, 1023.
67. A. Benninghoven. Surface analysis by secondary ion mass spectrometry (SIMS). *Surf. Sci.* **1994** 299-300, 246.
68. A.J. Eccles and J.C. Vickerman, The characterization of an imaging time-of-flight secondary ion mass spectrometry. *J. Vac. Sci. Technol. A*, **1989**, 7(2), 234.
69. N. Kudo, K. Tsunoda, Y. Terui, Liquid metal ion source and method for producing the same. *US Patent* 6,531,811, **2003**.
70. G.I. Taylor. Disintegration of Water Drops in an Electric Field. *Proc. R. Soc. Lon. A* **1964**, 280, 383.
71. A.J. Eccles, T.A. Steele, A.W. Robinson. Broadening the horizons of SIMS: the low cost chemical microscope, Appl. Surf. Sci. **1999**, 144-45,106.
72. A. Tolstogouzov, S.F. Belykh, M. Stepanova, S.K. Dew, C. Pagura. Characterization of Al^+ secondary ion emission produced by Ne^+ and Ar^+ bombardment of aluminum surface, *Surf. Rev. Lett*. **2004**, 11, 39.
73. U. Bardi, S.P. Chenakin, F. Ghezzi, C. Giolli, A. Goruppa, A. Lavacchi, E. Miorin, C. Pagura, A. Tolstogouzov. High-temperature oxidation of CrN/AlN multilayer coatings, *Appl. Surf. Sci*. **2005**, 252, 1339.
74. M.K. Miller. The ORNL atom probe, *J. Phys. Colloids* **1986**, 47, 493, C2.
75. A.R. Waugh, D.R. Kingham, C.H. Richardson, M. Coff. A time-of-flight mass spectrometer for SIMS and field ionized neutral analysis using a pulsed LMIS, *J. Phys. Colloids* **1987**, 48, 577, C6.
76. W.P. Poschenrieder. Multiple-focusing time of flight mass spectrometers. Part I. TOFMS with equal momentum acceleration, *Int. J. Mass Spectrom. Ion Phys*. **1971**, 6, 413.
77. W.P. Poschenrieder. Multiple-focusing time of flight mass spectrometers. Part II. TOFMS with equal energy acceleration, *Int. J. Mass Spectrom. Ion Phys*. **1972**, 9, 357.
78. G.-H. Oetjen, W.P. Poschenrieder. Focusing errors of a multiple-focusing timeof- flight mass spectrometer with an electrostatic sector field, *Int. J. Mass Spectrom. Ion Phys*. **1975**, 16, 353.
79. T. Grehl, R. Mollers, E. Niehuis. Low energy dual beam depth profiling: influence of sputter and analysis beam parameters on profile performance using TOFSIMS, Appl. Surf. Sci. **2003**, 203–204, 277.
80. P. Wagner and T. M. Hall. *J. Vac. Sci. Technol*. **1979**, 16, 1871.
81. T.S. Sudarshan, L. Park, H. Lim, J.E. Thompson, Method of wetting metals. *US Patent* 4,780,176, **1988**.
82. G.C. Curhan, W.C. Willett, F.E. Speizer, M. J. Stampfer. Intake of vitamins B6 and C and the risk of kidney stones in women. *J. Am. Soc. Nephrol*. **1999**, 10, 840.

83. N.S. Mandel, G.S. Mandel. Urinary tract stone disease in the United States veteran population. II. Geographical analysis of variations in composition. *J. Urol*. **1989**, 142(6), 1516.
84. A. Atsmon, A. DeVries, M. Frank. *Uric Acid Lithiasis*. Amsterdam: Elsevier; **1963**.
85. A. Hesse, H.J. Schneider, W. Berg, E. Hienzsch. Uric acid dehydrate as urinary calculus component. *Invest Urol*. **1975**, 12(5), 405.
86. C.Y. Pak, K. Sakhaee, O. Moe, G.M. Preminger, J.R. Poindexter, R.D. Peterson, P. Pietrow, W. Ekeruo. Biochemical profile of stone forming patients with diabetes mellitus. *Urology*. **2003**, 61(3), 523.
87. W.O. Ekeruo, Y.H. Tan, M.D.Young, P. Dahm , M.E. Maloney, B.J. Mathias, D.M. Albala, G.M. Preminger. Metabolic risk factors and the impact of medical therapy on the management of nephrolithiasis in obese patients. *J. Urol*. **2004**, 172(1):159.
88. M. Daudon, B. Lacour, P. Jungers. Influence of body size on urinary stone composition in men and women. *Urol. Res*. **2006**, 34(3), 193.
89. M. Daudon, O. Traxer, P. Conort, B. Lacour, P. Jungers. Type 2 diabetes increases the risk for uric acid stones. *J. Am. Soc. Nephrol*. **2006**, 17(7), 2026.
90. K. Sakhaee, in *Urinary Tract Stone Disease*, (Eds: P.N. Rao, G.M. Preminger, J.P. Kavanagh), Springer, London, **2011**, pp. 185-194.
91. O.M. Briggs, O. Sperling. Uric acid metabolism in the Dalmatian coach hound. *J. S. Afr. Vet. Assoc*. **1982**, 53, 201.
92. B. Shekarriz, M.L. Stoller. Uric acid nephrolithiasis: current concepts and controversies. *J. Urol*. **2002**, 168, 1307.
93. G.S. Gorman, T. Tamura, J.E. Baggott. Mass spectrometric method for detecting carbon 13 enrichment introduced by folate coenzymes in uric acid. *Anal. Biochem*. **2003**, 321, 188.
94. S.R. Khan, P.A. Glenton. Increased urinary excretion of lipids by patients with kidney stones. *Br. J. Urol*. **1996**, 77(4), 506.
95. H.-W. Peng, C.-F. Chou, M.-S. Shiao, E. Lin, H.-J. Zheng, C.C. Chen, P.C. Fan. Urine lipids in patients with a history of filariasis. *Urol. Res*. **1997**, 25, 217.
96. V. Mazel, P. Richardin, D. Touboul, A. Brunelle, P. Walter, O. Laprévote. Chemical imaging techniques for the analysis of complex mixtures: New application to the characterization of ritual matters on African wooden statuettes. *Analytica Chimica Acta* **2006**, 570, 34.
97. T. Knoll, A. Zöllner, G. Wendt-Nordahl , M.S. Michel, P. Alken. Cystinuria in childhood and adolescence: recommendations for diagnosis, treatment, and follow-up. *Pediatr. Nephrol*. **2005**, 20(1), 19.
98. E. Pras, N. Arber, I. Aksentijevich, G. Katz, J.M. Schapiro, L. Prosen, L. Gruberg, D. Harel, U. Liberman, J. Weissenbach, M. Pras, D. L. Kastner. Localization of a gene causing cystinuria to chromosome 2p. *Nat. Genet*. **1994**, 6(4), 415.
99. E.M. Wright. Cystinuria defect expresses itself. *Nat Genet*. **1994**, 6(4), 328.
100. P. Goodyer. The molecular basis of cystinuria. *Nephron. Exp. Nephrol*. **2004**, 98(2), 45.

101. M. Palacín, V. Nunes, M. Font-Llitjós , M. Jiménez-Vidal, J. Fort , E. Gasol, M. Pineda, L. Feliubadaló , J. Chillarón, A. Zorzano.The genetics of heteromeric amino acid transporters. *Physiology (Bethesda)* **2005**, 20, 112.
102. C.E. Dent, B. Senior. Studies on the treatment of cystinuria. *Br. J. Urol*. **1955**, 27(4), 317.
103. D.S. Goldfarb, F.L. Coe, J.R. Asplin. Urinary cystine excretion and capacity in patients with cystinuria. *Kidney Int*. **2006**, 69(6), 1041.
104. Y. Nakagawa, J.R. Asplin, D.S. Goldfarb, J.H. Parks, F.L. Coe. Clinical use of cystine supersaturation measurements. *J. Urol*. **2000**, 164(5), 1481.
105. C.Y. Pak, C. Fuller, K. Sakhaee, J.E. Zerwekh, B.V. Adams. Management of cystine nephrolithiasis with alphamercaptopropionylglycine. *J. Urol*. **1986**, 136(5), 1003.
106. J.S. Rodman, P. Blackburn, J.J. Williams, A. Brown, M.A. Pospischil, C.M. Peterson. The effect of dietary protein on cystine excretion in patients with cystinuria. *Clin. Nephrol*. **1984**, 22(6), 273.
107. N.N. Dookeran, T. Yalcin, A.G. Harrison. Fragmentation reactions of protonated a-amino acids. *J. Mass Spectrom*. **1996**, 31, 500.
108. W. Kulik, W. Heerma. A study of the positive and negative ion fast atom bombardment mass spectra of a-amino acids. *Biol. Mass Spectrom*. **1988**, 15, 419.
109. N.V. Gogichaeva, T. Williams. MALDI TOF/TOF tandem mass spectrometry as a new tool for amino acid analysis. *J. Am. Soc. Mass Spectrom*. **2007**, 18, 279.
110. F.M. Rubino, C. Verduci, R. Giampiccolo, S. Pulvirenti, G. Brambilla, A. Colombi. Characterization of the disulfides of bio-thiols by electrospray ionization and triple-quadrupole tandem mass spectrometry. *J. Mass Spectr*om. **2004**, 39, 1408.
111. L.D. Strologo. Cystinuria, P. Niaudet (Ed). Orphanet encyclopedia: Paris, France, 2003.
112. C.E. Dent, B. Senior. Studies on the treatment of cystinuria. *Br J Urol.* **1955**, 27(4), 317.
113. F.H. Field. Fast atom bombardment study of glycerol: mass spectra and radiation chemistry. *J. Phys. Chem*. **1982**, 86, 5115.
114. Y.M.F. Marickar, P.R. Lekshmi, L. Varma, P. Koshy. Problem in analyzing cystine stones using FTIR spectroscopy. *Urol. Res*. **2009**, 37, 263.
115. D.E. Johnston, M.M. Kaplan. Pathogenesis and treatment of gallstones. *N. Engl. J. Med*. **1993**, 328, 412.
116. I.S. Kim, S.J. Myung, S.S. Lee, S.K. Lee, M.H. Kim. Classification and nomenclature of gallstones revisited. *Yonsei. Med. J*. **2003**, 44, 561.
117. C.M. McQuaw, A.G. Sostarecz, L. Zheng, A.G. Ewing, N. Winograd. Lateral heterogeneity of dipalmitoylphosphatidylethanolaminecholesterol Langmuir-Blodgett films investigated with imaging time-of-flight secondary ion mass spectrometry and atomic force microscopy. *Langmuir* **2005**, 21, 807.
118. J.J.D. Fitzgerald, P. Kunnath, A.V. Walker. Matrix-enhanced secondary ion mass spectrometry (ME SIMS) using room temperature ionic liquid matrices. *Anal. Chem*. **2010**, 82, 4413.
119. D. Touboul, A. Brunelle, F. Halgand, S.D.L. Porte, O. Laprévote. Lipid imaging by gold cluster time-of-flight secondary ion mass spectrometry: application to Duchenne muscular dystrophy. *J. Lipid Res*. **2005**, 46, 1388.

120. Y.K. Magnusson, P. Friberg, P. Sjövall, J. Malm, Y. Chen. TOF–SIMS analysis of lipid accumulation in the skeletal muscle of ob/ob mice. *Obesity* **2008**, 16, 2745.
121. V. Tazzoli, C. Domeneghetti, The crystal structures of whewellite and weddellite: re-examination and comparison. *American Mineralogist* **1980**, 65, 327.
122. W. Heijnen, W. Jellinghaus, W.E. Klee WE. Calcium oxalate trihydrate in urinary calculi. *Urol. Res*. **1985**, 13, 281.
123. G. Schubert, B. Ziemer. A new calcium oxalate monohydrate produced by thermal dehydration of Weddellite. *Cryst Res Technol*. **1981**,16, 1025.
124. G. Schubert. in *Urinary Tract Stone Disease*, (Eds: P.N. Rao, G.M. Preminger, J.P. Kavanagh), Springer, London, **2011**, pp. 341-354.
125. G. Schubert, G. Brien, S. Lenk, R. Koch. Texture examinations on grain preparations of calcium oxalate calculi and their relations to pathogentic parameters. *Urol. Res*. **1982**, 11,111.
126. G. Schubert, G. Brien. Crystallographic investigations of urinary calcium oxalate calculi. *Intern. Urol. Nephrol*. **1981**,13, 249.
127. D.M. Houston, A. Moore, D.A. Elliott, V.C. Biourge. in *Urinary Tract Stone Disease*, (Eds: P.N. Rao, G.M. Preminger, J.P. Kavanagh), Springer, London, **2011**, pp.131-150.
128. A.A. Pupyshev. Formation of Doubly Charged Atomic Ions in an Inductively Coupled Plasma Discharge. *J. Anal. Chem*. **2001**, 56, 2.
129. M.L. Giannossi and V. Summa. in *An Introduction to the Study of Mineralogy*, (Ed: C. Aydinalp), InTech, Rijeka, **2012**, pp. 123-146
130. L. Yan, Y. Leng, L.-T. Weng. Characterization of chemical inhomogeneity in plasma-sprayed hydroxyapatite coatings. *Biomaterials* **2003**, 24, 2585.
131. G. Betz, G.K. Wehner, in *Sputtering of multicomponent materials*, (Ed: R. Behrisch), Sputtering by Particle Bombardment II. Sputtering of Alloys and Compounds, Electron and Neutron Sputtering, Surface Topography, Springer, Berlin, **1983**, pp. 11–90.
132. M.I.H. Bhuiyan, D.S. Mavinic, F.A. Koch. Thermal decomposition of struvite and its phase transition. *Chemosphere* **2008**, 70, 1347.
133. R. Boistelle, F. Abbona, H.E.L. Madsen. On the transformation of struvite in newberyite in aqueous systems. Physics and *Chemistry of minerals* **1983**, 9, 216.
134. D.S. Gross, M.E. Gälli, P.J. Silva, K.A. Prather. Relative Sensitivity Factors for Alkali Metal and Ammonium Cations in Single-Particle Aerosol Time-of-Flight Mass Spectra. *Anal. Chem*. **2000**, 72, 416.
135. J. D. Allan, J. L. Jimenez, P.I. Williams, M.R. Alfarra, K.N. Bower, J.T. Jayne, H. Coe, D.R. Worsnop. Quantitative sampling using an Aerodyne aerosol mass spectrometer 1. Techniques of data interpretation and error analysis. *Journal of Geophysical Research* **2003**, 108, 4090.